MIXED-METAL OXIDE NANOPOWDERS BY LIQUID-FEED FLAME SPRAY PYROLYSIS (LF-FSP): SYNTHESIS AND PROCESSING OF CORE-SHELL NANOPARTICLES

by

Min Kim

A dissertation submitted in partial fulfillment
of the requirements for the degree of
Doctor of Philosophy
(Materials Science and Engineering)
in The University of Michigan
2008

Doctoral Committee:

Professor Richard M. Laine, Chair
Professor Frank E. Filisko
Professor John Kieffer
Professor Johannes W. Schwank

For Jane and Chaerin

ACKNOWLEDGMENTS

First of all, I would like to thank my advisor, Professor Richard M. Laine for his guidance, support, and especially patience during my whole doctoral study. I also would like to appreciate my committee members; Professor Frank E. Filisko, Professor John Kieffer, and professor Johannes W. Schwank. I acknowledge financial supports from MAXIT group and Air Force. Especially, I would like to appreciate Mr. Roy Rennesund and Mr. Libor Kubina from MAXIT group.

From the bottom of my heart, I really want to thank my colleagues, especially fafnir team members including Jose Azurdia, Julien Marchal, Sanghak Kim, Dr. Thomas R. Hinklin, Samson Lai, Sameer Kumar and Bingyuan Huang, for their support, advice and fellowship. I would also like to thank current and past Laine group members, Professor Sangman Koo, Dr. Norihiro Takamura, Dr. Seungyu Kim, Dr. Kyunghoon Kang, Dr. Jiwon Choi, Dr. Chad Brick, Mike Asuncion, Kunio Takahashi, Mark Roll, and Santy sulaiman. I would like to appreciate Dr. Haiping Sun and Dr. Kai Sun from EMAL for their support and advice. I would love to extend my appreciation to UM MSE professors, current and past fellow Graduate/Undergraduate students.

I would like to thank fellow Korean graduate students of MSE, Macro and ChemE departments. I also would love to appreciate my friends of Ann Arbor Hope Church for their love and support.

Without the support from my family in Seoul, Korea, I could not have reached this point. I would love to thank all my family members including my parents, my brother, my sister, my parents in law and the family of my brother in law.

I really want to thank my wife Chaerin for her love, support, and especially everyday prayer for me. Without the presence of Chaerin and my daughter Jane, I could never have achieved this goal.

Finally, I want to dedicate this work to my Lord, Jesus Christ.

TABLE OF CONTENTS

LIST OF FIGURES

LIST OF TABLES

ABSTRACT

MIXED-METAL OXIDE NANOPOWDERS BY LIQUID-FEED FLAME SPRAY PYROLYSIS (LF-FSP): SYNTHESIS AND PROCESSING OF CORE-SHELL NANOPARTICLES

by

Min Kim

Chair: Richard M. Laine

In this dissertation, liquid feed–flame spray pyrolysis (LF-FSP) was used for the synthesis and characterization of mixed-metal oxide nanopowders in the Ce-Zr-Al-O system for potential catalytic, photonic, electronic and structural applications. The LF-FSP process aerosolizes metalloorganic precursors dissolved in an alcohol solvent with oxygen, combusts the aerosol, and then rapidly quenches the gaseous species to produce nanosize oxide "soot" with the same compositions as those in the starting precursor solutions. The wide variety of potential metal oxide precursors allows the synthesis of multiple chemical compositions, phase and unique particle morphologies in the resulting nanopowders.

Surprisingly, LF-FSP with the correct choice of metalloorganic precursors provides access to core-shell nanopowders in a single step.

The $(ZrO_x)_x(Al_2O_3)_{1-x}$ system was explored first for potential structural applications as zirconia toughened alumina (ZTA) composites. During the LF-FSP

process, core-shell nanoparticles with δ- alumina shell and tetragonal zirconia core form at $(ZrO_2)_x(Al_2O_3)_{1-x}$ (x = 0.4-0.8). Evidence is presented suggesting the incorporation of $Zr^{2+/3+}$ ions in the δ-alumina lattice.

The $(CeO_x)_x(Al_2O_3)_{1-x}$ system was studied for potential catalytic and photonic applications. Small amounts of Ce^{3+} ions substitute into the δ-alumina lattice at all concentrations and Ce-magnetoplumbite is observed at 5-10 mole % CeO_x concentrations.

The $Ce_xZr_{1-x}O_2$ and $(Ce_{0.7}Zr_{0.3}O_2)_x(Al_2O_3)_{1-x}$ systems were also investigated for potential catalytic applications. We were able to produce nano-size single crystal $Ce_{1-x}Zr_xO_2$ solid solutions and core-shell nanostructured $(Ce_{0.7}Zr_{0.3}O_2)_x(Al_2O_3)_{1-x}$ nanopowders.

Sintering studies of the $(ZrO_x)_x(Al_2O_3)_{1-x}$ core-shell nanopowders were performed to produce ZTA composites for structural applications. We were able to produce ZTA composites with 99 +% density and average grain sizes less than 200 nm by pressureless sintering < 1150 ^oC. Tetragonal zirconia was partially stabilized without added yttria. Phase transformation of zirconia (tetragonal to monoclinic) was observed by applied pressure.

Additionally, nanopowders in the $(ZnO)_x(Al_2O_3)_{1-x}$ system were produced as potential transparent conducting oxides (TCOs) for display applications. Al_2O_3 doped ZnO nanopowders (ZnO rich region) were characterized suggesting Al^{3+} ions incorporation into the interstitial sites of zincite. Spinel phase was found not only at 50 mole % ZnO in Al_2O_3 but also at 30 mole % ZnO in Al_2O_3.

CHAPTER 1

INTRODUCTION

1.1 Nanopowders and nanograined ceramics

In the field of ceramic processing, nano-sized powders as the starting point for sintering thin films, membranes and monolithic bodies can provide optimum control of the final microstructure of a given material. Furthermore, the high surface energy of the nanopowders permits sintering at much lower temperatures than traditional micron sized powders. In some instances, sintering of nanopowders can occur at 100s of degrees lower temperatures then micron sized powders.[1] Finally, completely dense monoliths with smaller final grain sizes can provide improved mechanical properties.[1,7,34] These include higher hardness, mechanical strength and because flaw sizes can be reduced, better toughness.[2-4]

For example, the potential exists to make higher toughness, smoother and harder ceramic surfaces that might be used for example in ceramic on ceramic hip implants.[5,6] The quality of the surface frequently determines the lifetime of the implant.[5,6] Thus the development of high-purity, nanograined ceramics is important for a wide variety of leading edge technologies such as high powered lasers, and transparent ballistic armor.[8]

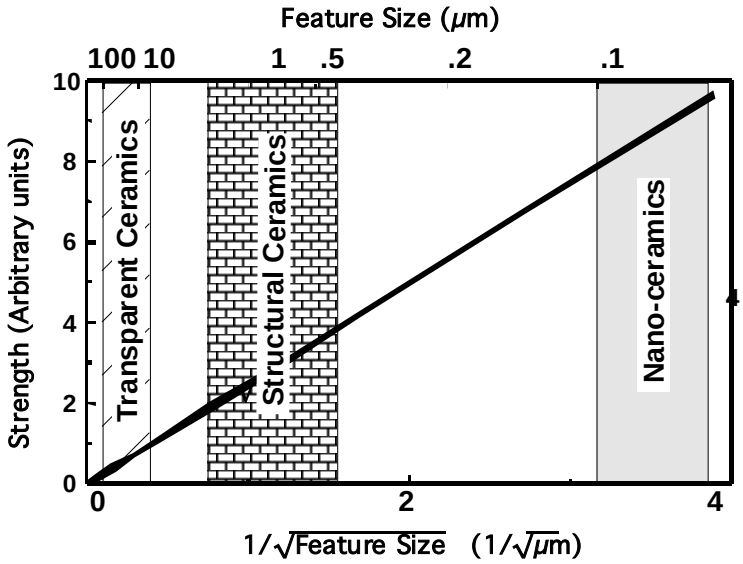

Figure 1.1. Strength of ceramic materials based on statistical fracture mechanics.

There are many challenges to achieving fully dense (< 100 ppm porosity), high purity (< 25 ppm of impurities) and nanograined (< 100 nm) ceramic materials. The primary challenges can best be described as maintaining complete control over phase, chemical composition and homogeneity at nanometer length scales. Figure **1.1** depicts the three classes of grain size ranges of ceramic systems: transparent ceramics, with 5-50 μm grains; structural ceramics, with 0.25 – 2.5 μm grains; and nanograined ceramics, with 0.05 – 0.20 μm grains.

1.2 Liquid feed flame spray pyrolysis (LF-FSP)

We have developed a new approach to generate high surface area, micropore free nanopowders through the use of liquid-feed flame spray pyrolysis (LF-FSP). LF-FSP offers the potential to make a wide variety of single and mixed-metal oxide nanopowders in a single step.[9-16] The LF-FSP process aerosolizes metalloorganic precursors dissolved in an alcohol solvent with oxygen, combusts the aerosol within a quartz chamber at 1500 to 2000 ^{o}C, and then rapidly quenches the gaseous species to produce nanosize oxide "soot" with the same compositions to those in the starting metalloorganic precursors.

These powders are produced free of microporosity with APSs (average particle sizes) of 15-35 nm at surface areas ≥35 m^2/g. By making these materials, we proved that

LF-FSP processing provides easy and precise compositional control as a low-cost route to versatile materials in mixed-metal oxide systems in one step processing as discussed below.

LF-FSP provides easy access to many types of nanopowders with excellent control of phase purity and morphology. These nanopowders offer potential access to a wide variety of ceramic materials for catalytic, mechanical, photonic and electrical applications. Initially we started our work based on specific ceramic materials for catalytic applications, but that also have related uses for many other applications. These include $(ZrO_2)_x(Al_2O_3)_{1-x}$ for catalytic, photonic, and structural applications,[11,29-37] $(CeO_2)_x(Al_2O_3)_{1-x}$ for catalytic, structural, electrical and photonic applications,[23-27] $Ce_xZr_{1-x}O_2$ and $(Ce_{0.7}Zr_{0.3}O_2)_x(Al_2O_3)_{1-x}$ mixed oxide systems for three way auto exhaust catalyst (TWC) applications,[28] and $(ZnO)_x(Al_2O_3)_{1-x}$ for various display applications as well as photovoltaic, electrochromic, RF shielding and sensor applications.[43-48]

1.3 Core-shell nanostructured nanoparticles

Only a few studies have been done to make coated or core-shell nanoparticles such as ZrO_2 coated Al_2O_3,[17] CdS coated SiO_2,[18] SiO_2 coated ZrO_2,[19] SnO_2 coated ZrO_2.[20] Current methods of making coated nanoparticles are mostly based on solution phase methods, and primarily sol-gel processing.[17-20] These synthesis methods are usually multi-step.[17-20] They usually require homogeneous dispersions of core materials in a solvent, typically by ultrasonication, followed by coating with the shell materials. The latter step often leads to micron-sized final products and aggregation of the core powders is unavoidable unless processing is done at low concentrations. Also, these multi-step processes are inefficient in time, cost and homogeneity of final product.[17-20] In contrast, LF-FSP has the potential to provide simple and efficient routes to nano core-shell nanopowders without aggregation.

Surprisingly, we were able to produce core-shell nanostructured nanopowders in a single step for certain compositions of $(ZrO_x)_x(Al_2O_3)_{1-x}$, $(CeO_x)_x(Al_2O_3)_{1-x}$ and $(Ce_{0.7}Zr_{0.3}O_2)_x(Al_2O_3)_{1-x}$ systems. We believe this is due to different nucleation and condensation processes. During particle formation in the flame, species with lower vapor pressures can be expected to nucleate and grow earlier at faster rates than species with

higher vapor pressures. Given that Al_2O_3 has a lower vaporization temperature (3000 ^oC) than CeO_2 (3906 ^oC),[21,22] it seems reasonable to suggest that during the LF-FSP process, ZrO_X/CeO_x species will nucleate and condense first followed by Al_2O_3. This results in homogeneous core-shell nanostructured nanopowders.

Since LF-FSP processing enables rapid quenching in a single step, core-shell ceria/zirconia-alumina mixed-metal oxide materials form at nano size level different from conventionally processed materials.

1.4 Other potential applications

We began our current studies targeting on potential catalytic materials for TWC. However, the systems we studied also have other related uses.

For the $(ZrO_2)_x(Al_2O_3)_{1-x}$ system, we were able to observe what appears to be the presence of $Zr^{2+/3+}$ ions in the δ-alumina lattice. These nanopowders may offer utility in photonic applications anticipated based on Ti doped sapphire lasers, because we find similar amounts of Zr^{3+} (assumed) dissolved in δ-alumina from our studies and Ti^{3+}/Zr^{3+} ions have same valence electron configuration ([Ar]$3d^1$ for Ti^{3+} and [Kr]$4d^1$ for Zr^{3+}).

For the $(CeO_x)_{1-x}(Al_2O_3)_x$ mixed-metal oxide nanopowders, our interest in these materials centers on their emissive behavior for potential use as laser paints and for other photonic applications.[23-25] This research is potentially relevant to improving phosphors for field emission displays, x-ray imaging, nanocomposite lasers and other photonic applications.[26,27]

1.5 Fully dense nanograin ceramic composites

We expanded our work to nanograined ceramics of ZTA (zirconia toughened alumina) nanocomposites based on the availability of $(ZrO_2)_x(Al_2O_3)_{1-x}$ core-shell nanopowders produced by LF-FSP. ZTA (zirconia toughened alumina) has received significant attention over the past two decades, because of its high toughness, good resistance to wear for the structural applications, and chemical stability for the biomedical applications.[29-37]

There are multiple methods of producing crystalline nanopowders,[38-41] but the resulting nanopowders are often aggregated and always agglomerated. Conventional processing methods are not efficient, because nanoparticles are difficult to disperse at high volume loadings compared with traditional, coarser powders. Nanoparticle packing efficiencies are limited by van der Waals interactions associated with the high surface to volume ratio and material transport processes associated with densification usually result in grain growth.[7] Thus, uniform nanostructured ceramic monoliths without large grains are very difficult to produce.

The most critical components in the development of nanograined ceramics are the creation of high purity, uniformly distributed, unaggregated nanopowders. Without pure, stoichiometric, unaggregated starting powders and effective processing procedures, the goal of nanograined ceramics cannot be achieved.[7,42]

Here we are able to produce and characterize fully dense $(ZrO_2)_x(Al_2O_3)_{1-x}$ ceramic nanocomposites with homogeneous, nanosize grains from LF-FSP produced core-shell nanopowders as a prelude to exploring their potential for structural and especially for biomedical applications.[12] These studies use LF-FSP produced $(ZrO_2)_x(Al_2O_3)_{1-x}$ core-shell nanopowders with phase pure t-zirconia cores and δ-alumina shell with APSs < 20 nm. These powders allow us to produce fully dense ZTA nanocomposites with grain sizes less than 200 nm using pressureless sintering in air at < 1150 ^oC. We are also able to control t to m phase transformation of nano zirconia offering the potential to obtain phase transformation toughening.

1.6. $(ZnO)_x(Al_2O_3)_{1-x}$ systems

$(ZnO)_x(Al_2O_3)_{1-x}$ systems have potential as transparent conducting oxides (TCOs) used for a wide variety of applications including various display applications as well as photovoltaic, electrochromic, RF shielding and sensor applications.

Transparent conducting oxides or TCOs are used for a wide variety of applications including various display applications as well as photovoltaic, electrochromic, RF shielding and sensor applications. TCOs typically have band gaps > 3.1 eV (absorptions < 400 nm) and can have conductivities of ≈ 1 x 10^4 Scm^{-1} similar to good metal conductors.[43-52] Although functionally useful TCOs have been made from a wide variety

of alloys or doped forms of In_2O_3, SnO_2, Ga_2O_3, ZnO, PbO_2, SbO_2; the commercial material of choice is doped indium oxide, e.g. In_2O_3:Sn 5-6 at% Sn (ITO). Unfortunately, ITO is expensive because of the scarcity of In. Thus, extensive efforts have been made to find substitutes that provide similar properties at lower costs.

We have previously demonstrated that LF-FSP processing of MgO-, CuO-, CoO-, ZrO-, CeO-, NiO-Al_2O_3 mixed-metal systems provides access to heretofore unknown and/or unusual spinel phases because of the rapid quench kinetics that occur in the process.[9-16] Given that some of these materials and phases may offer unique properties inaccessible using standard ceramics processing methods, we sought to extend LF-FSP processing to $(ZnO)_x(Al_2O_3)_{1-x}$ nanopowders hopefully with similar outcomes. The current studies also serve as the basis for LF-FSP processing of $(ZnO)_x(Al_2O_3)_{1-x}$ nanopowders incorporating tertiary and/or quaternary dopants.

Three phases are found along the ZnO-Al_2O_3 tie-line; ZnO zincite, $ZnAl_2O_4$ spinel, and Al_2O_3 alumina. Based on these phases, a set of compositions was targeted for LF-FSP processing focusing on two main regions of Al_2O_3 doped ZnO [$(ZnO)_x(Al_2O_3)_{1-x}$, x = 0.9-1.0] and middle compositions including spinel phase region [$(ZnO)_x(Al_2O_3)_{1-x}$, x = 0.3-0.5].

1.7 References

1. I-W. Chen, X-H. Wang, "Sintering dense nanocrystalline ceramics without final-stage grain growth," Nature **404** 168-171 (2000)

2. R. M. Laine, J. Marchal, H. Sun, X. Q. Pan, "A new $Y_3Al_5O_{12}$ phase produced by liquid-feed flame spray pyrolysis (LF-FSP)" *Adv. Mater.*, 17 **2005** 830-33

3. A. Krell, P. Blank, H. Ma, T. Hutzler, R. Apetz, M. P. B. van Bruggen, "Transparent sintered corundum with high hardness and strength," *J.Am. Ceram. Soc.* **86[1]** 12-18 (2003)

4. R. Apetz, M. P. B. Van Bruggen, "Transparent alumina: A light-scattering model," *J. Am. Ceram. Soc.*, **86[3]** 480-486 (2003)

5. M. E. Roy, L.A. Whiteside, B. J. Katerberg, J. A. Steiger, "Phase transformation, roughness, and microhardness of artificially aged yttria- and magnesia-stabilized zirconia femoral heads," *J. Biomed . Mat. Res. A* 83A(4) **2007** 1096-1102

6. P. F. Manicone, P. R. Iommetti, L. Raffaelli, "An overview of zirconia ceramics: basic properties and clinical applications," *J. Dent.* 35 (11) **2007** 819-826

7. M. J. Mayo, "Processing of nanocrystalline ceramics from ultrafine particles," *Inter. Mater. Rev.*, 41(3) **1996** 85-115

8. A. Krell, H. Ma, "Nanocorundum-advanced syndissertation and processing," *Nanostructured Mat.* 11(8) **1999** 1141-1153

9. T. Hinklin, B. Toury, C. Gervais, F. Babonneau, J. J. Gislason, R. W. Morton, R. M. Laine, "Liquid-feed flame spray pyrolysis of metalloorganic and inorganic alumina sources in the production of nanoalumina powders," *Chem. Mater*. **16**, 21-30 (2004).

10. J. Marchal, T. Johns, R. Baranwal, T. Hinklin, R. M. Laine, "Yttrium aluminum garnet nanopowders produced by liquid-feed flame spray pyrolysis (LF-FSP) of metalloorganic precursors," *Chem. Mater*. **16**, 822-831 (2004).

11. M. Kim, T. R. Hinklin, R. M. Laine, "Core-shell nanostructure nanopowders along $(CeO_x)_x(Al_2O_3)_{1-x}$ tie-line by liquid-feed flame spray pyrolysis (LF-FSP)" submitted to *Chem. Mater.* (2008).

12. M. Kim. R. M. Laine, "Liquid-feed flame spray pyrolysis (LF-FSP) for combinatorial processing of nanooxide powders along the $(ZrO_2)_{1-x}(Al_2O_3)_x$ tie-line. Phase segregation and the formation of core-shell nanoparticles," *J. Cer. Proc. Res. **8** 129-136* (2007).

13. S. Kim, J. J. Gislason, R.W. Morton, X. Q. Pan, H. P. Sun, R. M. Laine, "Liquid-feed flame spray pyrolysis of nanopowders in the alumina-titania System," *Chem. Mater.* **16**, 2336-2343 (2004).

14. J. A. Azurdia, J. Marchal, R. M. Laine, " Synthesis and characterization of mixed-metal oxide nanopowders along the CoO_x–Al_2O_3 tie line using liquid-feed flame spray pyrolysis," *J. Am. Ceram. Soc.*, **89 [9]** 2749–2756 (2006)

15. J. A. Azurdia, J. Marchal, P. Shea, H. Sun, X. Q. Pan, R. M. Laine, " Liquid-feed flame spray pyrolysis as a method of producing mixed-metal oxide nanopowders of potential interest as catalytic materials. Nanopowders along the NiO-Al_2O_3 tie line including $(NiO)_{0.22}(Al_2O_3)_{0.78}$, a new inverse spinel composition," *Chem. Mater.* **18** (2006) 731-739.

16. (a) Laine, R. M.; Treadwell, D. R.; Mueller, B. L.; Bickmore, C. R.; Waldner, K.F.; Hinklin, T. *J. Chem. Mater*. **1996**, 6, 1441. (b) Laine, R. M., Mueller, B. L., Hinklin, T. U.S. Patent 5,418,298, 1995.

17. Y. Jia, Y. Hotta, K. Sato, K. Watari, "Homogeneous ZrO_2-Al_2O_3 composite prepared by nano-ZrO_2 particle multilayer-coated Al_2O_3 particles," *J. Am. Ceram. Soc*. **89[3]** (2006) 1103-1106

18. S. Chang, L. Liu, S. Asher, "Preparation and properties of tailored morphology, monodisperse colloidal silica-cadmium sulfide nanocomposites," *J. Am. Chem. Soc*. **116** (1994) 6739-6744

19. A. J. Ruys, Y. Mai, "The nanoparticle-coating process: a potential sol-gel route to homogeneous nanocomposites," *Mater. Sci. Eng*. **A265** (1999) 202-207

20. J. D. Ferguson, K. J. Buechler, A. W. Weimer, S. M. George, " SnO_2 atomic layer deposition on ZrO_2 and Al nanoparticles: Pathway to enhanced thermite materials," *Powder Technology* **156** (2005) 154-163

21. R. Jossen, S. E. Pratsinis, W. J. Stark, and L. Madler, "Criteria for flame-spray synthesis of hollow, shell-like, or inhomogeneous oxides," *J. Am. Ceram. Soc*. **88** [6] (2005) 1388-1393

22. CRC handbook of chemistry and physics. 80^{th} ed.**1999-2000**. CRC press

23. a. R.M. Laine, S. C. Rand, T. R. Hinklin, G. R. Williams, " Ultrafine powders and their use as lasing media," *U.S.Patent* 6,656,588 Decenber 2, 2003. b. Hinklin T.R.; Ph.D. dissertation, Mixed-metal Oxide Nanopowders for Structural and Photonic Applications, 2006, University of Michigan.

24. B. Li, G. R. Williams, S. C. Rand, T. R. Hinklin, R. M. Laine, "Continuous–wave ultraviolet laser action in strongly scattering Nd-doped alumina," *Opt. Lett.* **27**(6)

394-396 (2002)

25. G. R. Williams, S. B. Bayram, S. C. Rand, T. R. Hinklin, R. M. Laine, “Laser action in strongly scattering rare-earth-metal-doped dielectric nanophosphors,” *Phys. Rev. A* **65** 013807 (2001)

26. C. Chiang, M. Tsai, M. Hon, “Preparation of cerium-activated GAG phosphor powders influence of Co-doping on crystallinity and luminescent properties,” *J. Electrochem. Soc.* **154(10)** J326-J329 (2007)

27. J. Touš, K. Blažek, L. Pína, B. Sopko, “High-resolution X-ray imaging CCD camera based on a thin scintillator screen,” *Radia. Meas.* **42** 925 – 928 (2007)

28. H.W. Jen, G.W. Graham, W. Chun, RW. McCabe, J.P Cuif, S. Deutsch, O.Touret, "Characterization of Model automotive exhaust catalysts: Pd on Ceria and Ceria-zirconia supports," *Cat. Today* **50** 309-28 (1999).

29. G. Magnani, A. Brillante, “ Effect of the composition and sintering process on mechanical properties and residual stresses in zirconia-alumina composites,” *J. Europ. Ceram. Soc.* **25** 3383-3392 (2005)

30. M. Szutkowska, “Fracture toughness behavior of alumina-zirconia composites,” J. Mater. Proc. Tech. **153-154** 868-874 (2004)

31. S. T. Aruna, K. S. Rajam, “ Mixture of fuels approach for the solution combustion synthesis of Al_2O_3-ZrO_2 nanocomposites,” *Mater. Res. Bull*. **39** 157-167 (2004)

32. Lukas, P.; Vrana, M.; Mikula, P.; Vleugels, J.; Anne, G.; Van der Biest, O. *Phys. B* 350 **2004** e517–e520

33. Jimenez-Piquea, E.; Ceseracciua, L.; Chalvetb, F.; Angladaa, M.; De Portub, G. *J. Europ. Ceram. Soc.* 25 **2005** 3393–3401

34. Dakskobler, A.; Kosmac, T. *J. Europ. Ceram. Soc.* 24 **2004** 3351–3357

35. D. Jayaseelan, T. Nishikawa, H. Awaji, F .D. Gnanam, “Pressureless sintering of sol-gel derived alumina-zirconia composites,” *Mater. Sci. Eng.* **A256** 265-270 (1998)

36. D. Casellas, M. M. Nagl, L. Llanes, M. Anglada, “Fracture tougness of alumina and ZTA ceramics,” J. Mater. Proc. Tech. **143-144** pp.148-152 (2003)

37. W. H. Tuan, R. Z. Chen, T. C. Wang, C. H. Cheng, P. S. Kuo, “Mechanical properties of Al_2O_3/ZrO_2 composites,” *J. Europ. Ceram. Soc.* **22** 2827-2833 (2002)

38. O. Masala, R. Seshadri,. *Annu. Rev. Mater. Rev.* 34 **2004** 41-81

39. M. T. Swihart, “Vapor phase syndissertation of nanoparticles,” *Coll. Inter. Sci.* 8 **2003** 127-133

40. M. K. Wu, R. S. Windeler, C.K. R. Steiner, “Controlled syndissertation of nanosized particles by aerosol process,” *Aerosol. Sci. Tech.* 19(4) **1993** 527-548

41. T. Gurav. T. P. Kodas, “Aerosol processing of materials,” *Aerosol Sci. Tech*. 19(4) **1993** 411-452

42. R.W. Siegel, “Nanostructured materials-mind over matter,” *Nanostructured Mat.* 3 **1993** 1-18

43. H. Hosono, H. Ohta, M. Orita, K. Ueda, M. Hirano, “Frontier of transparent conductive oxide thin films,” Vacuum **66**, 419-425 (2002).

44. I. Hamberg and C. G. Granqvist, “Evaporated Sn-doped In_2O_3 films: Basic optical properties and applications to energy-efficient windows,” J.Appl. Physics **60**, R123-R160 (1986).

45. P.P. Edwards, A.Porch, M.O. Jones, D.V. Morgan, R.M. Perks, “Basic materials physics of transparent conducting oxides,” Dalton Trans. 2995-3002 (2004).

46. H. Hono, “Built-in Nanostructures in Transparent Oxides for Novel Photonic and Electronic Functions Materials,” Int. J. Appl. Ceram. Technol. **1**, 106-18 (2004).

47. D.S. Ginley, C. Bright, “Transparent conducting oxides,” MRS Bull. **25**, 15-18 (2000).

48. B.G. Lewis, D.C. Paine, “Applications and processing of transparent conducting oxides,” MRS Bull. **25**., 22-7 (2000).

49. H.Kawazoe, H. Yanagi, K. Ueda, H. Hosono, “Transparent p-type conducting oxides: Design and fabrication of p-n heterojunctions,” MRS Bull., **25**, 28-36 (2000).

50. T. Minami, “New n-type transparent conducting oxides,” MRS Bull. **25**, 38-44 (2000).

51. R.G. Gordon, “Criteria for choosing transparent conductors,” MRS Bull. **25**, 52-7 (2000).

52. T.J. Coutts, D.L. Young, X. Li, “Characterization of Transparent Conducting Oxides, Mater. MRS Bull., **25**, 58-65 (2000).

CHAPTER 2

PROCESSING NANOPOWDERS ALONG THE $(ZrO_2)_{1-x}(Al_2O_3)_x$ TIE-LINE

2.1 Abstract

We report here the synthesis of $(ZrO_2)_{1-x}(Al_2O_3)_x$ nanooxide powders with molar ratios that span the ZrO_2-Al_2O_3 composition range. Liquid-feed flame spray pyrolysis (LF-FSP) of mixtures of $N(CH_2CH_2O)_3Al$ (alumatrane) and $Zr(CH_3CH_2COO)_2(OH)_2$ precursors dissolved in ethanol, were aerosolized with O_2, combusted at temperatures of 1500-2000°C and rapidly quenched thereafter to provide $(ZrO_2)_{1-x}(Al_2O_3)_x$ nanopowders of selected compositions. All powders exhibit average particle sizes (APSs) < 20 nm and corresponding surface areas of ≈ 50 m^2/g when produced at rates of 100-300 g/h. The as-processed powders were characterized in terms of phase, size, specific surface area, composition, and morphology by BET, XRD, XRF, SEM, TEM, FT-IR, and TGA-DTA. The presence of δ-alumina and tetragonal zirconia is observed over most of the compositions studied. Furthermore, this phase segregation leads to the formation of core-shell materials. Evidence is presented suggesting the incorporation of $Zr^{2+/3+}$ ions above the published solubility limit of ZrO_2 in δ-alumina.

Key Words: core-shell nanoparticles, liquid-feed flame spray pyrolysis, $(ZrO_2)_{1-x}(Al_2O_3)_x$ nanopowders, $(ZrO_2)_{1-x}(Al_2O_3)_x$ tieline, phase-separated nanopowders.

2.2 Introduction

Zirconia is an important material for a wide range of applications.[1,2] Besides its traditional uses in refractory ceramics and abrasion-resistant materials, high-surface area zirconia is used in applications ranging from catalysts[3] to oxygen sensors[4], to solid oxide fuel cells (oxygen electrolyte)[5] to gate dielectrics for MOSFET.[6,8] Zirconia has a high dielectric constant (~25), a wide energy band gap (7.8 eV), and when alloyed with ceria as the oxygen storage media in three way auto exhaust catalytic converters, TWCs, it greatly improves sinter resistance.[3-7] Doping zirconia with yttria (YSZ) or alumina (ZTA) to stablize the tetragonal phase, provides unusual toughening for a wide variety of mechanical applications. ZTA materials combine high flexural strength (~910 MPa) and hardness (~15 GPa) with good fracture toughness (~7 MPa $m^{1/2}$).[8,9] Unfortunately ZTA's very useful high temperature properties also contribute to difficulties in its processing to dense, defect-free composite materials.[10,11]

We have developed a new approach to high surface area, micropore free mixed-metal oxide nanopowders using liquid-feed flame spray pyrolysis (LF-FSP). LF-FSP offers the potential to make a wide variety of single and mixed-metal oxide nanopowders in a single step.[12-18] The LF-FSP process aerosolizes metalloorganic precursors dissolved in an alcohol solvent with O_2, combusts the aerosol within a quartz chamber at 1500-2000 ^oC, and then rapidly quenches the gaseous species to produce nanosize oxide "soot" with compositions identical to those in the starting metalloorganic precursors. See the experimental section below for details.

In previous studies we have used LF-FSP to make phase-pure nanopowders of single metal oxides including Al_2O_3, CeO_2, ZrO_2 and NiO.[12-18] These LF-FSP nanopowders are unaggregated and as-produced are without microporosity at surface areas of 30-50 m^2/g and average particle sizes (APSs) of 15-30 nm. We have also made binary metal nanopowders along the $(MO_z)_{1-x}(Al_2O_3)_x$ tielines were M = Ni, Ti, Co, Mg, Cu, Zn and CeO_2 by LF-FSP.[15-18] The majority of these nanopowders are solid solutions without microporosity with SSAs of 45-70 m^2/g and APSs of 15-35 nm.

LF-FSP provides easy access to many types of nanopowders with excellent control of phase purity and morphology. Furthermore, LF-FSP processing provides low-cost, easy and precise compositional (combinatorial) control to versatile nanomaterials in mixed-

metal oxide systems using one-step processing. These nanopowders in turn offer potential access to a wide variety of materials for catalytic, mechanical, photonic and electrical applications.

The potential to make high homogeneous ZTA nanopowders that offer relatively easy access to high strength monolithic ZTA components provides motivation for the work reported here. Additional motivation comes from the potential to create ZTA nanocomposites amenable to superplastic deformation.[19] Finally, the studies reported when combined with work on $[(CeO_2)_{1-x}(ZrO_2)_x]_{1-y}(Al_2O_3)_y$ to be described elsewhere[20], suggest a potential for one step processing of the washcoats used in TWCs.

Unlike many of the nanopowders previously produced by LF-FSP processing by us and others.[7-9,24,25] LF-FSP processing of materials along the $(ZrO_2)_x(Al_2O_3)_{1-x}$ tieline does not produce solid solutions but nanocomposites of each composition. As with other LF-FSP products, the resulting unaggregated nanopowders offer specific surface areas (SSAs) $\geq$ 45 m^2/g without microporosity and although not yttria stabilized, the only zirconia phase observed is tetragonal over all compositions studied.

2.3 Experimental

Liquid-feed flame spray pyrolysis (LF-FSP)

LF-FSP, invented at the University of Michigan, has been described in more detail in published papers.[12-18] Briefly, alcohol (typically EtOH) solutions containing 1-10 wt % loading of ceramic as precursors, e.g. single- or mixed-metal alkoxides, carboxylates or β-diketonates are aerosolized with O_2 into a quartz chamber where it is ignited with methane pilot torches.

Initial combustion temperatures run 1500°-2000°C, depending on the processing conditions, generating nanopowder "soot." Temperatures drop to 300-500 °C over 1.5 metre, equivalent to a 1000°C quench in ≤ 100 ms leading to kinetic products and nanopowders that are largely unaggregated; although they are lightly agglomerated. "Shooting" rates can be 200 g/h when using wire-in-tube electrostatic precipitators operating at 10 kV. Typical powders are 15 to 100 nm APS with specific surface areas (SSAs) of 30 to 100 m^2/g. When combinations of elements are used, the resulting nanopowders will have compositions identical to those of the precursor solutions. Since compositions of chemical solutions can be changed intentionally, potentially even during mixing just before aerosolization, it becomes possible to combinatorially produce mixed-metal oxide materials. Hence it becomes possible to rapidly optimize materials for given properties or for ease of processing.

Materials

Alumatrane. $N(CH_2CH_2O)_3Al$ prepared as described previously[21,22] is used as the alumina source.

Zirconium propionate. Zirconium carbonate [$2ZrO_2(CO_2)\cdot x(H_2O)$, 99%, 150 g, 0.34 mole] was reacted with excess proprionic acid (500 ml, 6.80 mole) in a 1 l flask equipped with a still head and an addition funnel. N_2 was sparged directly through the solution (13.7 KPa pressure) as the solution was heated at 120 °C/2h with magnetic stirring to distill off ~150 ml of liquid (water and propionic acid). The ceramic loading of the resulting precursor was 11 wt% as determined by TGA.

XRD studies

As-prepared samples were characterized using a Rigaku Rotating Anode Goniometer. Powder samples were prepared by placing ≈ 100 mg in XRD sample holders

(amorphous silica slides) for data collection. CuKα (λ = 1.54 Å) radiation with a Ni filter was used with a working voltage and current of 40 kV and 100 mA, respectively. Scans were continuous from 5–90° 2θ with a step scan of 2° 2θ/minute in increments of 0.05° 2θ. Peak positions and relative intensities were characterized by comparison with PDF files of standard materials: ZrO_2 (PDF file 42-1164), δ-Al_2O_3 (PDF file 46-1131) Debye-Scherer line broadening was used to calculate average particle sizes from the XRD powder patterns.

Thermal Gravimetric Analysis and Differential Thermal Analysis (TGA/DTA)

TGA-DTA was performed using a SDT 2960 Simultaneous Differential Thermal Analyzer (TA Instruments, Inc., New Castle, DE). The instrument was calibrated with gold supplied by Perkin-Elmer. Samples (70 mg) of as-prepared powders were hand pressed in a 3 mm dual action die and placed inside Pt sample cups and heated at ramp rates of 10 K/minute from ambient temperature to 1400˚C. The reference material was a pellet of α-alumina. A flow of synthetic air, 50 ml/minute, was maintained during all experiments.

Specific surface area (SSA)

SSA was measured on a Micromeritics ASAP 2000 sorption analyzer. Samples (200 mg) were degassed at 400°C until the outgas rate was 5 mmHg/minute. Analyses was run at 77K with N_2. SSAs were determined by the BET multipoint method using at least five data points. The average particle size was derived using the formula $< R >= \frac{3}{\rho \times SSA}$ where <R> = average particle size, and ρ is the density of the material.

Scanning electron microscopy (SEM)

A field emission SEM (Phillips XL30FEG) was used to image powder morphologies. Powder samples were dispersed in distilled H_2O using an ultrasonic horn (Vibra-cell, Sonics and Materials, Inc., Newton, CT). A drop of the dispersed powder/water was placed on an aluminum SEM stub and allowed to dry for 4 h on a hot plate. Powders were sputter coated with 10-40 nm of Au-Pd to reduce charging effects. Operating voltage was between 15.0 and 30.0 kV.

Transmission electron microscopy (TEM)

An analytical high resolution TEM (Model 3011, JOEL, Osaka, Japan) was used to measure the particle sizes and morphologies of as-prepared powders. Powder samples were prepared by dipping a holey carbon grid in a vial of emulsion with as-prepared powder. The specimen was held in a Gatan double tilt goniometer. An operating voltage of 300 kV was used.

FTIR Spectra.

Diffuse reflectance Fourier transform (DRIFT) spectra were recorded on a Mattson Galaxy Series FTIR 3000 spectrometer (Mattson Instruments, Inc., Madison, WI). Optical grade, random cuttings of KBr (International Crystal Laboratories, Garfield, NJ) were ground, with 1.0 wt % of the sample to be analyzed. For DRIFT analysis, samples were packed firmly and leveled off at the upper edge to provide a smooth surface. For transmission IR, 100 mg of each sample prepared for DRIFT analysis was pressed in a stainless steel double action die (12.75 mm diameter) at 100 MPa for 1 minute in a Carver Press (model 3912). Fresh backgrounds of pure KBr were done every 2 hour. The FTIR sample chamber was flushed continuously with N_2 prior to data acquisition in the range 4000-400 cm^{-1}. Each run consisted of 128 scans with a resolution of $\pm$ 8 cm^{-1}.

2.4 Results and discussion

In the following sections we begin by characterizing the zirconia precursor developed for LF-FSP processing. Thereafter we follow with sections on the production of selected nanopowders along the $(ZrO_2)_{1-x}(Al_2O_3)_x$ tieline, their phase behavior, particle morphologies, surface chemistries and thermal properties.

Precursor and precursor formation

We previously reported the characterization of alumatrane [$N(CH_2CH_2O)_3Al$] and its use as a precursor in LF-FSP for the synthesis of δ-alumina nanopowders.[12,16,21,22] Here we report on the zirconium precursor, $Zr(O_2CCH_2CH_3)_2(OH)_2$. synthesized as discussed in the experimental section. This precursor has a thermal decomposition pattern similar to other metal carboxylate precursors studied previously.[12-18]

Figure **2.1** shows a TGA trace for $Zr(O_2CCH_2CH_3)_2(OH)_2$. Initial mass losses (8%) are due to propionic acid of recrystallization. Thereafter, mass loss events are attributed to the decomposition of the propionate ligands as reaction suggested in reaction (1)~(3).[12-18,21,22]

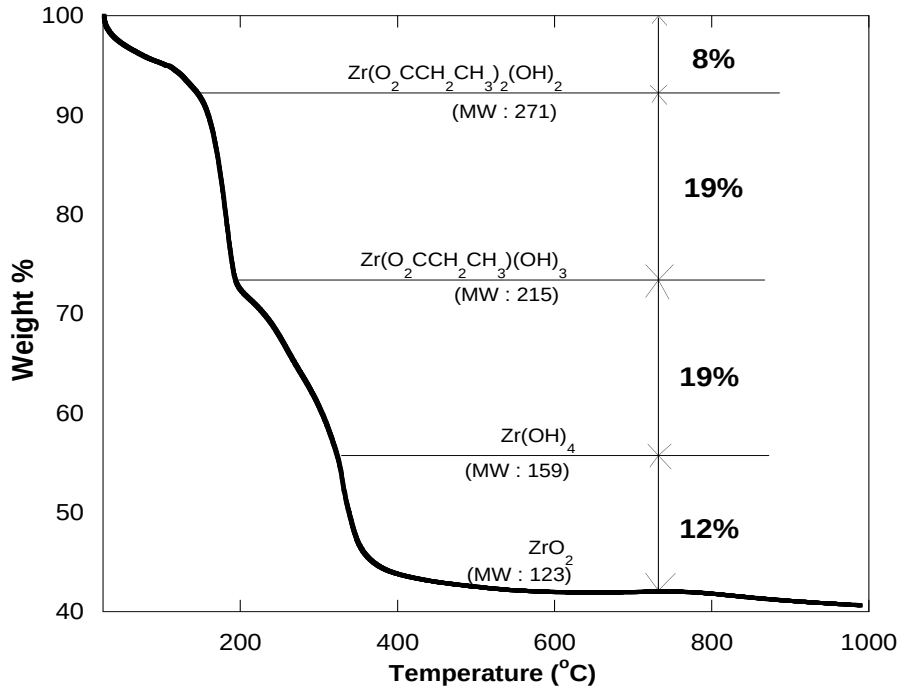

Figure 2.1. TGA of $Zr(CH_3CH_2COO)_2(OH)_2$ ramped at 10°C/min in synthetic air.

$$Zr(O_2CCH_2CH_3)_2(OH)_2 \rightarrow Zr(O_2CCH_2CH_3)(OH)_3 + CH_3CH=C=O \quad (1)$$

Calc. (Found) Mass Loss = 19.01% (19%)

$$Zr(O_2CCH_2CH_3)(OH)_3 \rightarrow Zr(OH)_4 + CH_3CH=C=O \quad (2)$$

Calc. (Found) Mass Loss = 19.01% (19%)

$$Zr(OH)_4 \rightarrow ZrO_2 + 2H_2O \quad (3)$$

Calc. (Found) Mass Loss = 12.22% (12%)

Final ceramic yields [42% (ZrO_2)] are within experimental error of the calculated value (41.75%) from the decomposition of the precursor [$Zr(CH_3CH_2COO)_2(OH)_2$] to oxide (ZrO_2) and are as expected based on previous studies.[12-18,21,22]

Compositions of as-processed nanopowders

Eight different precursor compositions in the $(ZrO_2)_x(Al_2O_3)_{1-x}$ system were prepared by making simple mixtures of alumatrane and the propionate as detailed in the Experimental. Table **2.1** lists the compositions of the LF- FSP produced nanopowders. Compositions were confirmed by XRF. These nanopowders were analyzed by XRD, SEM, FT-IR and TGA-DTA as discussed in the following sections.

Table 2.1. Compositions of the $(ZrO_2)_x(Al_2O_3)_{1-x}$ nanopowders.

Sample	Mole %ZrO_2	Wt % ZrO_2	Mole % Al_2O_3
1	2.4	3.0	96.8
2	4.1	5.0	94.9
3	4.6	5.6	94.3
4	5.9	7.1	92.8
5	8.4	10.0	90.0
6	13.6	16.0	93.9
7	49.7	54.5	45.4
8	79.4	82.4	17.6

XRD powder pattern studies

Figure **2.2** provides XRD patterns for as-produced nanopowders along the $(ZrO_2)_x(Al_2O_3)_{1-x}$ tie-line (Table **2.1**). In contrast to previous studies discussed above, we observe what appears to be complete phase separation as indicated by the presence of t-zirconia and δ-alumina in Samples 2-7, Table **2.1**.

It is important to note that two excellent papers from the Hahn and Winterer groups on low alumina content zirconia,[23,24] made by a process similar to LF-FSP have recently been published that corroborate our observations in this region of the tieline. Thus, their XRD studies of zirconia rich samples in $(ZrO_2)_x(Al_2O_3)_{1-x}$ at x = 0.5 ~1.0 indicate that the tetragonal phase is dominant in the zirconia-rich region as seen for 49.7 ZrA and 79.4 ZrA with the minor phase being of δ-alumina. They also briefly mention the formation of a transition alumina phase but did not characterize it.

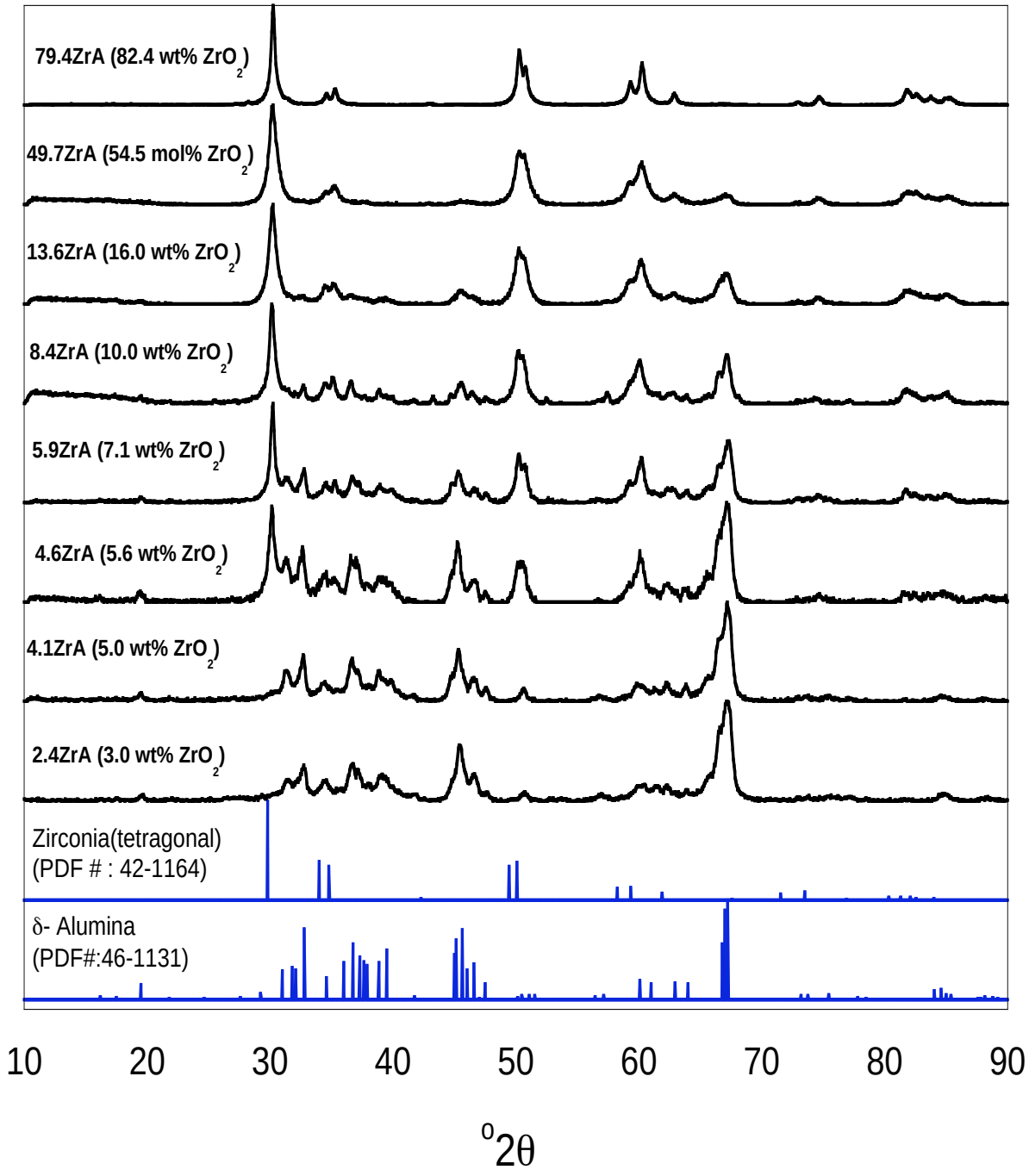

Figure 2.2. XRD powder patterns of $(ZrO_2)_x(Al_2O_3)_{1-x}$.
2.4 ZrA denotes 2.4 mole % ZrO_2 included in ZrO_2-Al_2O_3 binary system.

Average particle size (APSs) and specific surface area (SSAs) from BET

The APSs for these materials were estimated from Debye Scherer line broadening and their SSAs (Table **2.2**). Both methods give very similar results. The average SSAs for the samples are 52 ± 5 m^2/g, giving APS values of 15 ± 3 nm. Although the Hahn/Winterer studies[23,24] show that particle sizes decrease with increasing alumina contents, in the zirconia-rich region, we do not observe any such changes. This may be a consequence of the differences in method of processing or precursors used. Note that LF-FSP production is at rates of 100-300 g/h vs 3 g/h for CVS (chemical vapor synthesis) by Hahn/Winterer.

Table 2.2. APSs and SSAs of as produced LF-FSP samples

Sample	XRD line broadening Particle size (nm)	BET-derived Particle size (nm)	SSAs (m^2/g)
2.4ZrA	18 ± 1	14 ± 0.5	54 ± 0.5
4.1ZrA	18 ± 1	13 ± 0.5	57 ± 0.5
4.6ZrA	15 ± 1	13 ± 0.5	55 ± 0.5
5.9ZrA	15 ± 1	13 ± 0.5	57 ± 0.5
8.4ZrA	16 ± 1	14 ± 0.5	50 ± 0.5
13.6ZrA	13 ± 1	15 ± 0.5	47 ± 0.5
49.7ZrA	12 ± 1	11 ± 0.5	53 ± 0.5
79.4ZrA	12 ± 1	11 ± 0.5	51 ± 0.5

Scanning electron microscopy (SEM) studies

SEM was used to demonstrate powder uniformity. Figure **2.3** shows that SEM resolution is insufficient to reveal individual particles but does provide a view of the general particle population. These SEMs indicate that the particle populations produced here do not include any obvious micron size particles. Bell and Rodriguez[25] recently demonstrated that LF-FSP δ-Al_2O_3 nanopowders disperse perfectly in water without any apparent agglomeration or the presence of micron size particles.[16,25]

(a)

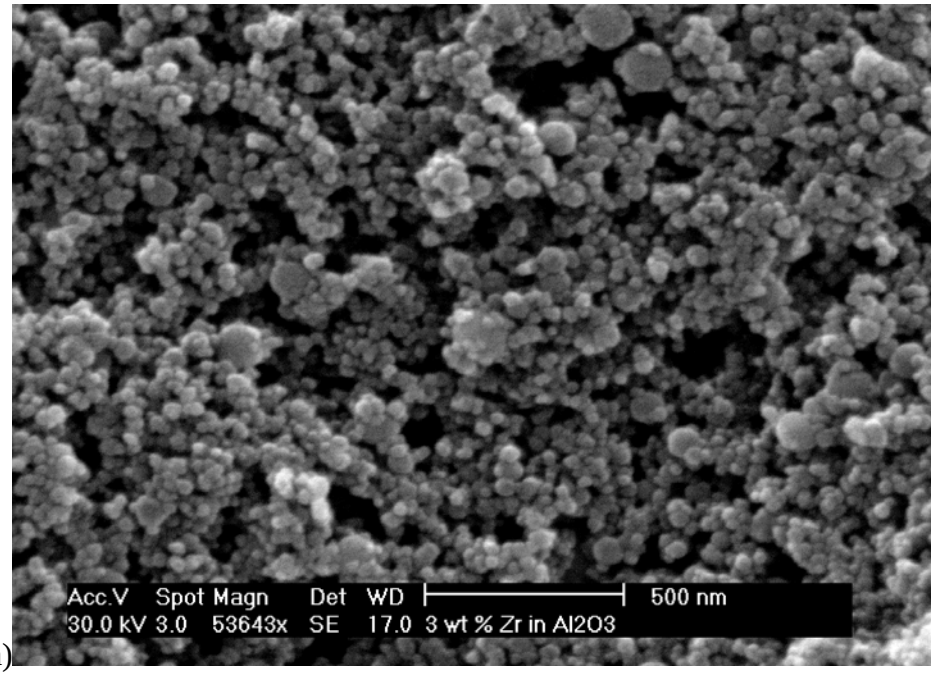

(b)

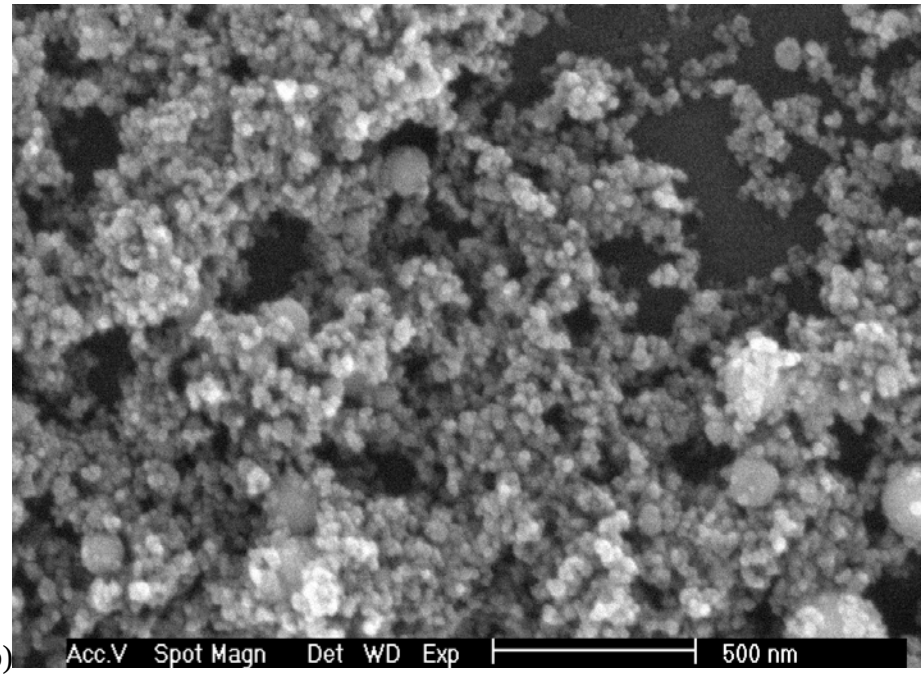

Figure 2.3. SEM images of (a) 2.4 mole% ZrO_2 in Al_2O_3.
(b) 79.4 mole % ZrO_2 in Al_2O_3.

Transmission electron microscopy (TEM) studies of particle morphologies

TEM images were used to assess particle morphologies and sizes of as-prepared powders. Discussions of actual size/size distributions are not appropriate if based solely on TEM micrographs, unless combined with the XRD results. The Figure **2.4** images are high-resolution TEM micrographs of $(ZrO_2)_x(Al_2O_3)_{1-x}$ nanopowders. The particle sizes here are typically below 30 nm in diameter with the vast majority < 20 nm.

In Figure **2.4**, clear lattice fringes show a high degree of crystallinity and strain, especially in the high zirconia content sample (49.7 mole % ZrO_2 in Al_2O_3, 79.4 mole % ZrO_2 in Al_2O_3). The lattice fringes are multi-directional and strain directions are different and multi-faceted in single particles which is likely a consequence of particle formation during rapid quench from the gas phase.

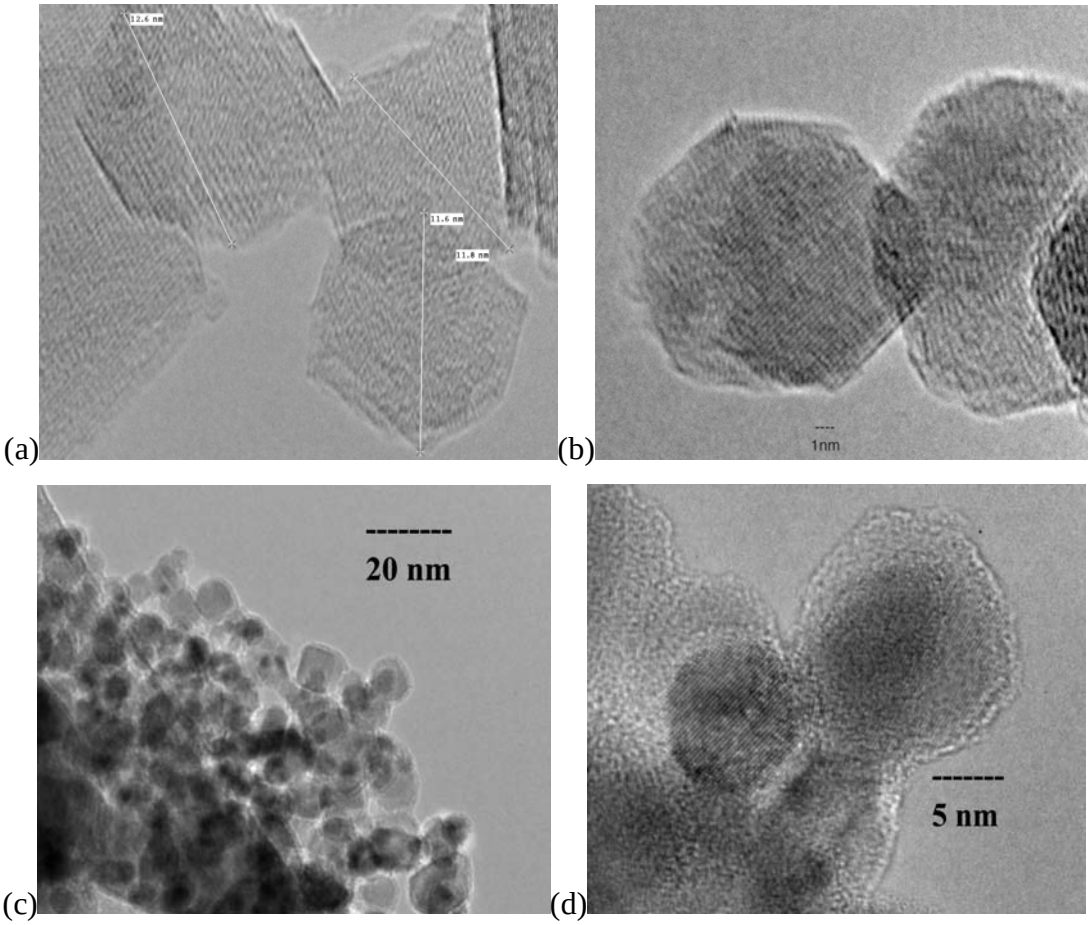

Figure 2.4. TEM micrographs of (a) 4.1 mole%, (b) 49.7 mole % ZrO_2 in Al_2O_3. (c),(d) 79.4 mole % ZrO_2 in Al_2O_3.

The highest zirconia content sample (79.4 mole % ZrO_2 in Al_2O_3) images show the formation of core-shell materials. This corroborates the XRDs of Figure **2.2** indicating phase segregation between t-zirconia and δ-alumina. Since Al_2O_3 has a lower vaporization temperature (3000 ^oC) than ZrO_2 (5155 ^oC) in LF-FSP, ZrO_2 should condense and nucleate first from the gas phase followed by Al_2O_3. We assume that t-zirconia nanoparticles form first during quenching, then δ-alumina nucleates on the t-zirconia nanoparticles forming the observed core-shell nanopowders in single step.

In the low zirconia content sample (4.1 mole% ZrO_2 in Al_2O_3), the lattice fringes are uniform. Combined with XRD, the co-existence of t-zirconia and δ-alumina is easily observed in the high ZrO_2 content sample, while δ-alumina dominates the low ZrO_2 content samples.

FT-IR studies

Once particle morphologies were characterized, a detailed picture of particle surface chemistries and thermal behavior was developed. These studies began with FTIR examination of the particle surfaces per Figure **2.5**.

All of the materials exhibit weak νOH absorptions in the 3700-3000 cm^{-1} region, attributable to surface hydroxyls arising from both physi- (3500 ~ 3000 cm^{-1}) and chemi-sorbed (3500 ~ 3700 cm^{-1}) water.[26] These bands are associated with the 1-4 % mass losses seen at ≤ 400 °C in the TGA studies below.

From 1800 to 1400 cm^{-1}, peaks attributable to surface confined CO_2 and carbonates are observed as expected and in accord with those seen for pure δ-Al_2O_3[27]. Bands in the 1000-400 cm^{-1} region correspond to tetrahedrally coordinated νAl-O at 810 cm^{-1} and octahedrally coordinated νAl-O at 610 cm^{-1}.[28] νZr-O stretching vibrations are found at 700 cm^{-1}.[29]

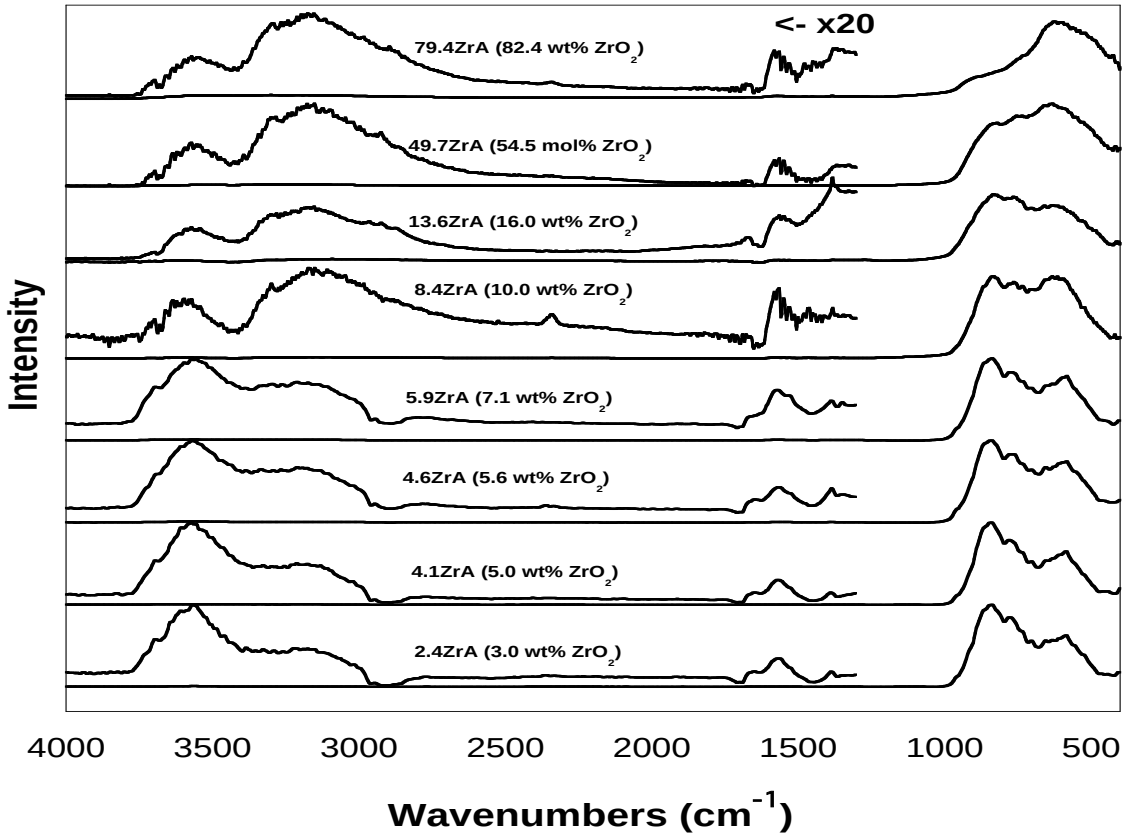

Figure 2.5. FTIR spectra of $(ZrO_2)_x(Al_2O_3)_{1-x}$. 2.4ZrA denotes 2.4 mole % ZrO_2.

TGA-DTA studies

Figure **2.6a** shows mass loss events for as-processed $(ZrO_2)_x(Al_2O_3)_{1-x}$ composition nanopowders. All powders exhibit 1-4 wt% mass losses up to ≈ 400°C. Much of this, up to ≈ 350°C, is attributed to evolution of both physi- and chemisorbed water from particle surfaces. Mass losses between 350° and 400°C are attributed to decomposition of the carbonate species.

The δ to α alumina phase transformation is observed as exotherms above 1300°C in the DTA (Figure **2.6b**). Coincidentally we also see slight mass gains in the TGA (Figure **2.6a**) simultaneously, except for the 79.4 mol % ZrO_2 sample. The most reasonable explanation for these mass gains is oxidation of some unknown $Zr^{2+/3+}$ species. However their appearance, especially at relatively low ZrO_2 contents, requires some discussion.

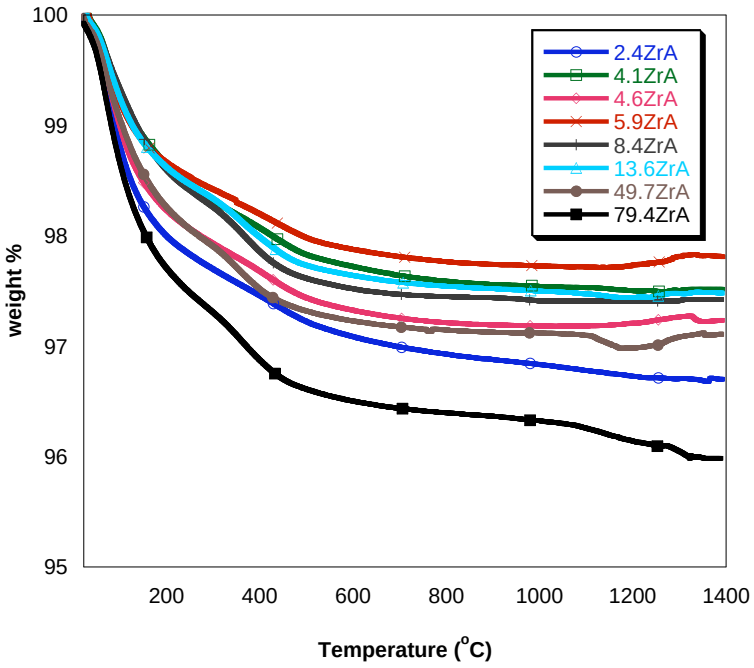

(a)

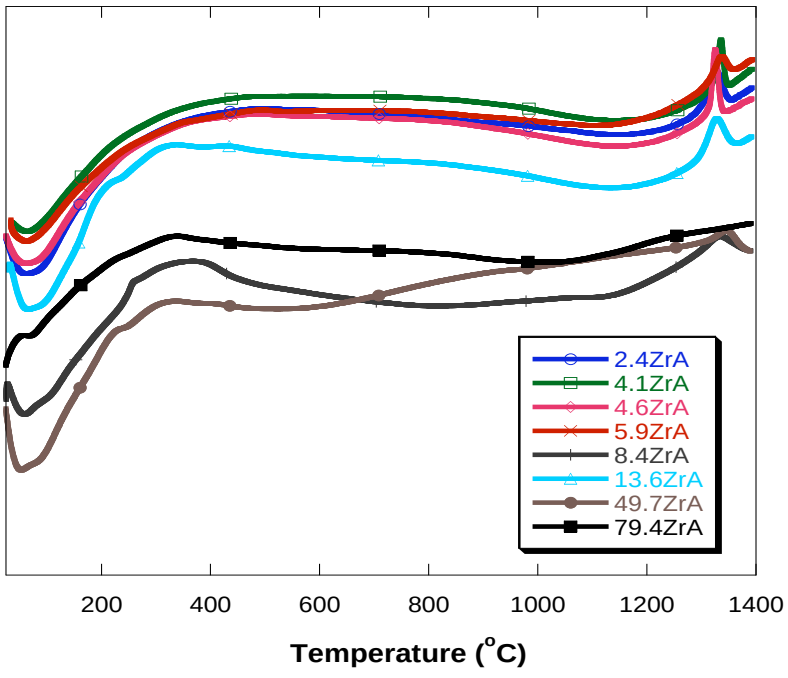

(b)

Figure 2.6. a. TGA of as-processed $(ZrO_2)_x(Al_2O_3)_{1-x}$ ramped at 10°C/min/air. **b.** DTA of as-processed $(ZrO_2)_x(Al_2O_3)_{1-x}$ ramped at 10°C/min/air.

From the literature, the solubility of zirconia in δ-alumina is less than 0.03 wt%,[30-34] and zirconia is essentially insoluble in α-alumina.[33,34] We presume that some $Zr^{2+/3+}$ ions are produced during LF-FSP and form solid solutions perhaps as a spinel phase

($ZrAl_2O_4$) or some unknown form (e.g. $ZrAlO_3$). Similar observations were made for Ti aluminate in previous studies.[35,36] We presume that these $Zr^{2+/3+}$ ions segregate out during the δ to α alumina transformation and oxidize to ZrO_2. The maximum mass gain of 0.2 wt% is assumed to be oxygen as these Zr ions oxidize to ZrO_2.

In Table **2.3**, we estimate the possible maximum amounts of $Zr^{2+/3+}$ ions from the mass gains. Here we assume that the Zr species formed during LF-FSP are all either Zr^{2+} or Zr^{3+} ions without mixed states. We assume that the dissolved Zr^{3+} ions form coincident with oxygen vacancies. From this study, we find that the amount of dissolved zirconia (assuming ZrO/Zr_2O_3 stoichiometries) is greater than the solubility limit of zirconia in δ-alumina reported in the literature.[30-34]

Table 2.3. Possible maximum portions of dissolved $Zr^{2+/3+}$ ions in δ-alumina.

Sample	Mass gain	Possible maximum Zr^{2+} * (mol ± 0.1 %)	Possible maximum Zr^{3+} † (mol ± 0.1 %)
2.4 ZrA	0.07 wt %	0.4	0.6
4.1 ZrA	0.09 wt%	0.5	0.7
4.6 ZrA	0.14 wt%	0.9	1.4
5.9 ZrA	0.2 wt%	1.2	1.8
8.4 ZrA	0.2 wt%	1.2	1.8
13.6 ZrA	0.2 wt%	1.2	1.8
49.7 ZrA	0.2 wt%	1.3	2.0

* Assumes all reduced species are Zr^{2+} (ZrO)
† Assumes all reduced species are Zr^{3+} (Zr_2O_3)

As with many of our previous studies, LF-FSP materials generated by rapid quenching lead to novel kinetic products not expected based on traditional processing methods that typically drive formation through thermodynamic assaults on particle mixtures. Since traditional processing methods lead to thermodynamically rather than kinetically defined phase compositions, these materials may offer unique opportunities for catalyst and fuel cell applications.

Zr^{3+} in Al_2O_3 may also offer utility in photonic applications. For example, Ti^{3+} in an α-alumina (Ti^{3+} doped sapphire) is widely-used as a laser material.[37-39] The amount of Ti^{3+} dissolved in sapphire (α-alumina) commercial lasers is usually 0.05~1.0 wt %. For a Ti^{3+} ion substitutionally incorporated in an Al^{3+} lattice site, the degenerate $3d^1$ electron

energy level is split under the influence of the local crystal field.[40] As a result, an optical transition arises leading to strong electron–phonon coupling that broadens the optical transition vibronically. Excitation to upper levels is characterized by strong absorption in the blue-green, and a radiative relaxation to the lower level gives rise to the broad fluorescence band that extends from 600 to 1050 nm.[40,41]

Since we find similar amounts of Zr^{3+} (assumed) dissolved in δ-alumina from our TGA-DTA studies and Ti^{3+}/Zr^{3+} ions have same valence electron configuration ($[Ar]3d^1$ for Ti^{3+} and $[Kr]4d^1$ for Zr^{3+}), we may expect photonic properties for our Zr^{3+} in Al_2O_3.

Finally, the identification of a method of forming core-shell nanoparticles suggests multiple opportunities for novel processing of ZTA materials for forming duplex structures and for superplastic deformation.[42,43] We plan to test this approach in the near future.

2.5 Conclusions

LF-FSP provides access to mixed-metal oxide nanopowders with exceptional control of stoichiometry and phase purity. Here we have succeeded in preparing nanopowders of any composition in ZrO_2-Al_2O_3 tieline with specific surface area of ≈ 50 m^2/g at rates of 100-300 g/h. Furthermore we have demonstrated access to core-shell nanoparticles in the $(ZrO_2)_x(Al_2O_3)_{1-x}$ system that may offer novel potential for processing dense, defect free ZTA composite materials.

Since LF-FSP enables rapid quenching of the combustion species, it offers access to new, kinetic materials not accessible by other conventional processing method. Thus, we were able to observe what appears to be the presence of of $Zr^{2+/3+}$ ions in Zr-Al-O binary system. These nanopowders may offer utility in photonic applications anticipated based on Ti doped sapphire lasers.

2.6 References

1. M.W. Pitcher, S .V. Ushakov, A. Navrotsky, B.F. Woodfield, G. Li, J. Boerio-Gooates "Energy crossovers in nanocrystalline zirconia" *J. Am. Ceram. Soc.* **88** [1] 160-167

2. R. Mueller, R. Jossen, S.E. Pratsinis, M. Watson, M.K. Akhtar " Zirconia nanoparticles in spray flames at high priduction rates" *J. Am. Ceram. Soc.* **87** [2] 160-167

3. T. Klimova, M. L. Rojas, P. Catillo, R. Cuevas, J. Ramirez " Characterization of Al_2O_3-ZrO_2 mixed oxide supports prepared by the sol-gel method." *Microporous and mesoporous materials* **20** (1998) 293-306

4. H. Neumann, G. Hotzel, G. Lindermann "Advanced planar oxygen censors for future emission control strategies" SAE 970459 (1997)

5. S. Park, J. M. Vohs, R.J. Gorte " Direct oxidation of hydrocarbons in a solid-oxide fuel cell" *Nature* 404 (2000) 265-267

6. Y. Kim, J. Koo, J. Han, S. Choi, H. Jeon, C. Park " Characteristics of ZrO_2 gate dielectric deposited using Zr t-butoxide and $Zr(NEt_2)_4$ precursors by plasma enhanced atomic layer deposition method" *J. App. Phy.* 92(9) 2002 5443-5447

7. M. Zhu, P. Chen, R. Fu, W. Liu, C. Lin, P. Chu "Microstructure and electrical properties of Al_2O_3-ZrO_2 composites films for gate dielectric applications" *Thin solid films* **476** (2005) 312-316

8. T. Aruna, K. S. Rajam "Mixture of fuels approach for the solutions combustion synthesis of Al_2O_3-ZrO_2 nanocomposite" *MRS Bulletin* **39** (2004) 157-167

9. G. Magnani, A. Brillante "Effects of the composition and sintering process on mechanical properties and residual stresses in zirconia-alumina composites" *J. Eur. Cer.Soc.* **25** (2005) 3383-3392

10. D. Casellas, M. M. Nagl, L.Llanes, M. Anglada " Microstructural Coarsening of Zirconia-Toughened Alumina Composites" *J. Am. Ceram. Soc.* **88** [7] 1958-1963

11. J. S. Moya, H. P. Steier, J. Requena "Interfacial reactions in aluminum alloys/mullite-zirconia composites" *Composites Composites: Part A* 30 (1999) 439-444.

12. A. C. Sutorik, S. S. Neo, T. Hinklin, R. Baranwal, D.R. Treadwell, R.Narayanan, R.M. Laine, "Synthesis of Ultrafine β"-Alumina Powders via Flame Spray Pyrolysis of Polymeric Precursors," *J. Am. Ceram. Soc*. **81**, 1477-86 (1998).

13. R. Baranwal, M. P. Villar, R. Garcia and R. M. Laine, "Synthesis, Characterization, and Sintering Behavior of Nano-mullite Powder and Powder Compacts," *J. Am. Ceram. Soc.* **84**, 951- 61 (2001).

14. C.R. Bickmore, K.F. Waldner, R. Baranwal, T. Hinklin, D.R. Treadwell, R.M. Laine, "Ultrafine Titania by Flame Spray Pyrolysis of a Titanatrane Complex: Part I," *J. Europ. Ceram. Soc*. **18**, 287-97 (1998).

15. J. Marchal, T. Hinklin, R. Baranwal, T. Johns, R. M. Laine, "Yttrium aluminum garnet nanopowders by flame spray pyrolysis," *Chem. Mater*. **16**, 822-831 (2004).

16. T. Hinklin, B. Toury, C. Gervais, F. Babonneau, J.J. Gislason, R.W. Morton, R.M. Laine "Liquid-Feed Flame Spray Pyrolytic Synthesis of Nanoalumina Powders," *Chem. Mater*. **16**, 21-30 (2004).

17. S. Kim, J.J. Gislason, R.W. Morton, X. Pan, H. Sun, R.M. Laine, "Liquid-Feed Flame Spray Pyrolysis of Nanopowders in the Alumina-Titania System" *Chem. Mater*. **16**, 2336-43 (2004).

18. J. A. Azurdia, J. Marchal, P. Shea, H. Sun, X. Q. Pan, R. M. Laine " Liquid-Feed Flame Spray Pyrolysis as a Method of Producing Mixed-Metal Oxide Nanopowders of Potential Interest as Catalytic Materials. Nanopowders along the $NiO\text{-}Al_2O_3$ Tie Line Including $(NiO)_{0.22}(Al_2O_3)_{0.78}$, a New Inverse Spinel Composition" *Chem. Mater.* **18** (2006) 731-739

19. X. Zhou, D .M. Hulbert, J. D. Kuntz, R. K. Sadangi, V. Shukla, B. H. Kear, A. K. Mukherjee "Superplasticity of Zirconia-alumina-spinel nanoceramic composite by spark plasma sintering of plasma aprayed powders" *Mater. Sci. Eng. A* 394 (2005) 353-359

20. M. Kim, R. M. Laine Unpublished work.

21. T. Hinklin, B. L. Mueller, R. M. Laine, U.S. Patent 5,418,298, 1995

22. R.narayanan, R. M. Laine "Synthesis and characterization of precursors for group II metal aluminates" *App. Org. Chem.* **11** (1997) 919-927

23. V. V. Srdic, M. Winterer "Aluminum-Doped Zirconia Nanopowders: Chemical Vapor Synthesis and Structural Analysis by Rietveld Refinement of X-ray Diffraction Data" *Chem. Mater*. **2003**, 15, 2668-2674

24. V. V. Srdic, M. Winterer, H. Hahn " Sintering Behavior of Nanocrystalline Zirconia Doped with Alumina Prepared by Chemical Vapor Synthesis." *J. Am. Ceram. Soc.* **83** [8] 1853-1860

25. N. S. Bell, M.A. Rodriguez, "Dispersion properties of an alumina nanopowder using molecular, polyelectrolyte, and steric stabilization" *J. Nanosci. Nanotech.* **2004**, 4(3), 283-290

26. J. B. Peri, “Infrared and gravimetric study of the structure hydration of γ-alumina” *J. Phys. Chem*. **1965**, 69, 211

27. J. M. Saniger, *Mater. Lett.* “ Al-O infrared vibrational frequencies of γ-alumina” **1995**, 22, 1995

28. P. Tarte. “Infrared spectra of inorganic aluminates and characteristic vibrational frequencies of AlO_4 tetrahedra and AlO_6 octahedra” *Spectrochim. Acta* **1967**, 23A, 2127

29. J. Chandradass, M. Balasubramanian “ Sol-gel processing of alumina-zirconia minispheres” *Ceram. Int*. 31, 5, 2005, 743-748

30. M. A. Stough, J. R. Hellmann “ Solid Solubility and precipitation in a single-crystal Alumina-Zirconia system” *J. Am. Ceram. Soc*. **85** [12] (2002) 2895-2902

31. M. K. Loudjani, R. Cortes “Study of the local environment around zirconium ions in polycrystalline α-alumina in relation with kinetics of grain growth and solute drag” *J. Europ. Ceram. Soc*. **20** (2000) 1483-1491

32. D. A. Jerebtsov, G. G. Mikhailov, S. V. Sverdina “Phase Diagram of the system : Al_2O_3- ZrO_2” *Ceram. Int.* **26** (2000) 821-823

33. B. Djuricic, S. Pickering, P. Glaude, D. Mcgarry, P. Tambuyser “Thermal stability of transition phases in zirconia-doped alumina” *J. Mater. Sci*. **32** (1997) 589-601

34. O. Fabrichnaya, F. Aldinger “Assessment of thermodynamic parameters in the system ZrO_2-Y_2O_3-Al_2O_3” *Zeitschrift fur metallkunde* **95** (2004) 27-39

35. M. Grinberg, A. Mandelis, K. Fjeldsted “Theory of interconfigurational nonradiative transitions in transition –metal ions in solids and applications to the Ti^{3+}: Al_2O_3 system” *Phys. Rev. B* 48 [9] (1993) 5935-5944

36. T. Mizoquchi, M. Sakurai, A. Nakamura. K. Matsunaga, I. Tanaka, T. Yamamoto, Y. Ikuhara “Valence state of Ti in conductive nanowires in sapphire.” *Phys. Rev. B* 70 153101 (2004)

37. T. Amthor, M. Sinther, T. Walther “An injection-locked, single-mode, continuous wave Ti:Sapphire laser” *Laser Phys. Lett.* **3** (2006) 75–78

38. J. Philip, C. D’Amico, G. Che´riaux, A. Couairon, B. Prade, A. Mysyrowicz “Amplification of Femtosecond Laser Filaments in Ti:Sapphire” *Phys. Rev. Lett.* October (2005) 95, 163901

39. A.Mandelis, J. Vanniasinkim, S. Budhudu, A. Othonos, M. Kokta “ Absolute nonradiative energy-conversion-efficiency spectra in Ti^{3+} : Al2O3 crystals measured

by contact quadrature photopyroelectric spectroscopy" *Phys. Rev. B* **48[10]** (1993) 6808- 6821

40. L. M. B. Hickey, E. Martins, J. E. Rom´an, W. S. Brocklesby, J. S. Wilkinson "Fluorescence of Ti^{3+} ions thermally diffused into sapphire" *Opt. Lett.* **21[8]** (1996) 597-599

41. K. Morinaga, H. Yoshida, H. Takebe "Compositional Dependence of Absorption Spectra of Ti^{3+} in Silicate, Borate, and Phosphate Glasses" *J. Am. Ceram. Soc*. **77** [12] (1994) 3113-3118

42. A. J. A. Winnubst, M. M. R. Boutz, Y. J. He, A. J. Burggraaf, H. Verweij, *Ceram. Int.* 23 (1997) 215-221.

43. S. Ishihara, T. Tanizawa, K. Akashiro, N. Furushiro, S. Hori, *Mater. Trans. JIM* 40(10) (1999) 1158-1165.

CHAPTER 3
CORE-SHELL NANOSTRUCTURED NANOPOWDERS ALONG $(CeO_x)_x(Al_2O_3)_{1-x}$ TIE-LINE

3.1 Abstract

We report here the synthesis of $(CeO_x)_{1-x}(Al_2O_3)_x$ mixed-metal oxide nanopowders with molar ratios that span the CeO_x-Al_2O_3 composition range. Liquid-feed flame spray pyrolysis (LF-FSP) of mixtures of $N(CH_2CH_2O)_3Al$ (alumatrane) and $Ce(CH_3CH_2COO)_3(OH)$ precursors dissolved in ethanol, were aerosolized with O_2, combusted at temperatures of 1500-2000 °C and rapidly quenched thereafter to provide $(CeO_x)_{1-x}(Al_2O_3)_x$ nanopowders of selected compositions. All powders exhibit average particle sizes (APSs) < 20 nm and corresponding surface areas of ≥ 50 m^2/g when produced at rates of 100-300 g/h. The as-processed powders were characterized in terms of phase, size, specific surface area, composition, and morphology by BET, XRD, XRF, SEM, TEM, STEM, XEDS, FT-IR, and TGA-DTA. Surprising core-shell nanostructured nanopowders are observed in the Ce-Al-O system at CeO_x rich concentrations (≥ 15 mole %). In addition, evidence is presented for the incorporation of Ce^{3+} ions in the δ-alumina lattice at the lowest concentrations and Ce-magnetoplumbite ($CeAl_{11}O_{18}$) at 5-10 mole % CeO_x concentrations.

Key Words: core-shell nanostructured nanoparticles, liquid-feed flame spray pyrolysis, $(CeO_x)_{1-x}(Al_2O_3)_x$ nanopowders, $(CeO_x)_{1-x}(Al_2O_3)_x$ tieline, Ce-Magnetoplumbite

3.2 Introduction

Ceria-based mixed-metal oxides are important candidates for a wide range of applications. Besides well-known catalytic applications related to the reversible Ce^{4+}/Ce^{3+} redox couple,[1-3] mixed-metal oxides with ceria are currently receiving attention as phosphors,[4-6] chemical mechanical polishing (CMP) slurries,[7,8] cutting tools (ceria toughened alumina),[9] and oxygen transport media for solid oxide fuel cells (SOFC).[10-12]

The ceria-alumina mixed-metal oxide system is of particular interest for catalytic applications, since rare earth (RE) species have the potential to stabilize high surface area transition aluminas.[13] These materials have been a topic of significant research,[14,15] because the gradual sintering and transformation of $\gamma\text{–}Al_2O_3$ into $\alpha\text{–}Al_2O_3$ above 1000°C coarsens the alumina substrate leading to loss of catalytic activity due to the reduction of the accessible surface area of the catalyst and changes in the acid/base surface chemistry.

For ceria-alumina binary systems, highly dispersed Ce^{3+} ions form $CeAl_{11}O_{18}$ and $CeAlO_3$ by solid-state interaction between Al_2O_3 and CeO_x at $\geq$ 5 mole% ceria compositions.[16,17,39,40] In this case, Ce^{3+} ions replace Al^{3+} in the transition alumina lattice increasing the thermal stability of δ-alumina by forming metastable Ce-magnetoplumbite ($CeAl_{11}O_{18}$) thereby halting Al_2O_3 grain growth.[39,40] It has been reported that the addition of rare earth (RE) ions to transition alumina-supported Pd catalysts not only reduces sintering of the alumina support at higher temperatures (around 1000 ^oC), but also retards sintering of the supported Pd.[16-18]

While stabilization of surface area is a classical field of study for rare-earth doped transition aluminas, our interest in these materials centers on their emissive behavior for potential use as laser paints and for other photonic applications.[19-21] Thus, we recently reported lasing behavior from RE doped mixed-metal oxide nano-composites under cathodoluminescence conditions.[20,21] In related systems, we demonstrated that RE doped mixed-metal oxide nanopowders offer novel UV emission behavior.[20,21] This research is potentially relevant to improving phosphors for field emission displays, x-ray imaging, nanocomposite lasers and other photonic applications.[22-24]

All nanopowders used in these previous studies were synthesized using LF-FSP, which offers the potential to make a wide variety of single and mixed-metal oxide nanopowders in a single step.[25-32] The LF-FSP process aerosolizes metalloorganic precursors dissolved in an alcohol solvent with oxygen, combusts the aerosol within a quartz chamber at ≥ 1500 ^{o}C, and then rapidly quenches the gaseous species to produce nanosize oxide "soot" with the same compositions as those in the starting precursor solutions. See the experimental section below for details.

To date, we have used LF-FSP to make phase-pure nanopowders of single and mixed-metal oxides including Al_2O_3, CeO_2, ZrO_2, TiO_2, CoO and NiO.[26-32] These LF-FSP as-produced nanopowders are typically unaggregated with specific surface areas (SSAs) of 30-50 m^2/g and average particle sizes (APSs) of 15-30 nm.

We have focused on oxide systems that offer potential for catalytic and/or photonic applications.[29-32] According to these studies, LF-FSP is proven to be a low-cost, single step route to versatile materials in mixed-metal oxide systems, and provides easy access to many types of metal oxide nanopowders with excellent control of phase purity and morphology. These nanopowders in turn offer potential access to a wide variety of dense ceramic source materials for catalytic, mechanical, photonic, electrical, and electronic applications.

Here we use LF-FSP to explore the synthesis and properties of nanopowders along the $(CeO_x)_x(Al_2O_3)_{1-x}$ tieline. Unlike previous studies on ceria-alumina mixed-metal oxides materials,[1-12] we find new nanostructured nanopowders for each composition. As with other LF-FSP products, the resulting unaggregated nanopowders offer specific surface areas (SSAs) $\geq$ 50 m^2/g and average particle sizes (APSs) less than 20 nm without microporosity.

Surprisingly, LF-FSP with the correct choice of metalloorganic precursors provides access to core-shell nanopowders in a single step for certain composition of $(CeO_x)_x(Al_2O_3)_{1-x}$.

3.3 Experimental

Liquid-feed flame spray pyrolysis (LF-FSP)

LF-FSP, as invented at the University of Michigan, has been described in detail in published papers.[25-32] Briefly, alcohol (typically EtOH) solutions containing 1-10 wt % loading of ceramic as precursors, e.g. single- or mixed-metal alkoxides, carboxylates or β-diketonates are aerosolized with O_2 into a 1.5 m long quartz chamber where it is ignited with methane pilot torches.

Initial combustion temperatures run 1500°-2000°C, depending on the processing conditions, generating nanopowder "soot." Temperatures drop to 300-500 °C over 1.5 meters, equivalent to a 1000°C quench in ≤ 100 msec leading to kinetic products and nanopowders that are largely unaggregated; although they are lightly agglomerated. "Shooting" rates can be 200 g/h when using wire-in-tube electrostatic precipitators operating at 10 kV. Typical powders are 15 to 100 nm APS with specific surface areas (SSAs) of 30 to 100 m^2/g. When combinations of elements are used, the resulting nanopowders will have compositions identical to those of the precursor solutions. Since compositions of chemical solutions can be changed intentionally, potentially even during mixing just before aerosolization, it becomes possible to combinatorially produce mixed-metal oxide materials. Hence it becomes possible to rapidly optimize materials for given properties or for ease of processing.

Materials

Alumatrane. $N(CH_2CH_2O)_3Al$ prepared as described previously[33,34] is used as the alumina source.

Cerium propionate. Cerium carbonate [$Ce_2(CO_3)_3 \cdot x(H_2O)$, 99%, 70 g, 0.15 mole] was reacted with excess propionic acid (400 mL, 5.44 mole) in a 1 L flask equipped with a still head and an addition funnel. N_2 was sparged directly through the solution (2 psi pressure) as the solution was heated at 120 ˚C/2h to distill off ~150 mL of liquid (water and propionic acid). The ceramic loading of the resulting precursor was 9 wt% as determined by TGA.

XRD studies

As-prepared samples were characterized using a Rigaku Rotating Anode Goniometer. Powder samples were prepared by placing ≈ 100 mg on XRD sample

holders (amorphous silica slides) for data collection. CuKα (λ = 1.54 Å) radiation with a Ni filter was used with a working voltage and current of 40 kV and 100 mA, respectively. Scans were continuous from 10–80° 2θ with a step scan of 2° 2θ/min in increments of 0.05° 2θ. Peak positions and relative intensities were characterized by comparison with PDF files of standard materials: CeO_2 (PDF file 4-002-2713), δ^*-Al_2O_3 (PDF file 46-1215), $CeAl_{11}O_{18}$ (PDF file 00-048-0055) Debye-Scherer line broadening was used to calculate average particle sizes (APS) from the XRD powder patterns.

X-ray Fluorescence (XRF)

Chemical analyses were obtained by X-ray fluorescence (XRF) from Ford motor company (Dearborn, MI). Samples were prepared by mixing 0.50g of sample into 10.0g of $Li_2B_4O_7$ glass flux. The sample and glass flux were mechanically stirred for 5 minutes in a methacrylate vial with three methacrylate balls using a SPEX 6000 ball mill. The mixtures were fused into glass beads by placing them in an oven held at 1000˚C for 10 min. The samples were analyzed using a Panalytical PW2400 X-Ray Fluorescence spectrometer (formerly Philips), equipped with a WDS detection system (wavelength dispersive).

Thermal Gravimetric Analysis and Differential Thermal Analysis (TGA/DTA)

TGA-DTA were performed using a SDT 2960 Simultaneous Differential Thermal Analyzer (TA Instruments, Inc., New Castle, DE). The instrument was calibrated with gold supplied by Perkin-Elmer. Samples (70 mg) of as-prepared powders were hand pressed in a 3 mm dual action die and placed inside Pt sample cups and heated at ramp rates of 10˚C/min from ambient temperature to 1400˚C. The reference material was a pellet of α-alumina. A flow of synthetic air, 50 ml/min, was maintained during all experiments.

Specific surface area (SSA)

SSA was measured on a Micromeritics ASAP 2000 sorption analyzer. Samples (200 mg) were degassed at 400°C until the outgas rate was 5 mmHg/min. Analyses was run at 77K with N_2. SSAs were determined by the BET multipoint method using at least five data points with relative pressures of 0.001-0.20. The average particle size was

derived using the formula $< R >= \frac{3}{\rho \times SSA}$ where <R> = average particle size in diameter, and ρ is the density of the material.

Scanning electron microscopy (SEM)

A high resolution SEM (FEI NOVA Dual beam focused ion beam workstation and scanning electron microscope) was used to image powder morphologies. Powder samples were dispersed in distilled H_2O using an ultrasonic horn (Vibra-cell, Sonics and Materials, Inc., Newton, CT). A drop of the dispersed powder/water was placed on an aluminum SEM stub and allowed to dry for 4 h on a hot plate. Powders were sputter coated with 1-5 nm of Au-Pd to reduce charging effects. The operating voltage was 15.0 kV.

Transmission electron microscopy (TEM)

An analytical high resolution TEM (Model 3011, JOEL, Osaka, Japan) was used to measure the particle sizes and morphologies of as-prepared powders. Powder samples were prepared by dipping a holey carbon grid in a vial of emulsion with as-prepared powder. The specimen was held in a Gatan double tilt goniometer. An operating voltage of 300 kV was used.

Scanning transmission electron microscopy (STEM)/X-ray energy dispersive spectroscopy (XEDS)

An analytical STEM (Model 2010, JOEL, Osaka, Japan) with X-ray Energy Dispersive Spectroscopy (XEDS) was used to determine core and shell elements of nano-sized particles. Same samples from high resolution TEM were used. The operating voltage was 200 kV.

FTIR spectra.

Diffuse reflectance Fourier transform (DRIFT) spectra were recorded on a Thermo Fisher Scientific Nicolet 6700 FTIR spectrometer (Thermo Fisher Scientific, Inc., Madison, WI.). Optical grade, random cuttings of KBr (International Crystal Laboratories, Garfield, NJ) were ground, with 1.0 wt % of the sample to be analyzed. For DRIFT analysis, samples were packed firmly and leveled off at the upper edge to provide a smooth surface. For transmission IR, 100 mg of each sample prepared for DRIFT analysis was pressed in a stainless steel double action die (12.75 mm diameter) at 100

MPa for 1 min in a Carver Press (model 3912). Fresh backgrounds of pure KBr were done every hour. The FTIR sample chamber was flushed continuously with N_2 prior to data acquisition in the range 4000-400 cm^{-1}. Each run consisted of 128 scans with a resolution of ± 4 cm^{-1}.

3.4 Results and Discussion

The objectives of the current studies are to produce and characterize high surface area, non-porous nanopowders along the $(CeO_x)_x(Al_2O_3)_{1-x}$ tie-line in one step using LF-FSP as a prelude to exploring their potential utility for catalytic,[1-3] photonic,[4-6] and structural applications.[7-9]

Nanopowders prepared along the $(CeO_x)_x(Al_2O_3)_{1-x}$ tie-line differ from other conventionally prepared nano-materials as noted above, because LF-FSP provides single step access to core-shell nanopowders. Current methods of making coated nanoparticles are mostly based on solution phase methods, and primarily sol-gel processing.[35-38] These types of methods are usually multi-step.[35-38] They usually require homogeneous dispersions of core materials in a solvent, typically by ultrasonication, followed by coating with the shell materials. The latter step often leads to micron-sized final products and aggregation of the core powders is unavoidable unless processing is done at low concentrations. Also, these multi-step processes are inefficient in time, cost and homogeneity of final product.[35-38] In contrast, LF-FSP has the potential to provide simple and efficient routes to nano core-shell nanopowders without aggregation.

In the following section we begin by characterizing the ceria precursor developed for LF-FSP processing. Thereafter we follow with sections on the production of selected nanopowders along the CeO_x-Al_2O_3 tie-line, their particle morphologies, phase compositions, surface chemistries, thermal properties.

Precursor and precursor formation

We previously reported the characterization of alumatrane $[N(CH_2CH_2O)_3Al]$ and its use as a precursor in LF-FSP for the synthesis of δ-alumina nanopowders.[28] Here we report the synthesis and characterization of the precursor, $Ce(O_2CCH_2CH_3)_3(OH)$, as detailed in the experimental section. This precursor has a thermal decomposition pattern similar to other metal carboxylate precursors studied previously.[25-34]

Figure **3.1** shows a TGA trace for $Ce(O_2CCH_2CH_3)_3(OH)$. Initial mass losses (3%) are due to propionic acid of recrystallization and solvent. Thereafter, mass loss events are attributed to decomposition of the propionate ligands as suggested by reactions (1)-(3).

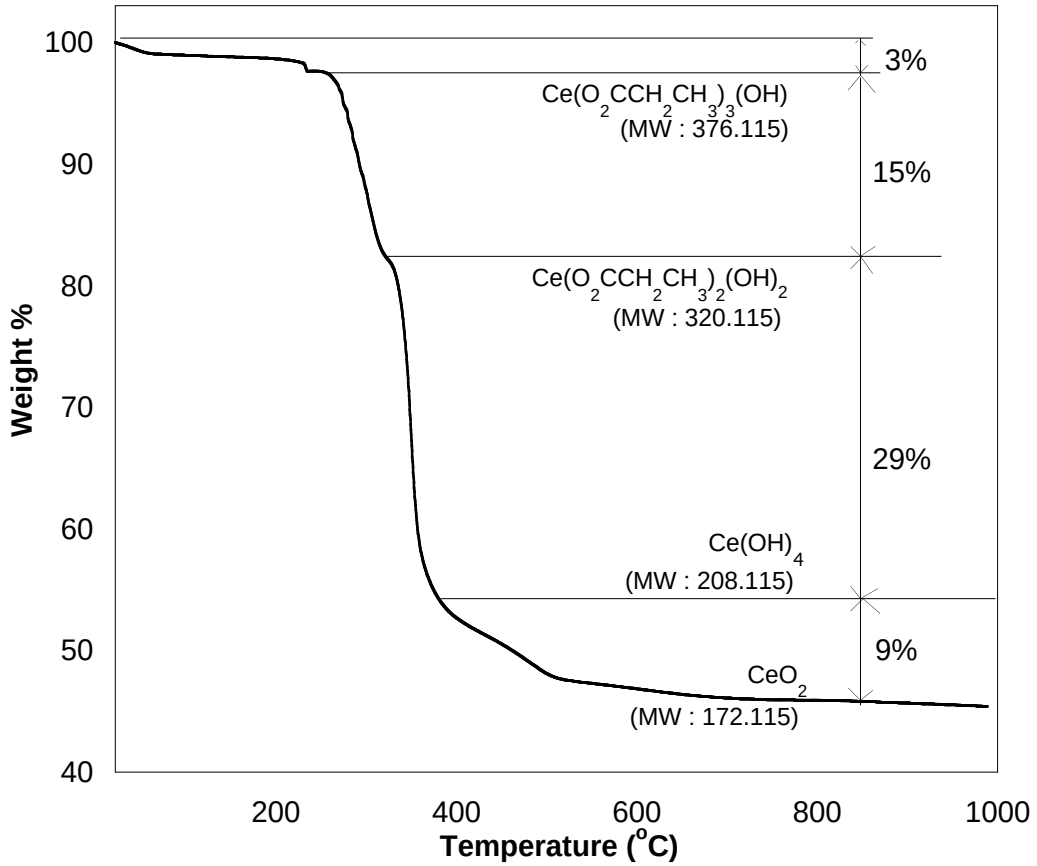

Figure 3.1. TGA of $Ce(O_2CCH_2CH_3)_3(OH)$ ramped at 10°C/min in synthetic air.

$$Ce(O_2CCH_2CH_3)_3(OH) \rightarrow Ce(O_2CCH_2CH_3)_2(OH)_2 + CH_3CH=C=O \quad (1)$$

Mass Loss Calc. (Found) = 14.45% (15%)

$$Ce(O_2CCH_2CH_3)_2(OH)_2 \rightarrow Ce(OH)_4 + 2[CH_3CH=C=O] \quad (2)$$

Mass Loss Calc. (Found) = 28.90% (29%)

$$Ce(OH)_4 \rightarrow CeO_2 + 2H_2O \quad (3)$$

Mass Loss Calc. (Found) = 9.28% (9%)

Final ceramic yields (44% CeO_2) are within experimental error of the calculated values (44.37%) for the decomposition of the precursor [$Ce(CH_3CH_2COO)_3(OH)$] to oxide (CeO_2) and are as expected based on previous studies.[25-34]

Compositions of as-processed nanopowders

Fifteen different precursor compositions in the $(CeO_2)_x(Al_2O_3)_{1-x}$ system were prepared by making simple mixtures of alumatrane and the propionate as detailed in the Experimental. Compositions were confirmed by XRF. These nanopowders were analyzed by XRD, BET, HR-SEM, HR-TEM, STEM, XEDS, FT-IR and TGA-DTA as discussed in the following sections.

XRD powder pattern studies

Figure **3.2** provides XRD patterns for as-produced nanopowders along the $(CeO_x)_x(Al_2O_3)_{1-x}$ tie-line. Samples with CeO_x concentrations ≤ 5 mole % show only the transition alumina phase (δ^*-alumina) found for undoped LF-FSP powders.[28] As noted in a previous publication, at these concentrations, the cerium is present as Ce^{3+} and replaces Al^{3+} in the δ^*-Al_2O_3 lattice as witnessed by its cathodoluminescence behavior.[19,20]

XRD patterns of samples with CeO_x concentrations between 5 - 10 mole % show the presence of both cubic CeO_2 (see below) and evidence that a considerable portion of the Ce^{3+} ions are present as Ce-magnetoplumbite ($CeAl_{11}O_{18}$).[19b] Ce-Magnetoplumbite has a spinel structure separated by hexagonal planes containing Ce^{3+} ions.[39-41] δ^*-alumina or Ce-magnetoplumbite vary only by the number (1 or 3) of oxygen atoms in the rare earth plane, respectively.[39-41]

Powders with concentrations above 10 mole % ceria show only the cubic CeO_2 phase because of the relative high peak intensity of ceria XRD patterns over alumina. However, both cubic ceria and δ^*-alumina co-exist as confirmed by TEM, XEDS and XRF in the following sections.

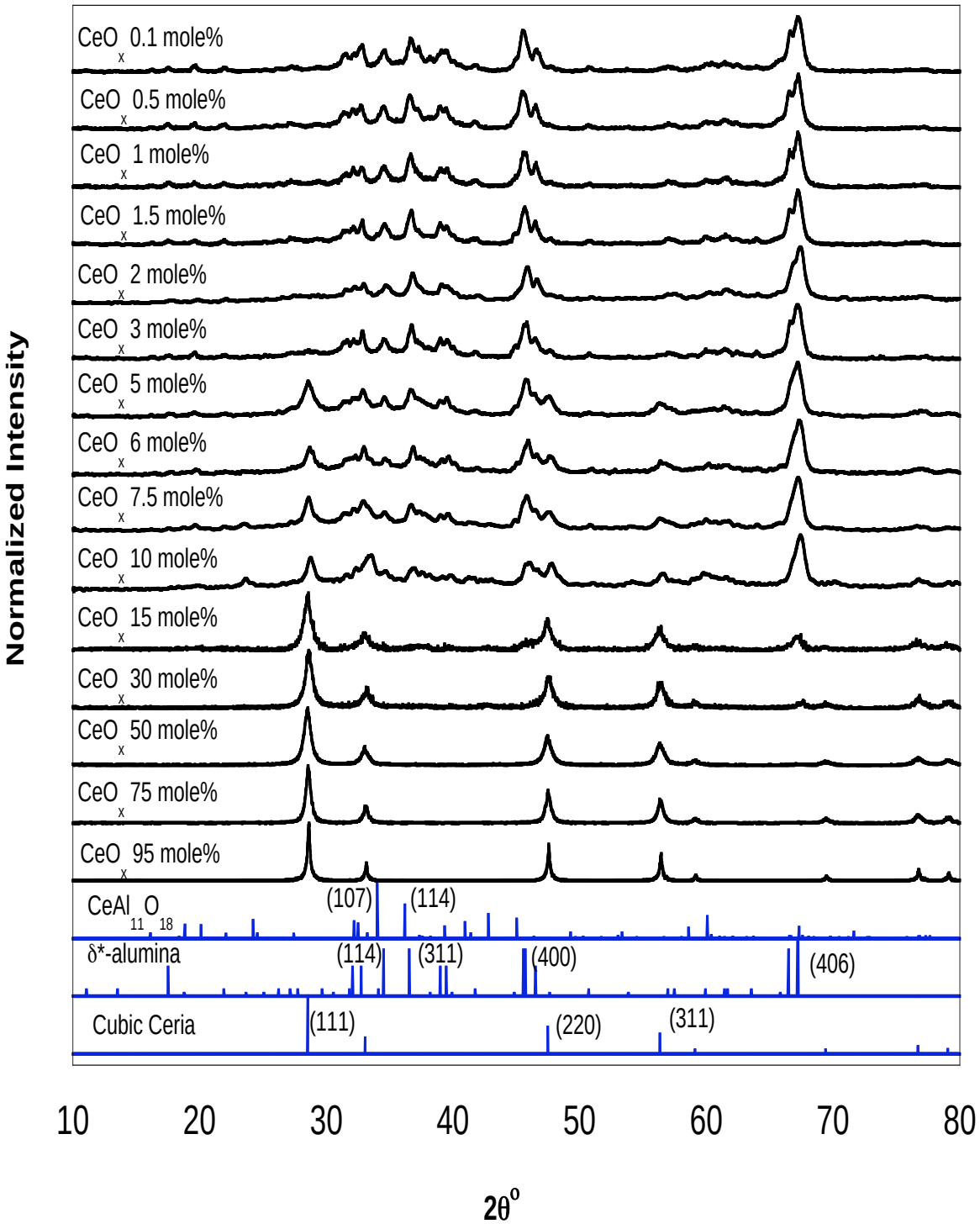

Figure 3.2. XRDs of as-produced $(CeO_2)_x(Al_2O_3)_{1-x}$ nanopowders by LF-FSP. CeO_x (PDF file 4-002-2713), δ^*-Al_2O_3 (PDF file 46-1215), $CeAl_{11}O_{18}$ (PDF file 00-048-0055)

Average particle sizes (APSs) and specific surface areas (SSAs) from BET

The APSs for these materials were estimated from Debye-Scherer line broadening and their SSAs (Table **3.1**). Both methods give very similar results. The average SSAs for the samples are 55 ± 10 m^2/g, giving APS values of 15 ± 5 nm.

Table 3.1. APSs and SSAs of $(CeO_2)_x(Al_2O_3)_{1-x}$ nanopowders

Sample Mole % Ceria	XRD line broadening Particle size (nm)	BET-derived Particle size (nm)	SSA (m^2/g)
95	20 ± 1	10 ± 1	45
75	18 ± 1	10 ± 1	45
50	16 ± 1	10 ± 1	50
30	15 ± 1	10 ± 1	57
15	15 ± 1	10 ± 1	60
10	14 ± 1	11 ± 1	57
7.5	17 ± 1	11 ± 1	63
6	15 ± 1	12 ± 1	61
5	14 ± 1	12 ± 1	60
3	14 ± 1	13 ± 1	56
2	14 ± 1	13 ± 1	58
1.5	16 ± 1	12 ± 1	62
1	15 ± 1	11 ± 1	65
0.5	14 ± 1	10 ± 1	70
0.1	12 ± 1	11 ± 1	66

Scanning electron microscopy (SEM) studies

SEM was used to demonstrate powder uniformity. Figure **3.3** shows that SEM resolution is insufficient to reveal individual particles but does provide a view of the general particle population. These SEMs indicate that the particle populations produced here do not include any obvious micron size particles.

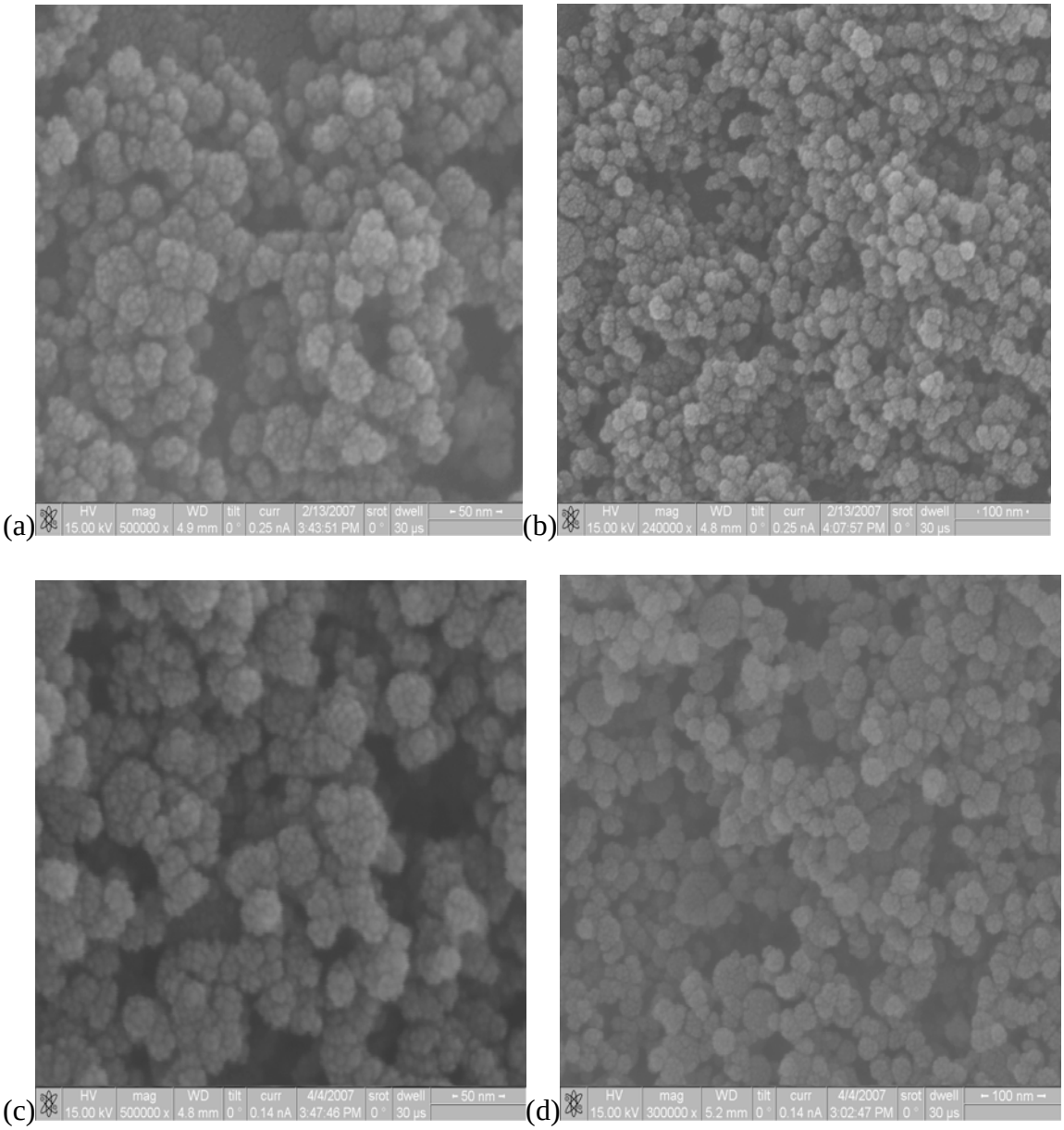

Figure 3.3. SEM images of (a) 75 mole% CeO_2 in Al_2O_3. (b) 50 mole% CeO_2 in Al_2O_3. (c) 10 mole% CeO_2 in Al_2O_3. (d) 0.5 mole% CeO_2 in Al_2O_3.

<u>High Resolution TEM (transmission electronic microscopy) studies</u>

TEM images were used to gather information on particle morphologies and sizes of as-prepared powders. Discussions of actual size/size distributions are not appropriate if based solely on TEM micrographs, unless combined with the XRD results and SEM images. Figure **3.4** offers high-resolution TEM images of $(CeO_x)_x(Al_2O_3)_{1-x}$ nanopowders

from LF-FSP. Particle sizes here are typically below 30 nm in diameter with the vast majority < 20 nm.

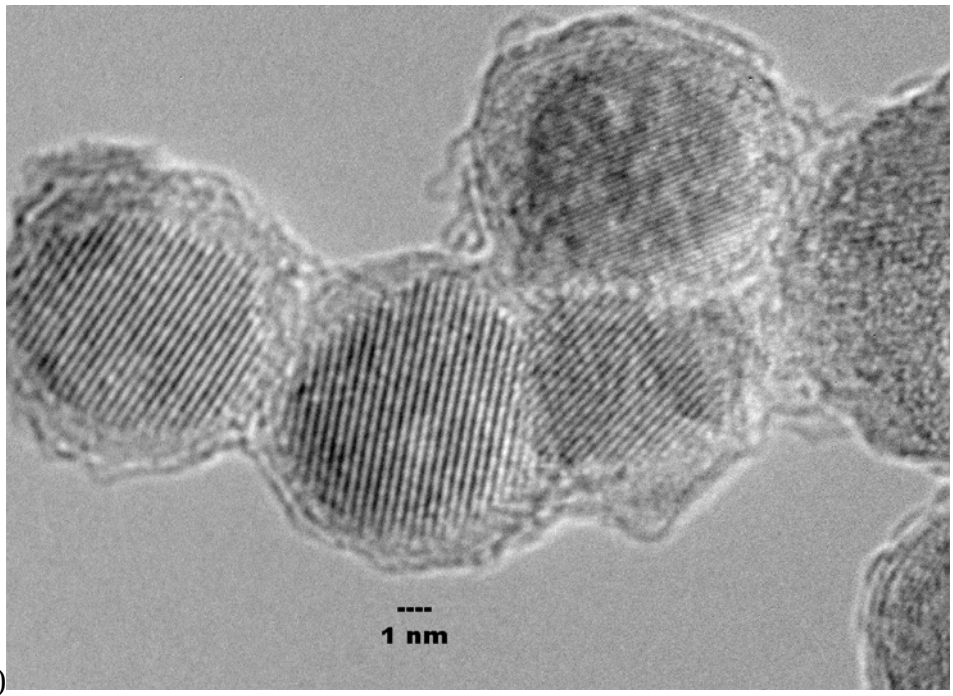

(a)

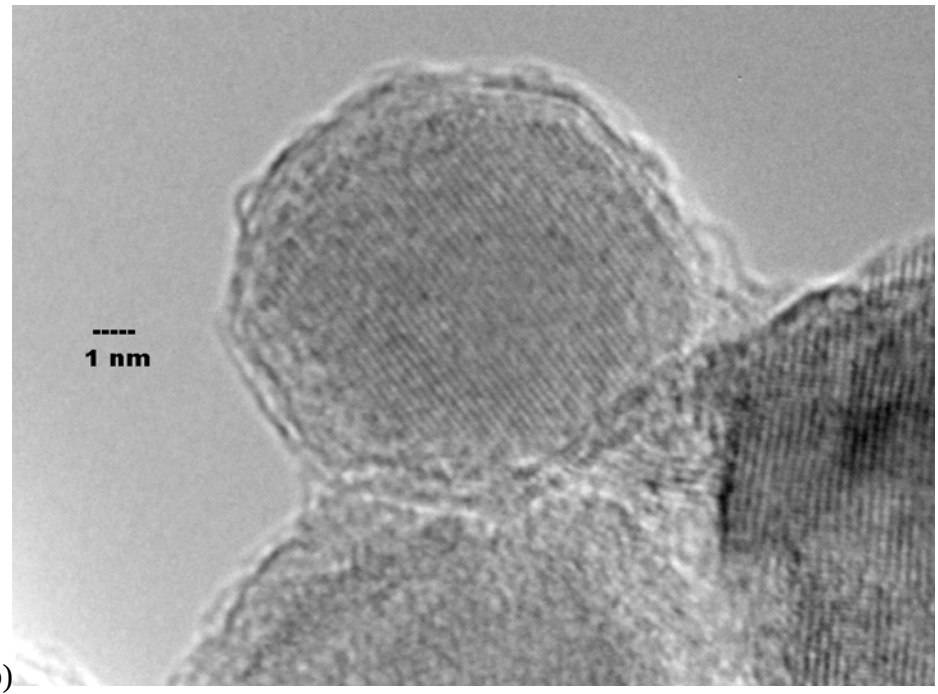

(b)

Figure 3.4. HR-TEM images of (a) 50 mole% CeO_2 in Al_2O_3
(b) 75 mole% CeO_2 in Al_2O_3.

In Figure **3.4**, clear lattice fringes in particle cores show a high degree of crystallinity of the CeO_x. Phase segregation between cubic ceria and δ*-alumina can be presumed from these core-shell TEM images. Since elements with high Z numbers are darker in HR TEM images, the ceria core and alumina shell can easily be distinguished. Although the particles appear to be highly necked (aggregated) they are easily dispersed through ultrasonication with dispersions staying stable for up to 72 h without sedimentation.

Particle Formation Mechanism

At the lowest concentrations of CeO_x (less than 10 mole%), Ce^{3+} ions are located in δ^*-alumina lattice or Ce-Magnetoplumbite ($CeAl_{11}O_{18}$) as discussed above.[39-41] At higher ceria concentrations (≥ 30 mole % ceria), CeO_x particles become encapsulated in Al_2O_3. We believe this is due to different nucleation and condensation processes.

During particle formation in the flame, species with lower vapor pressures can be expected to nucleate and grow earlier at faster rates than species with higher vapor pressures. Given that Al_2O_3 has a lower vaporization temperature (3000 ^oC) than CeO_2 (3906 ^oC),[42,43] it seems reasonable to suggest that during the LF-FSP process, CeO_x species will nucleate and condense first followed by Al_2O_3. This results in homogeneous core-shell nanostructured nanopowders.

Since LF-FSP processing enables rapid quenching in a single step, core-shell ceria-alumina mixed-metal oxide materials form at nano size level different from conventionally processed ceria-alumina binary materials. Note that we have recently reported similar results for LF-FSP produced $(ZrO_2)_x(Al_2O_3)_{1-x}$ nanopowders.[32]

STEM/XEDS

To determine where the cerium ions reside in as-produced powders, the Figure **3.5** STEM image was obtained for a $(CeO_x)_{0.5}(Al_2O_3)_{0.5}$ sample. The large Z contrast between the Ce and Al ions is demonstrated by the distinctly brighter high Z core and darker alumina shells [dark cores and bright shells in normal TEM (**Figure 3.4**)] as corroborated by the XEDS analyses (Figure **3.6**) for the shell (EDS-1) and core (EDS-2) regions.

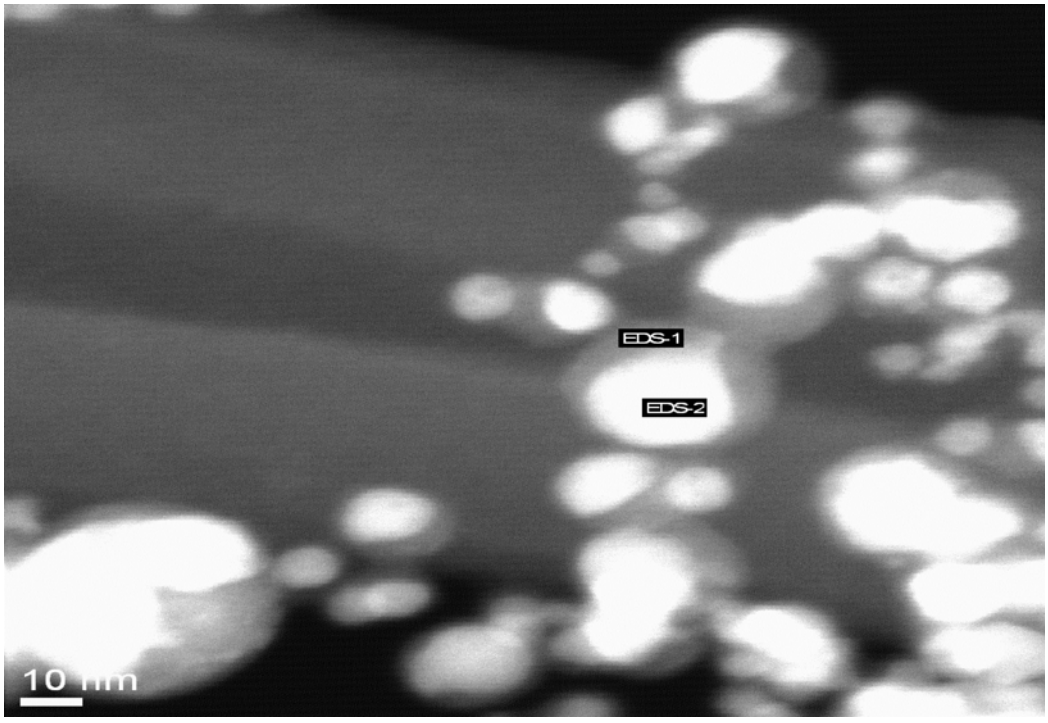

Figure 3.5. STEM image of core-shell $(CeO_2)_{0.5}(Al_2O_3)_{0.5}$

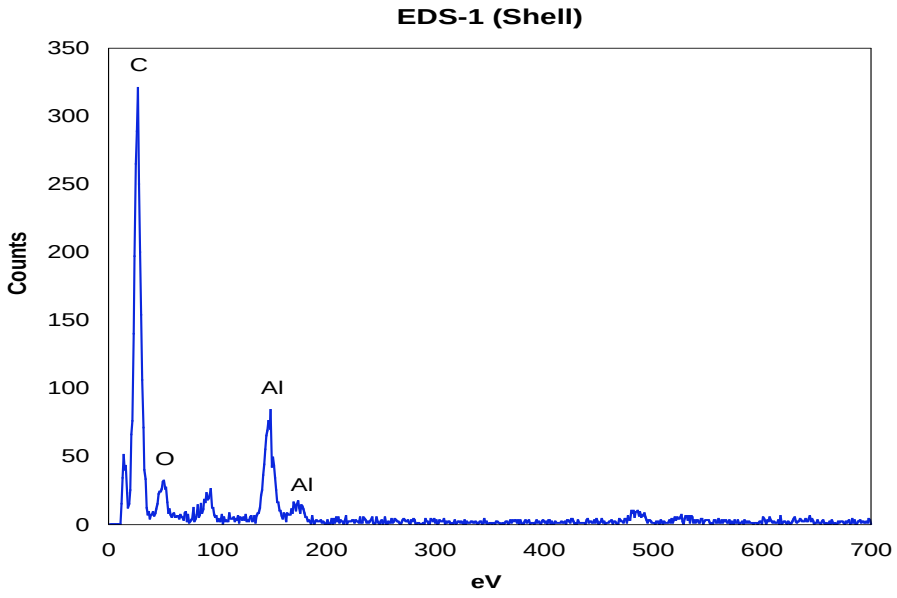

(a)

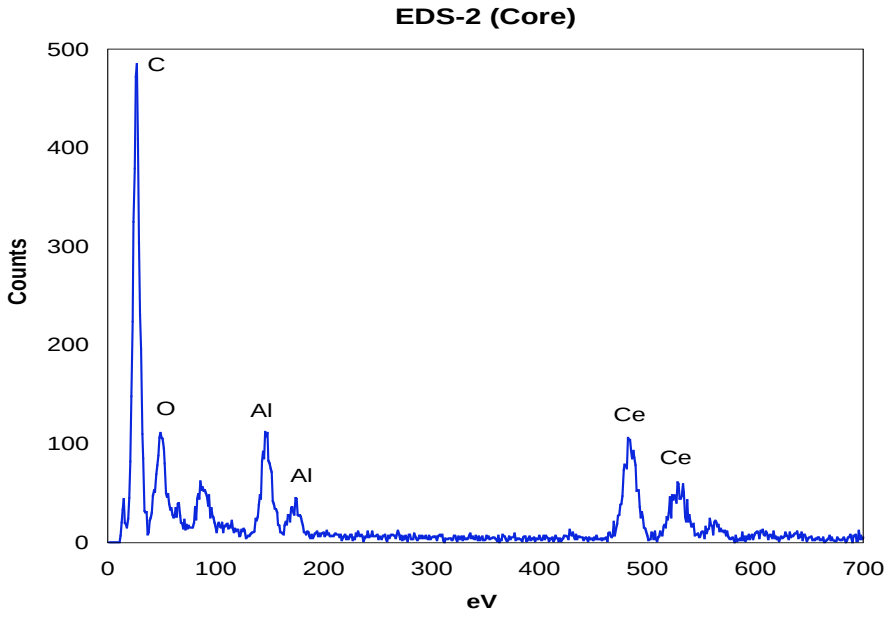

(b)

Figure 3.6. (a), (b) XEDS of core-shell $(CeO_2)_{0.5}(Al_2O_3)_{0.5}$

FTIR spectra

Once the particle morphologies were characterized by XRD and high-resolution microscopy, the particle surface chemistries were characterized using FTIR per Figure **3.7**. All of the materials exhibit weak νOH absorptions in the 3700-3000 cm^{-1} region, attributable to surface hydroxyls arising from both physi- and chemisorbed water.[44] No νCH bands in the 3000-2700 cm^{-1} region were observed on the nanopowder surfaces.

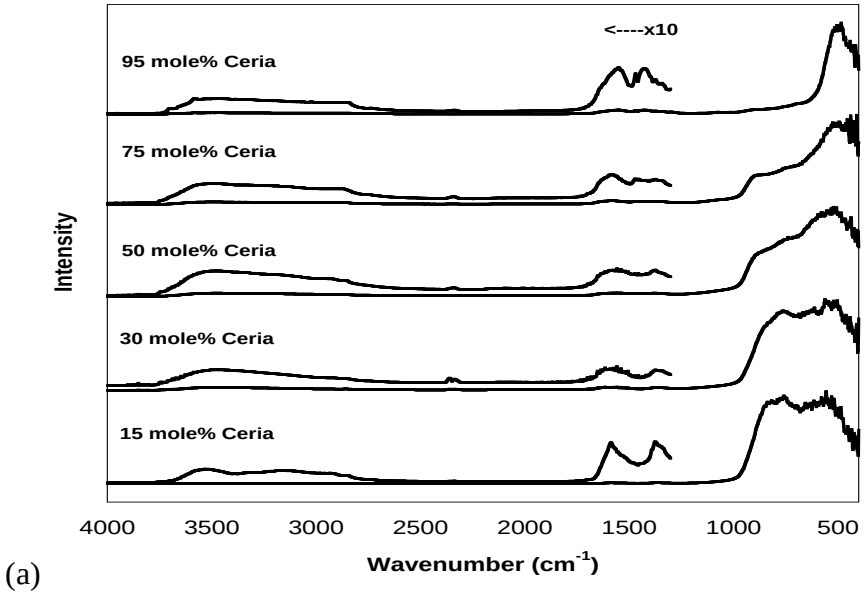

(a)

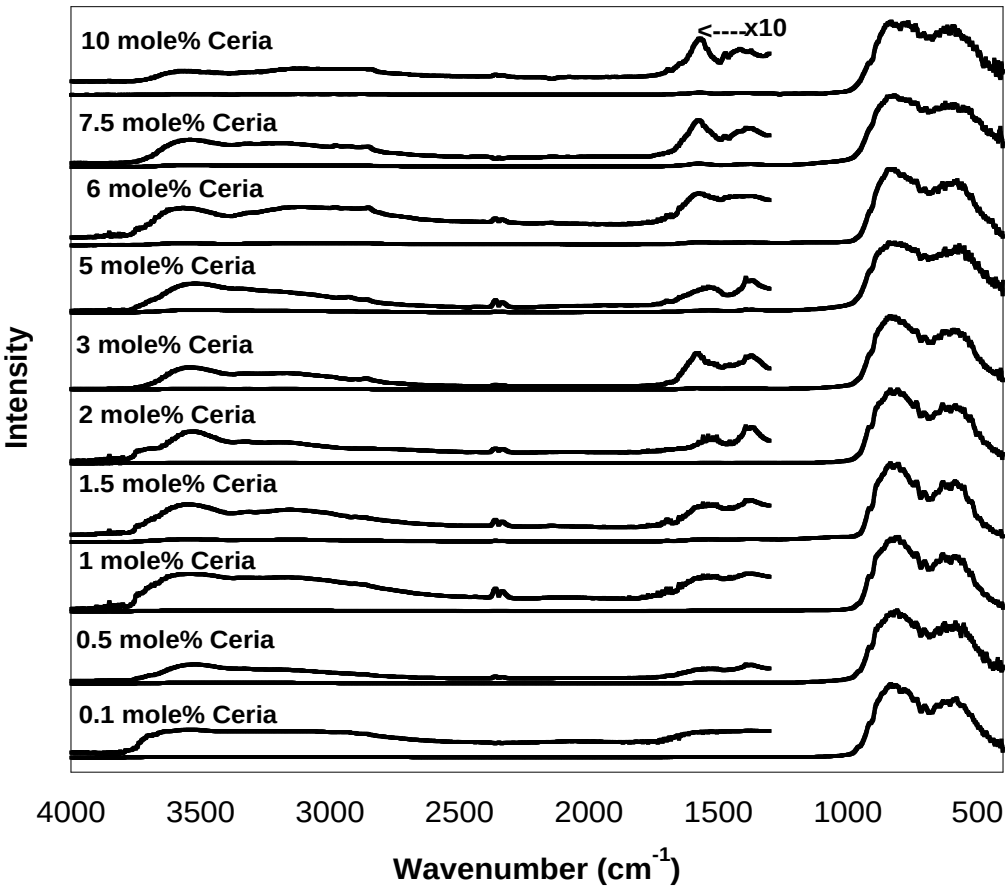

(b)

Figure 3.7. FTIR spectra of (a) ceria-rich (b) alumina-rich $(CeO_2)_x(Al_2O_3)_{1-x}$.

Peaks attributable to surface confined CO_2 (1450 cm^{-1}) and carbonates (1620 cm^{-1}) are observed in the 1800 to 1400 cm^{-1}region in accord with those seen by Liu *et. al.* and in our previous studies of pure δ-Al_2O_3 nanopowders.[28,45]

The lower wavenumber region shows νM-O bands typical for δ-alumina including two νAl-O bands at 810 cm^{-1} (stretching vibrations of tetrahedrally coordinated Al-O) and 610 cm^{-1} (octahedrally coordination).[46,47] Ceria has a well-defined νCe-O band at 458 cm^{-1}.[48,49]

TGA-DTA studies

Figure **3.8** records the mass loss events for the $(CeO_x)_x(Al_2O_3)_{1-x}$ composition nanopowders. All as-processed powders exhibit 1-1.5 wt% mass-losses up to ≈ 300°C typical of LF-FSP produced nanopowders, that can be attributed to evolution of both physi- and chemisorbed water as seen in the FTIR (Figure **3.7**).[44] Mass losses between 300° and 400 °C are due to elimination of carbonate species.

Perhaps the most interesting observations are those at higher temperatures that appear to be associated with mass gains in the TGA at ca. 1200°C with corresponding exotherms seen in the DTA (Figure **3.9**). The most reasonable explanation for these mass gains is oxidation of residual Ce^{3+}. The solubility of Ce^{3+} in δ-Al_2O_3 is ≤ 5 mole %. $Ce^{3+/4+}$ are essentially insoluble in α-alumina. [50-52] Thus, we presume that the Ce^{3+} ions present in the δ-Al_2O_3 lattice or as magnetoplumbite segregate out during the δ to α alumina transformation and oxidize to CeO_2.

In Table **3.2**, we estimate the possible maximum amounts of Ce^{3+} ions from the mass gains above the ceria solubility limit. The mass gain of each composition is assumed to be oxygen as Ce^{3+} ions oxidize to CeO_2.

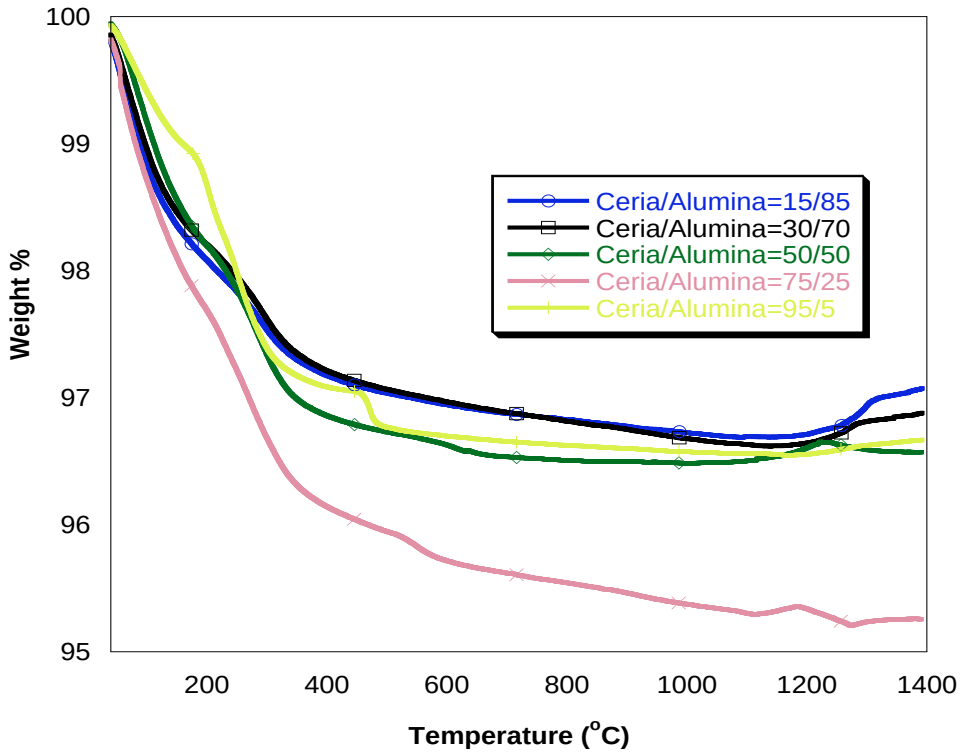

(a)

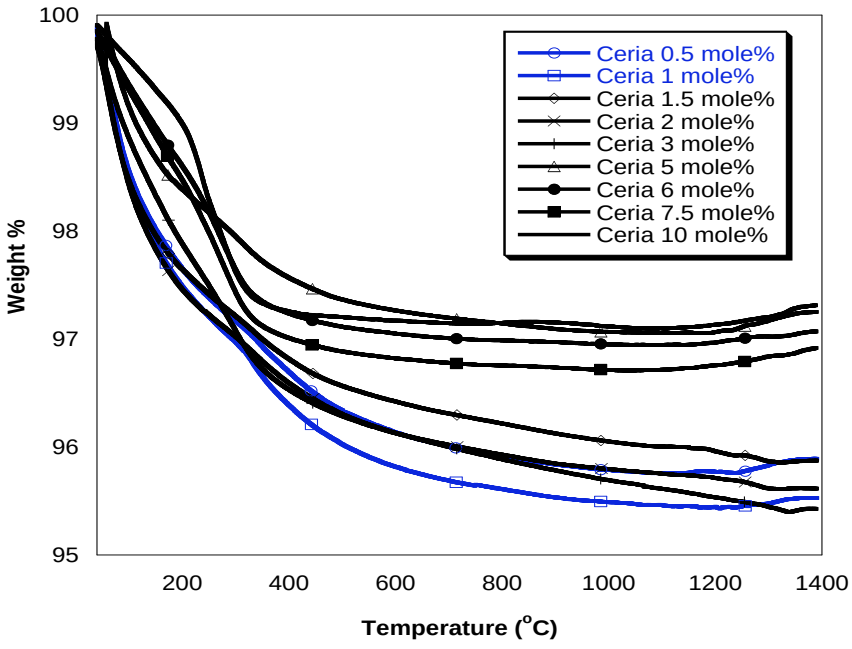

(b)

Figure 3.8. TGA of as-processed (a) ceria-rich (b) alumina-rich $(CeO_x)_x(Al_2O_3)_{1-x}$ ramped at 10°C/min/air.

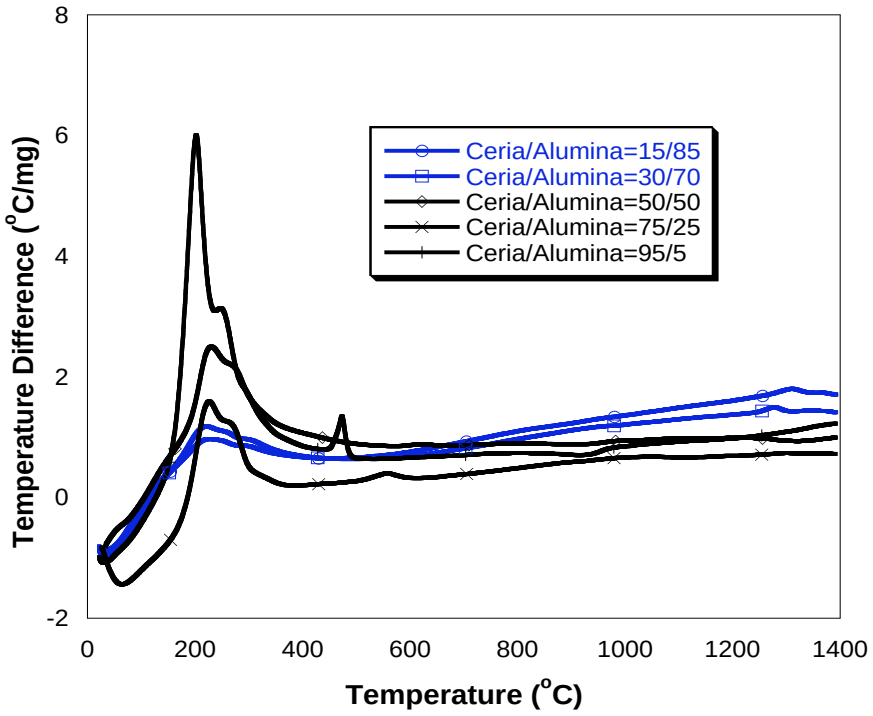

(a)

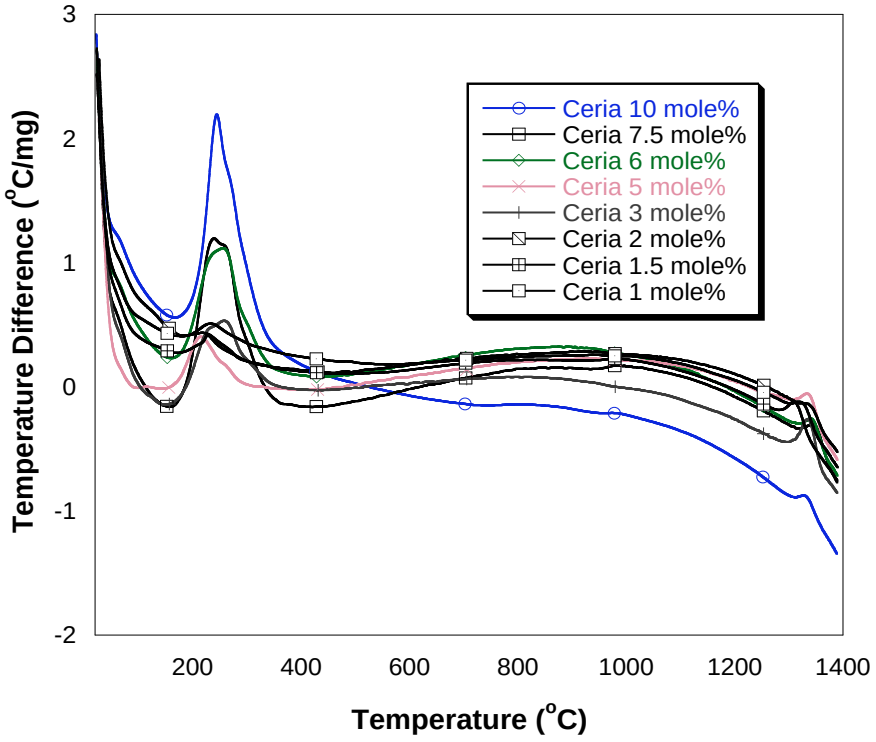

(b)

Figure 3.9. DTA as-processed of (a) ceria-rich (b) alumina-rich $(CeO_x)_x(Al_2O_3)_{1-x}$ ramped at 10°C/min/air.

Table 3.2. Possible maximum portions of dissolved Ce^{3+} ions in δ-alumina

Ceria mole %	Mass gain (wt%)	Possible maximum Ce^{3+}* (mol ± 0.1 %)
30	0.30	0.7
15	0.32	0.7
10	0.21	0.4
7.5	0.20	0.4
6	0.18	0.3
5	0.15	0.3

*Assumes all reduced species are Ce^{3+}

As with many of our previous studies, LF-FSP materials generated by rapid quenching lead to novel kinetic products not expected based on traditional processing methods that typically drive formation through thermodynamic assumption on particle mixtures. Since traditional processing methods lead to thermodynamically rather than kinetically defined phase compositions, these materials may offer unique opportunities for variety of applications.

From our previous study, Ce^{3+} in Al_2O_3 can also offer potential for photonic applications such as sensor, laser and display materials.[22-24]

3.5 Conclusions

LF-FSP provides access to $(CeO_x)_x(Al_2O_3)_{1-x}$ mixed-metal oxide nanopowders with exceptional control of stoichiometry and phase purity. We were able to produce nanopowders of any composition in the $(CeO_x)_x(Al_2O_3)_{1-x}$ phase field with specific surface area of ≥ 50 m^2/g at rates of 100-300 g/h. Most of all, we succeeded in preparing core-shell nanoparticles in the $(CeO_x)_x(Al_2O_3)_{1-x}$ system in a single step, at CeO_x rich compositions (≥ 15 mole%). We also found the presence of Ce^{3+} ions in δ-alumina lattice at all concentrations and Ce-magnetoplumbite at 5-10 mole % CeO_x concentrations.

Since LF-FSP offers rapid quenching of the combustion species, it provides access to new, kinetic materials not accessible by any other conventional processing method. Thus, we find the presence of Ce^{3+} ions in nanopowders of Ce-Al-O system, Ce-magnetoplumbite structure and $(CeO_x)_x(Al_2O_3)_{1-x}$ core-shell nanostructured nanoparticles at specific CeO_x compositions. These nanopowders can offer novel potential for catalytic, structural, photonic, and electronic applications.

3.6 References

1. H. W. Jen, G. W. Graham, W. Chun, R. W. McCabe, J. P. Cuif, S. Deutsch, O. Touret, "Characterization of model automotive exhaust catalysts: Pd on Ceria and Ceria-zirconia supports," *Cat. Today* **50** 309-28 (1999).

2. P. Marecot, L. Pirault, G. Mabilon, M. Prigent, J. Barbier, "Influence of the redox properties of ceria on the preparation of three-way automotive platinum-rhodium/alumina-ceria catalysts," *Appl. Catal. B,* **5** 57-69 (1994).

3. R. W. McCabe, J. M. Kisenyi, "Advances in automotive catalyst technology," *Chemistry & Industry* **15**, 605-608 (1995)

4. K. Zhang, H. Liu, Y. Wu, W. Hu, " Synthesis of (Y, Gd)$_3$Al$_5$O$_{12}$:Ce nanophosphor by co-precipitation method and its luminescence behavior," *J. Mater. Sci.* 42: 9200–9204 (2007)

5. N. Kalivas, I. Valais, D. Nikolopoulos, A. Konstantinidis, A. Gaitanis, D. Cavouras, C.D. Nomicos, G. Panayiotakis, I. Kandarakis, "Light emission efficiency and imaging properties of YAP:Ce granular phosphor screens," *Appl. Phys. A* 89, 443–449 (2007)

6. O. Milosevic, L. Mancic, M. E. Rabanal, J. M. Torralba, B. Yang, P. Townsend, "Structural and Luminescence Properties of Gd_2O_3:Eu^{3+} and $Y_3Al_5O_{12}$:Ce^{3+} Phosphor Particles Synthesized via Aerosol," *J. Electrochem. Soc.* **152** 9 G707-G713 (2005)

7. S. Hedge, S. V. Babu, " Study of surface charge effect on oxide and nitride planarization using alumina/ceria mixed abrasive slurries," *Electrochemical and solid state Letters* **7** (12) G316-G318 (2004)

8. G. Lim, J. Lee, J. Kim, H. Lee, S. Hyun, "Mechanochemical synthesis of nano-sized CeO_2 and its application for CMP slurry," *Mater. Sci. Forum* Vols. 449-452 pp. 1105-1108 (2004)

9. A. S. Kumar, A. R. Durai, T. Sornakumar, "Performance characteristics of ceria toughened alumina ceramic cutting tool on machining C30 steel," *Powder Metallurgy* Vol. 47 No.3 235-238 (2004)

10. B. Huang, X. F. Ye, S. R. Wang, H. W. Nie, R. Z. Liu, T. L. Wen, "Performance of Ni/ScSZ cermet anode modified by coating with $Gd_{0.2}Ce_{0.8}O_2$ for a SOFC," *Mater. Res. Bull.* **42** 1705–1714 (2007)

11. N. Laosiripojana, S. Assabumrungrat, "Catalytic steam reforming of dimethyl ether (DME) over high surface area Ce–ZrO_2 at SOFC temperature: The possible use of DME in indirect internal reforming operation (IIR-SOFC)," *App. Cat. A: General* **320** 105–113 (2007)

12. M. Soorie, S. J. Skinner, "Ce substituted Nd_2CuO_4 as a possible fuel cell cathode

material," *Solid State Ionics* **177** 2081–2086 (2006)

13. A. Piras, A. Trovarelli, G. Dolcetti, "Remarkable stabilization of transition alumina operated by ceria under reducing and redox conditions," *Appl. Catal. B*, **28**, L77-L81 (2000)

14. A. F. Ahlstrom-Silversand, C. U. I. Odenbrand, "Combustion of methane over a Pd-Al_2O_3/SiO_2 catalyst activity and stability," *Appl. Catal.* **153**, 157-175 (1997)

15. H. Arai, M. Machida, "Thermal stabilization of catalyst supports and their application to high temperature catalytic combustion," *Appl. Catal. A*, **138**(2) 161-176 (1996)

16. J. S. Church, N.W. Cant, D. L. Trimm, "Stabilisation of aluminas by rare earth and alkaline earth ions," *Appl. Catal. A.* **101** 105-116 (1993)

17. D. J. Pettigrew, D. L. Trimm, N. W. Cant, "The effects of rare-earth-oxides on the reverse water-gas shift reaction on palladium alumina," *Catal. Lett.* **28** 313-319 (1994)

18. J. Chang, T. Chou, " Selective hydrogenation of isoprene over δ-alumina-supported eggshell Pd catalysts: Particle size effects," *Appl. Catal.A* **156** 193-205(1997)

19. a. R.M. Laine, S. C. Rand, T. R. Hinklin, G. R. Williams, " Ultrafine powders and their use as lasing media," *U.S.Patent* 6,656,588 Decenber 2, 2003. b. Hinklin T.R.; Ph.D. dissertation, Mixed-metal Oxide Nanopowders for Structural and Photonic Applications, 2006, University of Michigan.

20. B. Li, G. R. Williams, S. C. Rand, T. R. Hinklin, R. M. Laine, "Continuous–wave ultraviolet laser action in strongly scattering Nd-doped alumina," *Opt. Lett.* **27**(6) 394-396 (2002)

21. G. R. Williams, S. B. Bayram, S. C. Rand, T. R. Hinklin, R. M. Laine, "Laser action in strongly scattering rare-earth-metal-doped dielectric nanophosphors," *Phys. Rev. A* **65** 013807 (2001)

22. C. Chiang, M. Tsai, M. Hon, "Preparation of cerium-activated GAG phosphor powders influence of Co-doping on crystallinity and luminescent properties," *J. Electrochem. Soc.* **154**(**10)** J326-J329 (2007)

23. J. Touš, K. Blažek, L. Pína, B. Sopko, "High-resolution X-ray imaging CCD camera based on a thin scintillator screen," *Radia. Meas.* **42** 925 – 928 (2007)

24. J. Yuan, J. Wang, D. Xiong, J. Zhao, Y. Fu, G. Zhang, C. Shi, "Potential PDP phosphors with strong absorption around 172 nm: Rare earth doped $NaLaP_2O_7$ and $NaGdP_2O_7$," *J. Lumin.* **126** 717-722 (2007)

25. J. Marchal, T. Johns, R. Baranwal, T. Hinklin, R. M. Laine, "Yttrium aluminum garnet nanopowders produced by liquid-feed flame spray pyrolysis (LF-FSP) of metalloorganic precursors," *Chem. Mater*. **16**, 822-831 (2004).

26. C. R. Bickmore, K. F. Waldner, R. Baranwal, T. Hinklin, D. R. Treadwell, R. M. Laine, "Ultrafine titania by flame spray pyrolysis of a titanatrane complex: Part I," *J. Europ. Ceram. Soc.* **18**, 287-97 (1998).

27. R. M. Laine, T. R. Hinklin, G. R. Williams, S. C. Rand, "Low-cost nanopowders for phosphor and laser applications by flame spray pyrolysis," *Mat. Sci. Forum* vol. 343-346 p.500-510 (2000)

28. T. Hinklin, B. Toury, C. Gervais, F. Babonneau, J. J. Gislason, R. W. Morton, R. M. Laine, "Liquid-feed flame spray pyrolysis of metalloorganic and inorganic alumina sources in the production of nanoalumina powders," *Chem. Mater*. **16**, 21-30 (2004).

29. S. Kim, J. J. Gislason, R.W. Morton, X. Q. Pan, H. P. Sun, R. M. Laine, "Liquid-feed flame spray pyrolysis of nanopowders in the alumina-titania System," *Chem. Mater*. **16**, 2336-2343 (2004).

30. J. A. Azurdia, J. Marchal, P. Shea, H. Sun, X. Q. Pan, R. M. Laine, " Liquid-feed flame spray pyrolysis as a method of producing mixed-metal oxide nanopowders of potential interest as catalytic materials. Nanopowders along the NiO-Al_2O_3 tie line including $(NiO)_{0.22}(Al_2O_3)_{0.78}$, a new inverse spinel composition," *Chem. Mater.* **18** (2006) 731-739

31. J. A. Azurdia, J. Marchal, R. M. Laine, " Synthesis and characterization of mixed-metal oxide nanopowders along the CoO_x–Al_2O_3 tie line using liquid-feed flame spray pyrolysis," *J. Am. Ceram. Soc.*, 89 [9] 2749–2756 (2006)

32. M. Kim. R. M. Laine, "Liquid-feed flame spray pyrolysis (LF-FSP) for combinatorial processing of nanooxide powders along the $(ZrO_2)_{1-x}(Al_2O_3)_x$ tie-line. Phase segregation and the formation of core-shell nanoparticles," *J. Cer. Proc. Res. **8** 129-136* (2007).

33. T. Hinklin, B. L. Mueller, R. M. Laine, U.S. Patent 5,418,298, 1995

34. R. Narayanan, R. M. Laine, "Synthesis and characterization of precursors for group II metal aluminates," *App. Org. Chem.* **11** (1997) 919-927

35. Y. Jia, Y. Hotta, K. Sato, K. Watari, "Homogeneous ZrO_2-Al_2O_3 composite prepared by nano-ZrO_2 particle multilayer-coated Al_2O_3 particles," *J. Am. Ceram. Soc*. **89[3]** (2006) 1103-1106

36. S. Chang, L. Liu, S. Asher, "Preparation and properties of tailored morphology, monodisperse colloidal silica-cadmium sulfide nanocomposites," *J. Am. Chem. Soc*.

116 (1994) 6739-6744

37. A. J. Ruys, Y. Mai, "The nanoparticle-coating process: a potential sol-gel route to homogeneous nanocomposites," *Mater. Sci. Eng*. **A265** (1999) 202-207

38. J. D. Ferguson, K. J. Buechler, A. W. Weimer, S. M. George, " SnO_2 atomic layer deposition on ZrO_2 and Al nanoparticles: Pathway to enhanced thermite materials," *Powder Technology* **156** (2005) 154-163

39. N. Iyi, S. Takekawa, S. Kimura, "Crystal chemistry of hexaaluminates: β-Alumina and magnetoplumbite structures," *J. Solid State Chem.* **83**, 8-19 (1989)

40. S. R. Jansen, J. W. de Haan, L. J. M van de Ven, R. Hanssen, H. T. Hintzen, and R. Metselaar, "Incorporation of nitrogen in alkaline-earth hexaaluminates with a β-alumina- or a magnetoplumbite-type structure," *Chem. Mater.* **9** 1516-1523 (1997)

41. K. Okada, A. Hattori, T. Taniguchi, A. Nukui, R. N. Das, "Effect of divalent cation additives on the γ-Al_2O_3-to-α-Al_2O_3 phase transition," *J. Am. Ceram. Soc*., **83** [4] 928–932 (2000)

42. R. Jossen, S. E. Pratsinis, W. J. Stark, and L. Madler, "Criteria for flame-spray synthesis of hollow, shell-like, or inhomogeneous oxides," *J. Am. Ceram. Soc*. **88** [6] (2005) 1388-1393

43. CRC handbook of chemistry and physics. 80th ed.1999-2000. CRC press

44. J. B. Peri, "Infrared and gravimetric study of the structure hydration of γ-alumina," *J. Phys. Chem*. **69** 211-219 (1965)

45. X. Liu, R. E. Truitt, "DRFT-IR Studies of the Surface of γ-Alumina," *J. Am. Chem. Soc.* **119** 9856-9860 (1997)

46. J. M. Saniger, "Al-O infrared vibrational frequencies of γ-alumina," *Mater. Lett*. **1995**, 22, 109-113

47. P. Tarte, "Infrared spectra of inorganic aluminates and characteristic vibrational frequencies of AlO_4 tetrahedra and AlO_6 octahedra," *Spectrochim. Acta* **1967**, 23A, 2127-2143

48. A. Bouchara, L. Rozes,, G.J. DE A.A. Soler-Illia, C. Sanchez, "Use of functional dendritic macromolecules for the design of metal oxo based hybrid materials," *J. Sol-Gel Sci. Tech.* **26** 629–633 (2003)

49. P. G. Harrison, W. Daniell "Catalytic activity, surface redox properties, and structural evolution during the thermal processing of chromium-promoted ceria oxidation catalysts" *Chem. Mater.* **13** 1708-1719 (2001)

50. E. W. Dewing, G. M. Haarberg, S. Rolseth, L. Ronne, J. Thonstad, N. Aalberg, “The chemistry of solutions of CeO_2 in cryolite melts,” *Metal. Mater. Trans. B* **26B** 81-86 (1995)

51. A.S. Prakash, C. Shivakumara, M.S. Hegde, “Single step preparation of $CeO_2/CeAlO_3/\gamma$ -Al_2O_3 by solution combustion method: Phase evolution, thermal stability and surface modification,” *Mat. Sci. Eng. B* **139** 55-61 (2007)

52. R. Sasikala, V. Sudarsan, S.K. Kulshreshtha, “^{27}Al NMRstudies of Ce–Al mixed oxides: origin of 40 ppm peak,” *J. Solid State Chem.* **169** 113-117 (2002)

CHAPTER 4

ONE STEP SYNTHESIS OF $Ce_xZr_{1-x}O_2$ AND $(Ce_{0.7}Zr_{0.3}O_2)_x(Al_2O_3)_{1-x}$ NANOPOWDERS

4.1 Abstract

We report here the synthesis of $Ce_xZr_{1-x}O_2$ and $(Ce_{0.7}Zr_{0.3}O_2)_x(Al_2O_3)_{1-x}$ high surface area nanopowders in a single step by liquid-feed flame spray pyrolysis (LF-FSP) of metalloorganic precursors including $Ce(O_2CCH_2CH_3)_3(OH)$, $Zr(O_2CCH_2CH_3)_2(OH)_2$, and alumatrane $[N(CH_2CH_2O)_3Al]$. Mixtures of all precursor systems in ethanol with the ceramic yields of 2.5 wt% were aerosolized with O_2, combusted at temperature above 1500 ^oC, and rapidly quenched at 1000 ^oC/msec to form $Ce_xZr_{1-x}O_2$ and $(Ce_{0.7}Zr_{0.3}O_2)_x(Al_2O_3)_{1-x}$ nanopowders of selected compositions, at rates of 100 g/h. The resulting, as-processed materials from LF-FSP are un-agglomerated nano-sized powders with average particle sizes (APSs) < 20 nm and corresponding surface areas of 30 ~ 50 m^2/g. Characterization of as-processed nanopowders were performed in terms of phase, particle size, specific surface area, compositions, and morphology by XRD, BET, SEM, TEM, TGA-DTA, and FT-IR.

We are able to produce binary $Ce_xZr_{1-x}O_2$ and ternary $(Ce_{0.7}Zr_{0.3}O_2)_x(Al_2O_3)_{1-x}$ nanopowders in one step by LF-FSP. Cubic $Ce_{0.7}Zr_{0.3}O_2$ solid solutions form during LF-FSP processing. Surprisingly, LF-FSP with the correct choice of metalloorganic precursors provides access to core-shell nanopowders in a single step for $(Ce_{0.7}Zr_{0.3}O_2)_x(Al_2O_3)_{1-x}$ (x=0.5, 0.7) by differences in condensation and nucleation between alumina and $Ce_{1-x}Zr_xO_2$ during FSP processing. These as-produced materials are without microporosity at surface areas of ≥ 30 m^2/g. Evidence is presented suggesting the incorporation of $(Ce_{0.7}Zr_{0.3})^{3+}$ species in δ-alumina for as-processed $(Ce_{0.7}Zr_{0.3}O_2)_x(Al_2O_3)_{1-x}$ nanopowders.

4.2 Introduction

Worldwide concerns for air quality, especially in urban environs, provide continuing impetus for developing increasingly efficient emission control systems for internal combustion engines. Three recent reviews describe the progress, current problems and future needs (legal mandates) that drive efforts to develop better systems.[1-3] These reviews note that for autos, three way catalyst (TWC) systems composed of an active metal (e.g. Pd) impregnated on a reversible oxygen storage promoter ($Ce_xZr_{1-x}O_2$)/high surface area alumina washcoat are the industry standard. These systems effectively convert CO, NO_x, and hydrocarbons, the main pollutants in auto exhaust, to CO_2, N_2, O_2, and H_2O. They are now so effective that contributions from the once lower emitting and unregulated diesel engines now constitute a significant component of urban air pollution. TWCs that are effective for autos offer little or no help in eliminating the particulate, unburned hydrocarbon and particularly NO_x emissions produced by diesel engines because of the 5-15 mol % excess O_2 in their exhausts. Similar problems occur with the more fuel efficient lean-burn gasoline engines currently being introduced.[4,5]

Reduction of particulate and hydrocarbon emissions from diesels is difficult but not impossible using existing technology.[6,7] However, coincident NO_x reduction requires new scientific and technical advances. New U.S. regulations require that diesel engine NO_x emissions be cut to 4g/BHP-hr in '98 and to 2.0 gr./BHP-hr by 2003. Similar requirements apply to Europe and somewhat less stringent requirements are in place in Japan and Korea. This represents an average decrease of 50% or greater in NO_x tailpipe emissions from pre-'98 standards.

Current problems still of concern for TWCs are deactivation of the catalyst due to loss of catalytic surface area and contamination of noble metal catalyst which results in incomplete conversion of the exhaust gases.[7,8] For diesel engines, carbon particulate products clog and coat the surface of catalytic converter, prohibiting its functioning. While current TWCs are very effective for reduction and oxidation simultaneously converting HC, CO and (NO_x) to harmless gases, they are not effective as oxidizing catalysts to convert carbon soot in diesel exhausts to carbon dioxide.[9-11] Moreover, the oxidizing environment in lean-burn exhaust systems makes NO_x reduction difficult, and

causes deactivation of noble metal catalysts (Pd, Pt, Rh) in standard TWC systems by oxidation.[12,13]

Standard TWCs are combinations of honeycomb type supports to which a "washcoat" material including the active catalyst is added. The washcoat is composed of noble metals deposited on oxygen storage materials, typically CeO_2/ZrO_2 with alumina as the support, providing oxygen for oxidation of HCs and noble metals (Pt, Rh, Pd) that effect the simultaneous catalytic reactions. A stable, high surface area support is an essential requirement for all catalyst systems, and the minimization of sinterable porosity is also critical to stabilizing the high surface areas needed to maintain good catalytic activity with aging.

Essentially all catalyst systems used for all the forms of emission control cited above, e.g. the washcoat layer, are made by multistep processes.[7,8,14-24] For TWCs, this process can begin with solution precipitation of a $Ce_xZr_{1-x}O_2$ precursor followed by removal of the aqueous phase. The precursor is first calcined, then heated to crystallize the correct phase. The resulting materials are combined with an alumina precursor coating on a monolith and then heated to form a high surface area (70-150 m^2/g) washcoat that is then preaged to reduce microporosity (surface areas drop to <15 m^2/g).[7,8,14-24] This material is then solution impregnated with a noble metal catalyst and calcined again. The procedures including multiple time and equipment intensive steps make the whole process inefficient in terms of the cost and the quality of the final products.

We have developed an efficient approach to generating high surface area, micropore free nanopowders for potential catalytic applications using liquid-feed flame spray pyrolysis (LF-FSP). LF-FSP offers one step processing of a wide variety of mixed-metal oxide nanopowders such as Y_2O_3-Al_2O_3, CeO_2-Al_2O_3, ZrO_2-Al_2O_3, TiO_2-Al_2O_3, CoO-Al_2O_3 and NiO-Al_2O_3.[25-31] As-produced LF-FSP nanopowders are typically unaggregated with specific surface areas (SSAs) of 30-50 m^2/g and average particle sizes (APSs) of 15-30 nm.

Here we illustrate our approach to one step production of $Ce_xZr_{1-x}O_2$ solid solutions of essentially any composition and the formation of $Ce_{0.7}Zr_{0.3}O_2$ solid solution single crystals encapsulated in δ-alumina nanoparticles as $(Ce_{0.7}Zr_{0.3}O_2)_x(Al_2O_3)_{1-x}$ (x=0.3-0.9) mixed-metal oxide materials like those currently used for TWCs.[14-24]

The resulting $(Ce_{0.7}Zr_{0.3}O_2)_x(Al_2O_3)_{1-x}$ nanopowders produced by LF-FSP are unaggregated and therefore disperse easily. So we expect that these nanopowders in turn offer potential access to dense ceramic materials for catalytic, structural, and photonic applications.

4.3 Experimental

Materials

Cerium carbonate [$Ce_2(CO_3)3{\cdot}x(H_20)$, 99%] and zirconium carbonate [$2ZrO_2(CO_2){\cdot}x(H_2O)$, 99%] were purchased from PIDC Inc.(Ann Arbor, MI). EtOH (99 %) was purchased from standard sources and used as received. Alumatrane [$N(CH_2CH_2O)_3Al$] was prepared as described elsewhere.[32] Propionic acid ($C_2H_5CO_2H$, 99%) was purchased from Aldrich and used as received.

Precursor preparation.

A series of precursors corresponding to the ceramic compositions $[(CeO_2)_{0.7}(ZrO_2)_{0.3}]_x(Al_2O_3)_{1-x}$ (x = 0.9, 0.7, 0.5 and 0.3) was prepared from mixtures of metallorganic precursors as described below.

Al_2O_3 precursor

In all cases, alumatrane [$N(CH_2CH_2O)_3Al$] was used as the Al_2O_3 source. An alumatrane/ethanol solution was prepared containing 10.8 wt% Al_2O_3 as determined by TGA .

Cerium propionate precursor: $Ce(O_2CCH_2CH_3)_3(OH)$

Cerium carbonate [$Ce_2(CO_3)_3{\cdot}x(H_2O)$, 99%, 70 g, 0.15 mole] was reacted with excess propionic acid (400 mL, 5.44 mole) in a 1 L flask equipped with a still head and an addition funnel. N_2 was sparged directly through the solution (2 psi pressure) as the solution was heated at 120 ˚C/2h to distill off ~150 mL of liquid (water and propionic acid). The ceramic loading of the resulting precursor was 9 wt% as determined by TGA.

Zirconium propionate precursor: $Zr(O_2CCH_2CH_3)_2(OH)_2$

Zirconium carbonate [$2ZrO_2(CO_2){\cdot}x(H_2O)$, 99%, 150 g, 0.34 mole] was reacted with excess proprionic acid (500 ml, 6.80 mole) in a 1 l flask equipped with a still head and an addition funnel. N_2 was sparged directly through the solution (2 psi pressure) as the solution was heated at 120 °C/2h with magnetic stirring to distill off ~150 ml of liquid (water and propionic acid). The ceramic loading of the resulting precursor was 11 wt% as determined by TGA.

XRD studies

As-prepared samples were characterized using a Rigaku Rotating Anode Goniometer. Powder samples were prepared by placing ≈ 100 mg in XRD sample holders

(amorphous silica slides) for data collection. CuKα (λ = 1.54 Å) radiation with a Ni filter was used with a working voltage and current of 40 kV and 100 mA, respectively. Scans were continuous from 5–90° 2θ with a step scan of 2° 2θ/min in increments of 0.05° 2θ. Peak positions and relative intensities were characterized by comparison with PDF files of standard materials: CeO_2 (PDF file 43-1002), ZrO_2 (PDF file 42-1164), δ-Al_2O_3 (PDF file 46-1131) Debye-Scherer line broadening was used to calculate average particle sizes from the XRD powder patterns.

Thermal Gravimetric Analysis and Differential Thermal Analysis (TGA/DTA)

TGA-DTA was performed using a SDT 2960 Simultaneous Differential Thermal Analyzer (TA Instruments, Inc., New Castle, DE). The instrument was calibrated with gold supplied by Perkin-Elmer. Samples (70 mg) of as-prepared powders were hand pressed in a 3 mm dual action die and placed inside Pt sample cups and heated at ramp rates of 10˚C/min from ambient temperature to 1400˚C. The reference material was a pellet of α-alumina. A flow of synthetic air, 50 ml/min, was maintained during all experiments.

Specific surface area (SSA)

SSA was measured on a Micromeritics ASAP 2000 sorption analyzer. Samples (200 mg) were degassed at 400°C until the outgas rate was 5 mmHg/min. Analyses was run at 77K with N_2. SSAs were determined by the BET multipoint method using at least five data points with relative pressures of 0.001-0.20. The average particle size was derived using the formula $< R >= \frac{3}{\rho \times SSA}$ where <R> = average particle size, and ρ is the density of the material.

Scanning electron microscopy (SEM)

A field emission gun SEM (Phillips FEG XL30 SEM) was used to image powder morphologies. Powder samples were dispersed in distilled H_2O using an ultrasonic horn (Vibra-cell, Sonics and Materials, Inc., Newton, CT). A drop of the dispersed powder/water was placed on an aluminum SEM stub and allowed to dry for 4 h on a hot plate. Powders were sputter coated with 10-40 nm of Au-Pd to reduce charging effects. Operating voltage was between 10.0 and 20.0 kV.

Transmission Electron Microscopy (TEM)

An analytical high resolution TEM (Model 3011, JOEL, Osaka, Japan) was used to measure the particle sizes and morphologies of as-prepared powders. Powder samples were prepared by dipping a holey carbon grid in a vial of emulsion with as-prepared powder. The specimen was held in a Gatan double tilt goniometer. An operating voltage of 300 kV was used.

FTIR Spectra.

Diffuse reflectance Fourier transform (DRIFT) spectra were recorded on a Mattson Galaxy Series FTIR 3000 spectrometer (Mattson Instruments, Inc., Madison, WI). Optical grade, random cuttings of KBr (International Crystal Laboratories, Garfield, NJ) were ground, with 1.0 wt % of the sample to be analyzed. For DRIFT analysis, samples were packed firmly and leveled off at the upper edge to provide a smooth surface. For transmission IR, 100 mg of each sample prepared for DRIFT analysis was pressed in a stainless steel double action die (12.75 mm diameter) at 100 MPa for 1 min in a Carver Laboratory Press (model 3912). Fresh backgrounds of pure KBr were done every 2 hours. The FTIR sample chamber was flushed continuously with N_2 prior to data acquisition in the range 4000-400 cm^{-1}. Each runs consisted of 128 scans with a resolution of $\pm$ 8 cm^{-1}.

Liquid Feed - Flame Spray Pyrolysis (LF-FSP).

The apparatus used for LF-FSP are comprised of an aerosol generator, a combustion chamber, and an electrostatic powder collection system described elsewhere.[25-31] The precursor solution was pumped through the aerosol generator at a rate controlled by the ceramic yield of the solution. Typically, more concentrated (5 wt% ceramic yield) solutions were pumped at 100 mL/min to avoid producing large particles (200 – 1000 nm).[25-31] Solutions with lower ceramic yields were pumped at 400 Ml/min. Here we used the precursor solution with 2.5 wt% ceramic yield of each batches at the pumping rate of 300 Ml/min. The solution was atomized with oxygen to from an aerosol and ignited by two methane/oxygen torches, while the pressure was kept at 20 psi. Combustion produces temperatures > 1500 °C[28-30] and nano-sized oxide powders are collected in electrostatic precipitators (ESP).

4.4 Results and Discussion

The objective of the current study is to produce high surface area, non-porous $Ce_{1-x}Zr_xO_2/Al_2O_3$ materials in one step using LF-FSP as a prelude to exploring their potential utility for catalytic applications such as two/three-way catalysts (TWC)[14-24] and exhaust catalysts for diesel engines, etc.[9-13]

The LF-FSP process, which has been described in detail elsewhere,[25-31] aerosolizes solutions of single and mixed-metal alkoxides and/or carboxylates dissolved in alcohol (typically EtOH) using oxygen. The aerosol is ignited in a quartz combustion chamber generating flame temperatures of 1500°-2000°C depending on the processing conditions, the precursor and the alcohol used. The temperature drops rapidly to less than 400°C in ≈ 1 meter leading to very rapid quenching of the gas entrained ceramic "soot." This soot is then collected in electrostatic precipitators downstream from the combustion chamber. This soot consists of unagglomerated nanopowders of the exact composition as found in the original solution. Typical production rates are 50-100 g/h depending on the precursor. The resulting average particle sizes are 10-150 nm depending on processing conditions giving specific surface areas (SSAs) of 20-100 m^2/g. They are most frequently unagglomerated, single crystal particles that disperse readily in common solvents.

We have recently used LF-FSP to produce a wide variety of binary mixed-metal oxides nanopowders[25-32] along the $(MO_z)_{1-x}(Al_2O_3)_x$ tielines were M = Ni, Ti, Co, Mg, Y, Cu, Zr and Ce. The as-produced nanopowders are typically unaggregated with specific surface areas (SSAs) of 30-50 m^2/g and average particle sizes (APSs) of 15-30 nm.

Of particular importance is the fact that the quality of the nanopowders produced depends strongly on the type of metalloorganic precursor used. In our studies on the LF-FSP synthesis of δ-Al_2O_3, we determined that metal nitrates although relatively inexpensive are actually very poor precursors for LF-FSP processing because they tend to form large (200-2000 nm) hollow particles, whereas alumatrane $N(CH_2CH_2O)_3Al$ provides access to powders with SSAs ≈ 60 m^2/g.[25] Furthermore, combustion flame temperatures typically have no influence on the quality of the nanopowders produced or the phase.[25-32] It appears that the quenching rate is the primary variable that controls what phases form, the degree of particle agglomeration, and to some extent particle sizes.[26-32]

Sutorik and Baliat have briefly reported using LF-FSP to make $Ce_{1-x}Zr_xO_2$ solid solutions.[33] The current work, provides more details about these materials and also demonstrates a new facet of LF-FSP processing, directed phase segregation. Using directed phase segregation, we illustrate an approach to the one step production of $Ce_xZr_{1-x}O_2$ solid solutions on δ-Al_2O_3 supports with essentially any composition desired.

In this study, 70:30 element ratio mixtures of the proprionate precursors to CeO_2 and ZrO_2 and alumatrane typically at 2.5 wt% ceramic loading in EtOH were aerosolized with O_2 and combusted to produce $Ce_{1-x}Zr_xO_2$ and $[(CeO_2)_{0.7}(ZrO_2)_{0.3}]_x(Al_2O_3)_{1-x}$ (x = 0.3~0.9) composition nanopowders at rates of 50 g/h. The resulting materials are unagglomerated nanopowders with SSAs of 45±5 m^2/g without microporosity.

In the following section we begin by discussing alumina, ceria and zirconia precursor developed for LF-FSP processing. Thereafter we follow with the discussion of the LF-FSP processing and characterization of the $Ce_{1-x}Zr_xO_2$ and $[(CeO_2)_{0.7}(ZrO_2)_{0.3}]_x(Al_2O_3)_{1-x}$ (x = 0.3~0.9) materials using various analytical tools including XRD, BET, TGA-DTA, SEM, and FTIR.

Precursors and precursor formation

We previously reported the characterization of alumatrane $[N(CH_2CH_2O)_3Al]$, cerium propionate $Ce(O_2CCH_2CH_3)_3(OH)$, zirconium propionate $Zr(O_2CCH_2CH_3)_2(OH)_2$, and their use as a precursor in LF-FSP for the synthesis of δ-alumina, $(CeO_x)_{1-x}(Al_2O_3)_x$ and $(ZrO_2)_{1-x}(Al_2O_3)_x$ nanopowders.[27,28] These precursors have thermal decomposition patterns similar to other metal carboxylate precursors studied previously.[25-32]

For example, Figure **4.1** shows a TGA trace for $Zr(O_2CCH_2CH_3)_2(OH)_2$.[28] Initial mass losses (8%) are due to propionic acid of recrystallization. Thereafter, mass loss events are attributed to the decomposition of the propionate ligands as suggested in reactions (1)-(3). [25-32]

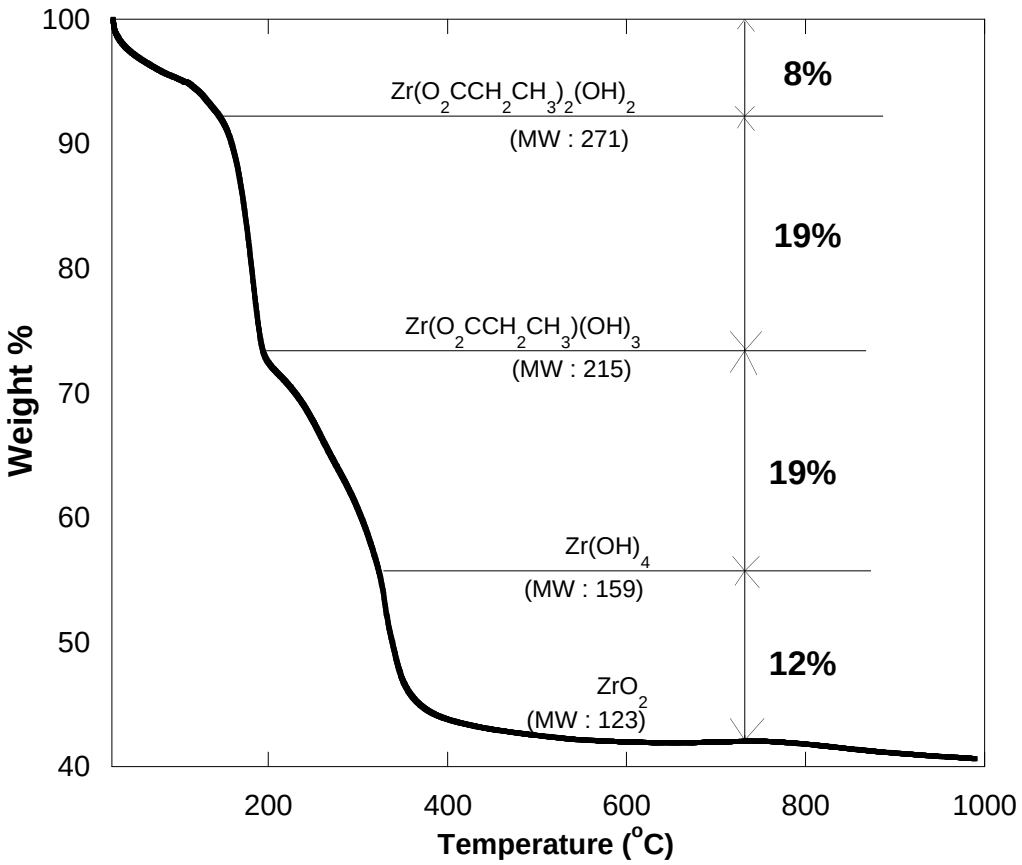

Figure 4.1. TGA of $Zr(O_2CCH_2CH_3)_2(OH)_2$ ramped at 10^oC/min in synthetic air.

$$Zr(O_2CCH_2CH_3)_2(OH)_2 \rightarrow Zr(O_2CCH_2CH_3)(OH)_3 + CH_3CH{=}C{=}O \quad (1)$$

Calc. (Found) Mass Loss = 19.01% (19%)

$$Zr(O_2CCH_2CH_3)(OH)_3 \rightarrow Zr(OH)_4 + CH_3CH{=}C{=}O \quad (2)$$

Calc. (Found) Mass Loss = 19.01% (19%)

$$Zr(OH)_4 \rightarrow ZrO_2 + 2H_2O \quad (3)$$

Calc. (Found) Mass Loss = 12.22% (12%)

Final ceramic yields [42% (ZrO_2)] are within experimental error of the calculated value (41.75%) from the decomposition of the precursor [$Zr(CH_3CH_2COO)_2(OH)_2$] to oxide (ZrO_2) and are as expected based on previous studies. [25-32]

XRD studies

XRD was used to characterize the phase compositions of as-processed LF-FSP nanopowders. In Figure **4.2**, the XRD patterns show that the (111) peak of cubic ceria shifts from its standard peak position 28.55^{o} 2θ to 28.91^{o} 2θ in the $Ce_{0.7}Zr_{0.3}O_2$ composition. We attribute this (111) peak shift to the formation of a solid solution. Because standard peak position for the (111) ceria peak (PDF file: 43-1002) is 28.55^{o} 2θ, and the (111) zirconia peak (PDF file: 42-1164) is 29.80^{o} 2θ, we can calculate the (111) peak position for $Ce_{0.7}Zr_{0.3}O_2$ using Vegard's law as 28.92^{o} 2θ. This matches the peak position (28.91^{o} 2θ) of our $(CeO_2)_{0.7}(ZrO_2)_{0.3}$ composition perfectly within the limits of XRD resolution (± 0.02^{o} 2θ).

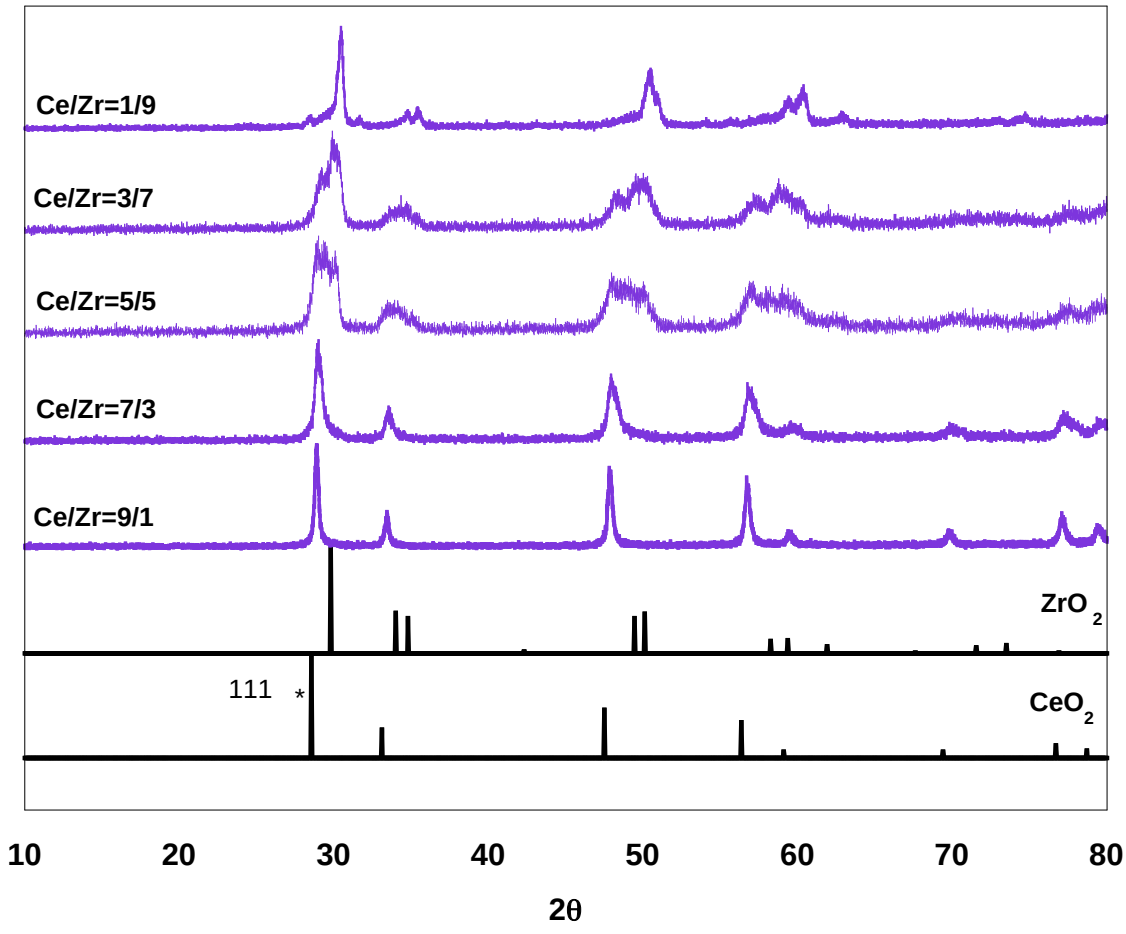

Figure 4.2. XRD patterns for LF-FSP as-produced $(CeO_2)_x(ZrO_2)_{1-x}$ nanopowders.

For the samples Ce:Zr = 1:1 and Ce:Zr = 3:7, we observe phase separation of the two possible phases (cubic ceria, t-zirconia) from the data analysis (see experimental). This contrasts with the work of Sutorik and Baliat[33] where at 1:1 only the solid solution was observed. However, the surface areas of their materials were closer to 15 m^2/g suggesting some influence of particle size and/or processing conditions on the product phase.

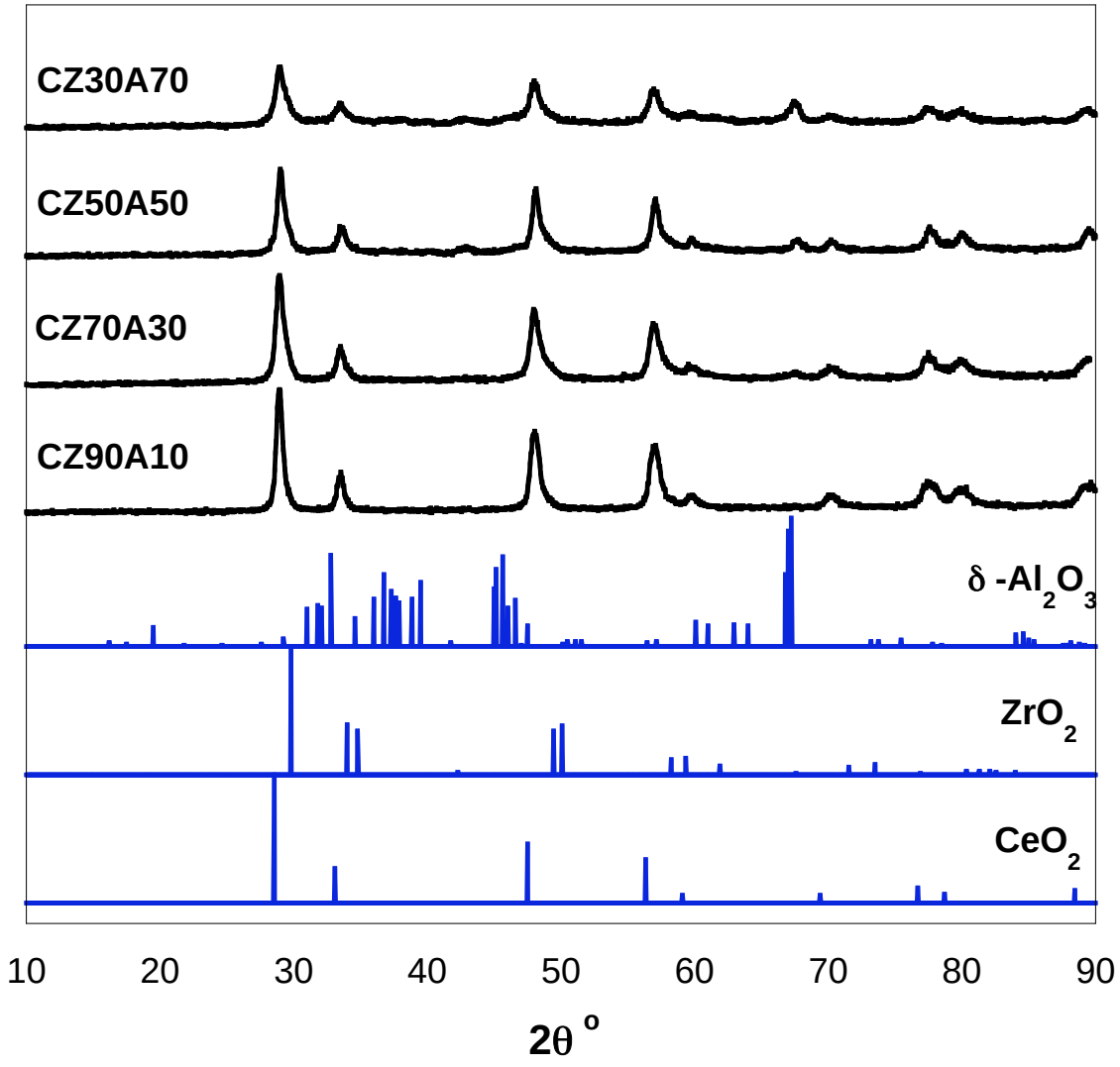

Figure 4.3. XRD powder patterns for compositions $(Ce_{0.7}Zr_{0.3}O_2)_x(Al_2O_3)_{1-x}$; CeO_2 (PDF file 43-1002), ZrO_2 (PDF file 42-1164), and δ-Al_2O_3 (PDF file 46-1131). CZ70A30 denotes $(Ce_{0.7}Zr_{0.3}O_2)_x(Al_2O_3)_{1-x}$, where x = 0.7

The Ce/Zr= 7/3 composition is that often used in commercial TWCs.[14-24] Hence we chose $Ce_{0.7}Zr_{0.3}O_2$ as the typical TWC composition and changed the relative amount of alumina and $Ce_{0.7}Zr_{0.3}O_2$ to make four samples of different compositions. The XRDs shown in Figure **4.3** were produced using a precursor system formulated to a $Ce_{0.7}Zr_{0.3}O_2$ composition and then mixed with an alumatrane $[Al(OCH_2CH_2)_3N]$ to obtain the ternary precursor compositions $[Ce_{0.7}Zr_{0.3}O_2]_x(Al_2O_3)_{1-x}$ (x = 0.3~0.9) used for LF-FSP processing.

By comparison with the XRD of $Ce_{0.7}Zr_{0.3}O_2$ in Figure **4.2,** we reproducibly generate the same cubic $(CeO_2)_{0.7}(ZrO_2)_{0.3}$ solid solution with alumina. The (111) peak position of four different $[Ce_{0.7}Zr_{0.3}O_2]_x(Al_2O_3)_{1-x}$ samples in Figure **4.3** (28.93^o 2θ) is close to the calculated (111) peak position of $Ce_{0.7}Zr_{0.3}O_2$ (28.92^o 2θ) within the limits of the XRD resolution (± 0.02^o 2θ).

Samples with higher $Ce_{0.7}Zr_{0.3}O_2$ loadings make it difficult to observe the δ-Al_2O_3 component in XRD patterns due to the relative peak intensity differences from higher Z value of Ce/Zr.

Average Particle Size (APS)

The APSs for these materials were estimated from Debye Scherer line broadening and their SSAs (Table **4.1**). Both methods give very similar results. The average SSAs for the Ce/Zr samples are ≈ 33±2 m^2/g, and those for the Ce/Zr/Al samples are 45±2 m^2/g. APS values for all of the powders generated are 10-15 nm.

It is important to note that here the higher *z* value of the Ce/Zr component might be expected to make it difficult to determine particle sizes from X-ray line broadening. In this instance, it is important that the BET derived values are similar. Furthermore, for the higher alumina loaded samples, the alumina might be expected to dominate the observed surface areas and therefore the particle sizes. The fact that the data are uniform for both methods over all types of powders suggests that both measurement methods are valid. However, SEM and TEM provide further substantiation.

Table 4.1. Average particle sizes and specific surface areas (SSA) of as produced LF-FSP samples

Sample	Debye-Scherrer Particle size (nm)	BET-derived Particle size (nm)	SSA (m^2/g)
$[(CeO_2)_{0.7}(ZrO_2)_{0.3}]_x(Al_2O_3)_{1-x}$ for x = 0.9	16	10	42
$[(CeO_2)_{0.7}(ZrO_2)_{0.3}]_x(Al_2O_3)_{1-x}$ for x = 0.7	13	11	45
$[(CeO_2)_{0.7}(ZrO_2)_{0.3}]_x(Al_2O_3)_{1-x}$ for x = 0.5	13	12	46
$[(CeO_2)_{0.7}(ZrO_2)_{0.3}]_x(Al_2O_3)_{1-x}$ for x = 0.3	11	13	47
$(CeO_2)_{0.1}(ZrO_2)_{0.9}$	16	16	32
$(CeO_2)_{0.3}(ZrO_2)_{0.7}$	16	15	32
$(CeO_2)_{0.5}(ZrO_2)_{0.5}$	16	14	32
$(CeO_2)_{0.7}(ZrO_2)_{0.3}$	16	13	33
$(CeO_2)_{0.9}(ZrO_2)_{0.1}$	16	11	36

Scanning electron microscopy (SEM) images

SEM images (Figures **4.4**) are presented to demonstrate the uniformity of both powder systems. SEM resolution is insufficient to carefully characterize nanopowders but it does provide a view of the general population. The goal here is to demonstrate that the particle populations produced by LF-FSP do not include any obvious micron size particles; although there are some weak agglomerates. Bell and Rodriguez demonstrated that LF-FSP δ-Al_2O_3 nanopowders disperse perfectly without any apparent evidence of aggregates.[34]

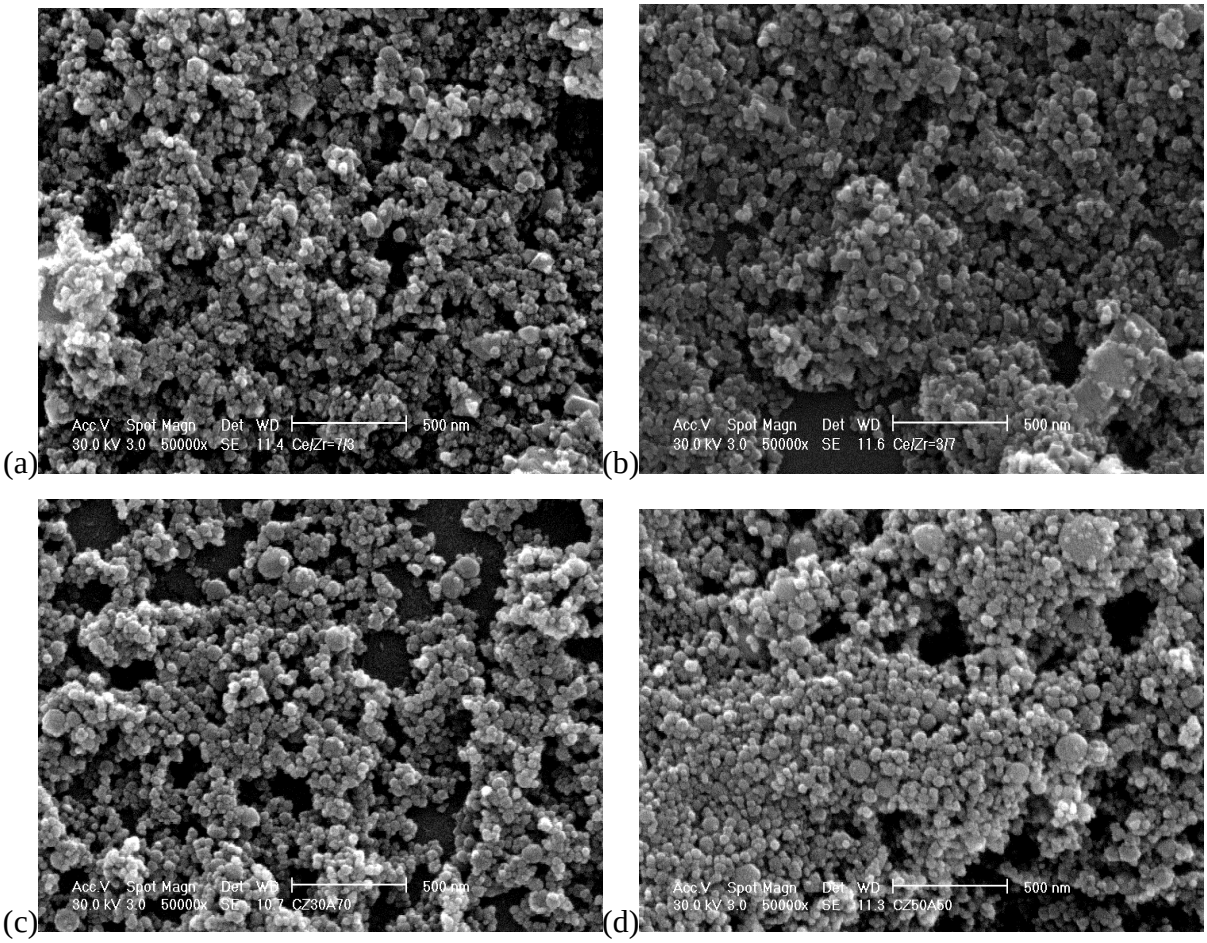

Figure 4.4. SEM images of **(a)** $(CeO_2)_{0.7}(ZrO_2)_{0.3}$ **(b)** $(CeO_2)_{0.3}(ZrO_2)_{0.7}$ **(c)** $[(CeO_2)_{0.7}(ZrO_2)_{0.3}]_x(Al_2O_3)_{1-x}$ for x = 0.7 **(d)** $[(CeO_2)_{0.7}(ZrO_2)_{0.3}]_x(Al_2O_3)_{1-x}$ for x = 0.5

Transmission electron microscopy (TEM) images

Discussions of actual size/size distributions are not appropriate if based solely on TEM micrographs, unless combined with the XRD results. Figure **4.5** shows high-resolution TEM images of $[Ce_{0.7}Zr_{0.3}O_2]_x(Al_2O_3)_{1-x}$ nanopowders from LF-FSP. Particle sizes here are typically below 30 nm in diameter with the vast majority < 20 nm.

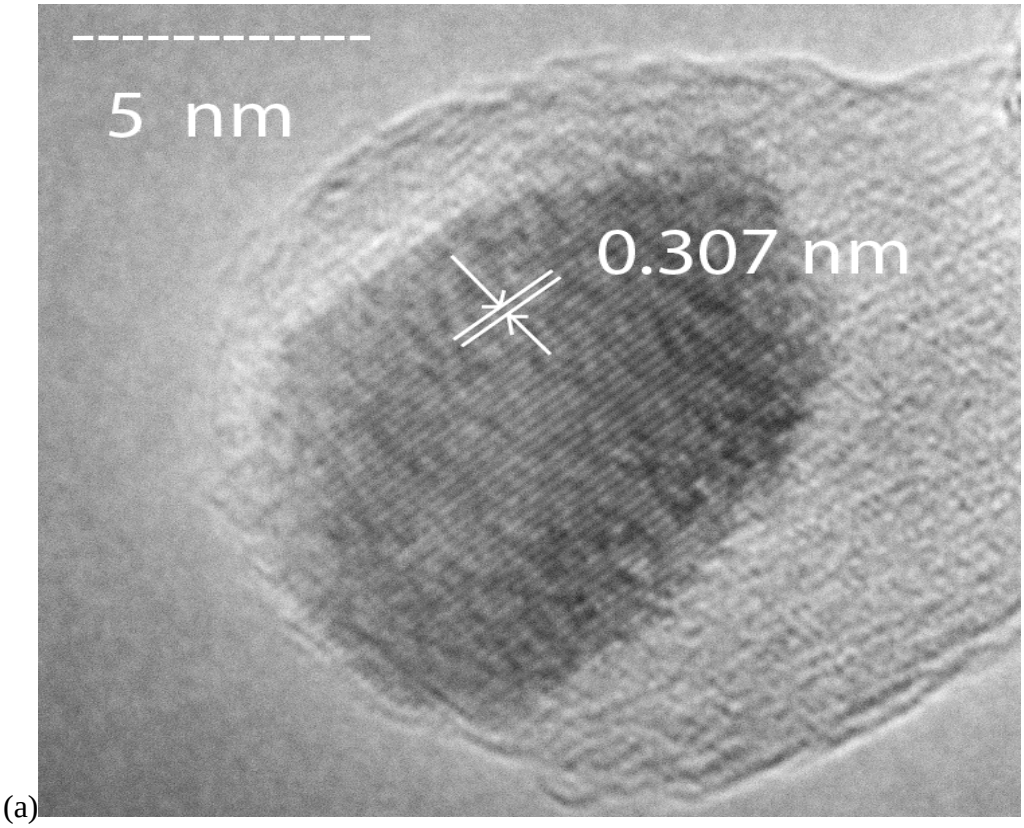

(a)

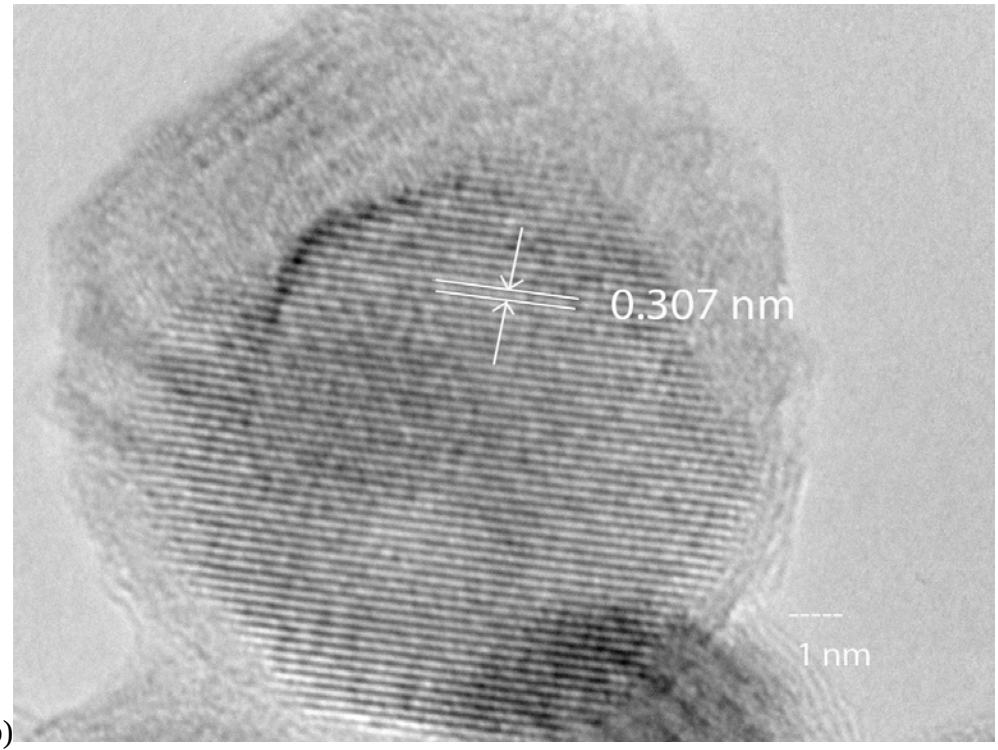

(b)

Figure 4.5. (a). TEM image of $(Ce_{0.7}Zr_{0.3}O_2)_{0.5}(Al_2O_3)_{0.5}$. (b). $(Ce_{0.7}Zr_{0.3}O_2)_{0.3}(Al_2O_3)_{0.7}$.

In Figure **4.5**, the clear lattice fringes show a high degree of crystallinity. Core-shell nanostructured nanopowders of $[Ce_{0.7}Zr_{0.3}O_2]_x(Al_2O_3)_{1-x}$ form due to the formation of cubic $Ce_{0.7}Zr_{0.3}O_2$ solid solution cores in δ-alumina nanopowders matching the XRDs of ceria-zirconia solid solutiuons and δ-alumina in Figure **4.3**. Because Al_2O_3 has a lower vaporization temperature (3000 ^oC) than CeO_2 (3906 ^oC) or ZrO_2 (5155 ^oC), [35,36] ZrO_2 and CeO_2 should co-condense and nucleate first followed by Al_2O_3 in LF-FSP processing. Thus we assume that $[Ce_{0.7}Zr_{0.3}O_2]$ nanoparticles form first during quenching, then δ-alumina wets the $[Ce_{0.7}Zr_{0.3}O_2]$ nanoparticles forming core-shell type nanopowders relatively uniformly in the LF-FSP system.

The d-spacings in Figure **4.5** images for the (111) plane of both the $(Ce_{0.7}Zr_{0.3}O_2)_{0.5}(Al_2O_3)_{0.5}$ and $(Ce_{0.7}Zr_{0.3}O_2)_{0.3}(Al_2O_3)_{0.7}$ nanopowders are the same 3.07 Å. This value (3.07 Å) for the (111) plane confirms the cubic $Ce_{0.7}Zr_{0.3}O_2$ solid solution as seen by the XRD in Figure **3**. It appears that nano single crystals of $Ce_{0.7}Zr_{0.3}O_2$ solid solution core form in non-crystalline transition alumina shell.

FTIR studies

Once the particle morphologies were characterized, a detailed picture of particle surface chemistries and thermal behavior was developed through FTIR examination of the particle surfaces per Figure **4.6**.

All of the materials exhibit weak νO-H absorptions in the 3700-2500 cm^{-1} region, attributable to surface hydroxyls arising from both physi- and chemi-sorbed water.[37,38] For two alumina rich samples (CZ5050, CZ30A70), νC-H bands were observed between 3000 and 2700 cm^{-1}.[38]

From 1800 to 1400 cm^{-1}, peaks attributable to traces of surface confined CO_2 and carbonates are observed again in accord with those seen for pure δ-Al_2O_3.[38] Peak intensities of CO_2 and carbonates are proportional to the amount of the alumina, because there are more organics in alumina rich samples. Absorption bands in the 1000-400 cm^{-1} region correspond to two νAl-O bands at 810 cm^{-1} (stretching vibrations of tetrahedrally coordinated Al-O) and 610 cm^{-1} (octahedrally coordination).[39] The νCe-O band (470 cm^{-1})[40] is not clearly shown here, due to the limit of machine.

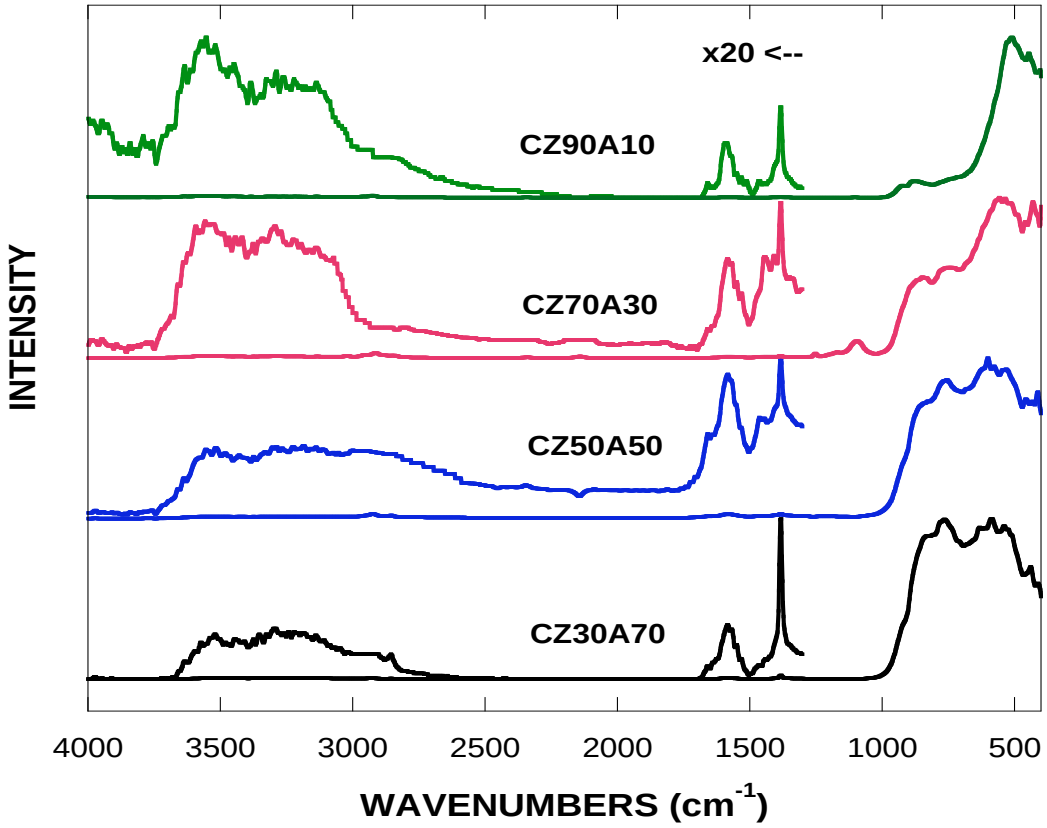

Figure 4.6. FTIR spectra of $(Ce_{0.7}Zr_{0.3}O_2)_X(Al_2O_3)_{1-X}$ for x = 0.3, 0.5, 0.7, and 0.9.

TGA-DTA studies

Figure **4.7** records the mass loss events for the $(Ce_{0.7}Zr_{0.3}O_2)_X(Al_2O_3)_{1-X}$ composition nanopowders. All as-processed powders exhibit 1-1.5 wt% mass-loss behavior up to ≈ 300°C. Much of this mass loss can be attributed to evolution of both physi- and chemisorbed water. Here the majority of the water is lost below ≈ 300°C.

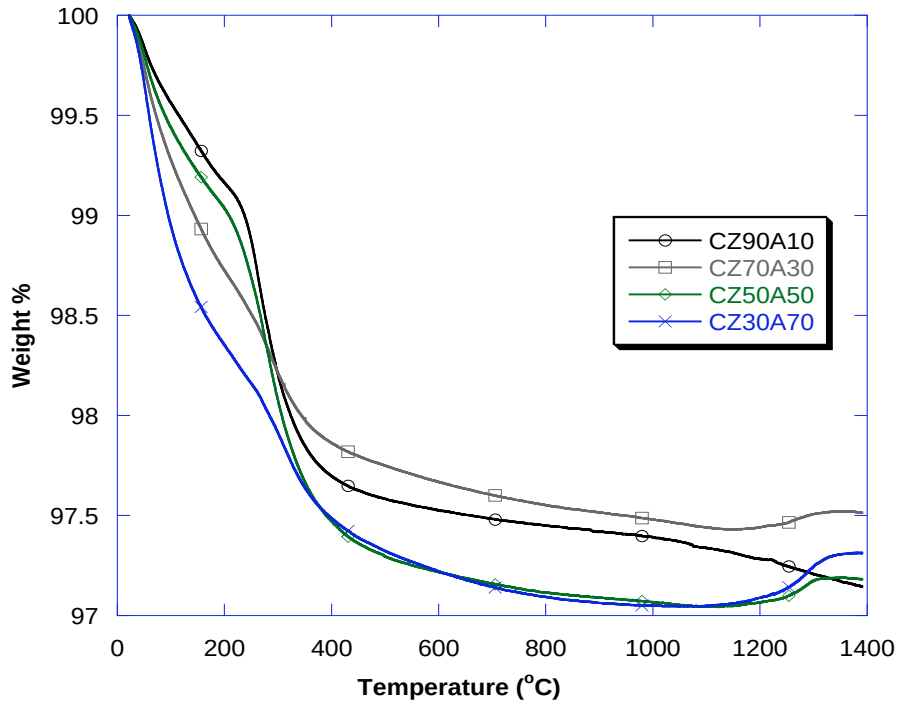

Figure 4.7. TGA of as-processed $(Ce_{0.7}Zr_{0.3}O_2)_x(Al_2O_3)_{1-x}$ ramped at 10°C/min/air.

The mass differences between air and nitrogen in the TGA and peak intensities around 300 °C in the DTA (Figure **4.9**) are proportional to the amount of alumina in three different samples (Figure **4.8a-c**). From the FT-IR data (Figure **4.6**), we see hydro-carbon species from νC-H bands in alumina rich samples (CZ30A70, CZ50A50). Thus, we presume that the mass differences between air and nitrogen in TGA and peak intensities around 300 °C in the DTA are due to the oxidation of organics of alumina rich samples.

At higher temperatures, we observe mass gains (TGA at ≥ 1200°C) with a corresponding exotherm in the DTA (Figure **4.9**). This may be attributable to the oxidation of residual $(Ce_{0.7}Zr_{0.3})^{3+}$ species dissolved in the δ-alumina component during LF-FSP processing, as we observed in previous studies.[27,28] Here we presume that the $(Ce_{0.7}Zr_{0.3})^{3+}$ species dissolved in the δ-Al_2O_3 lattice segregate out during the δ to α alumina transformation and oxidize to $Ce_{0.7}Zr_{0.3}O_2$. In Table **4.2,** we calculate the amounts of residual $(Ce_{0.7}Zr_{0.3})^{3+}$ species from the TGA mass gains during the δ to α alumina transformation.

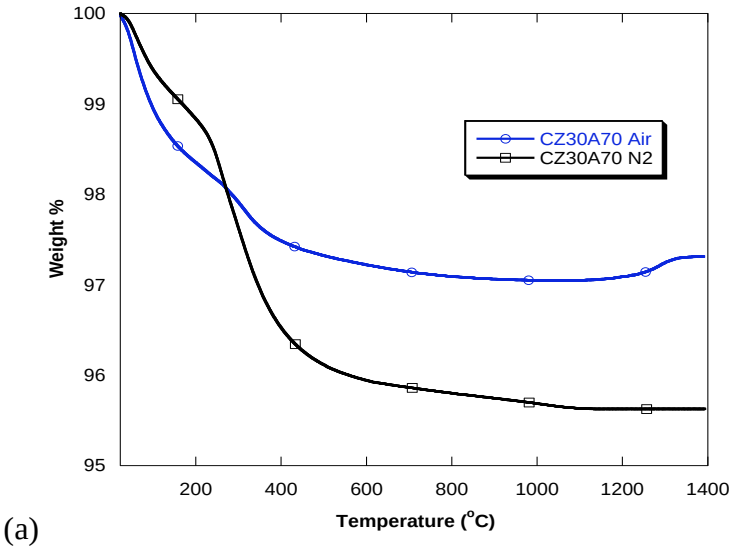

(a)

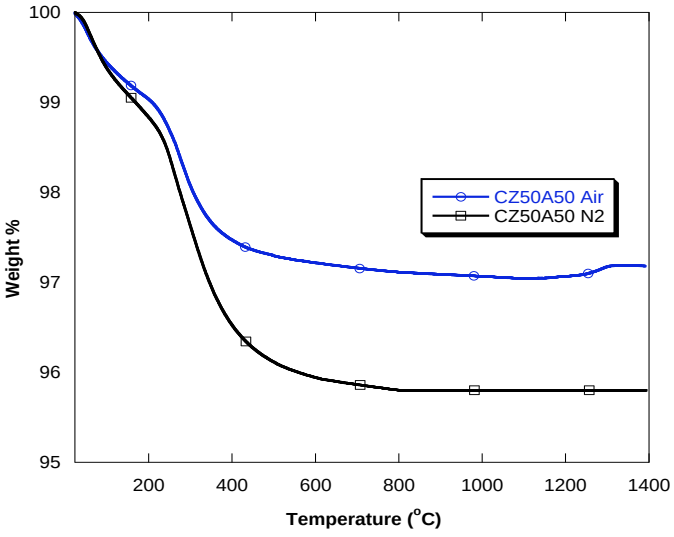

(b)

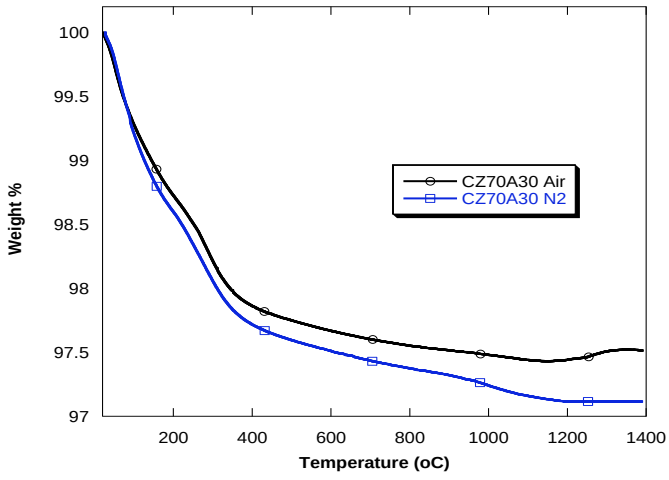

(c)

Figure 4.8. TGA of (a) $(Ce_{0.7}Zr_{0.3}O_2)_{0.3}(Al_2O_3)_{0.7}$ (b) $(Ce_{0.7}Zr_{0.3}O_2)_{0.5}(Al_2O_3)_{0.5}$ (c) $(Ce_{0.7}Zr_{0.3}O_2)_{0.7}(Al_2O_3)_{0.3}$ ramped at 10°C/min under air and nitrogen

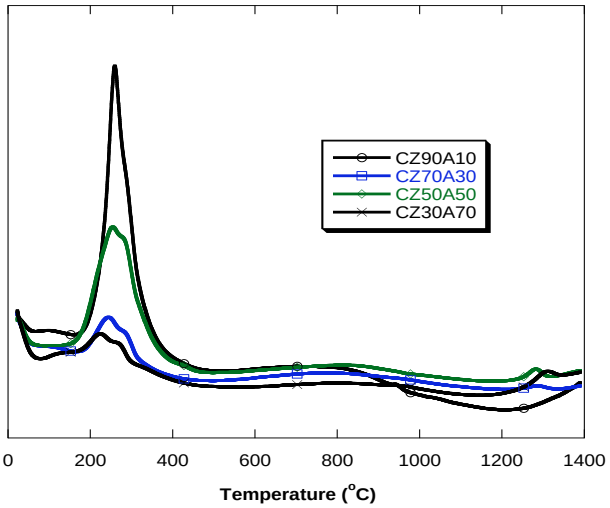

Figure 4.9. DTA of as-processed $(Ce_{0.7}Zr_{0.3}O_2)_{0.x}(Al_2O_3)_{1-x}$ nanopowders.

Table 4.2 Possible maximum residual $(Ce_{0.7}Zr_{0.3})^{3+}$ species in δ-alumina

Sample	Mass gain as O_2 content (wt%)	Possible maximum $(Ce_{0.7}Zr_{0.3})^{3+}$ species (mol ± 0.1 %)
CZ30A70	0.16	0.3
CZ50A50	0.18	0.3
CZ70A30	0.2	0.4

*Assumes all reduced species are $(Ce_{0.7}Zr_{0.3})^{3+}$

Like many of our previous studies, LF-FSP as-produced nanopowders generated by rapid quenching provide access to novel kinetic products not expected from traditional processing methods that typically drive formation through thermodynamic assumption on particle mixtures. Since traditional processing methods lead to thermodynamically rather than kinetically defined phase compositions, these materials may offer unique opportunities for variety of applications.

4.5 Conclusions

Key technical points suggest that LF-FSP processing can provide low-cost, efficient routes to well-known but enhanced catalyst materials, especially for emission control applications.

LF-FSP provides access to $(CeO_x)_x(ZrO_2)_{1-x}$ and $(Ce_{0.7}Zr_{0.3}O_2)_{0.x}(Al_2O_3)_{1-x}$ mixed-metal oxide nanopowders with exceptional control of stoichiometry and phase purity. We were able to produce nanopowders of any composition in the Ce-Zr-O and Ce-Zr-Al-O systems with specific surface area of ≥ 30 m^2/g at rates of 50-100 g/h. We were able to produce nano $Ce_{0.7}Zr_{0.3}O_2$ solid solution single crystals in the $(CeO_x)_x(ZrO_2)_{1-x}$ and $(Ce_{0.7}Zr_{0.3}O_2)_{0.x}(Al_2O_3)_{1-x}$ systems.

Most of all, we succeeded in producing core-shell nanoparticles in the $(Ce_{0.7}Zr_{0.3}O_2)_{0.x}(Al_2O_3)_{1-x}$ system in a single step with the correct choice of metalloorganic precursors. Because LF-FSP offers rapid quenching of the combustion species, it provides access to new, kinetic materials not accessible by any other conventional processing method. These nanopowders can offer novel potential for catalytic application.

4.6 References

1. H.W. Jen, G.W. Graham, W. Chun, RW. McCabe, J.P Cuif, S. Deutsch, O.Touret, "Characterization of Model automotive exhaust catalysts: Pd on Ceria and Ceria-zirconia supports," *Cat. Today* **50** 309-28 (1999).

2. M. Shelef, R.W. McCabe, "Twenty-five years after introduction of automotive catalysts: what next?," *Catal. Today,* **62**, 35-50 (2000).

3. H. S. Ghandi, G. W. Graham, " Automotive exhaust catalysis" *J. Cat.* **216** (2003) 433-422

4. R. G. Juan, A. G. Miguel, M. Jean-Louis, G. Pilar, B. Gilbert, "Effects of redox thermal treatments and feed dtream composition on the activity of Ce/Zr mixed oxides for TWC applications," *Appl. Cat. B: Environ.* **25** (2000) 19-29

5. H. C. Yao, H. K. Stephen, H. S. Ghandi, "The effect of SO_2 on the oxidation of hydrocarbons and carbon-monooxide over Pt/γ-Al_2O_3 catalysts," *J. Cat.* **67(1)** (1981) 231-236

6. T. Shido, Y. Iwasawa, "Reactant-promoted reaction mechanism for water-gas shift reaction on Rh-doped CeO_2" *J. Cat.* **141(1)** (1993) 71-81

7. J.-P. Cuif, G. Blanchard, O. Touret, A. Seigneurin, M. Marczi, E. Quemere, "(Ce,Zr)O_2 Solid solutions for Three-Way Catalysts," SAE 970463 (1997)

8. P. Marecot, L. Pirault, G. Mabilon, M. Prigent, J. Barbier, "Influence of the Redox Properties of Ceria on the Preparation of Three-Way Automotive Platinum-Rhodium/Alumina-Ceria Catalysts," *Appl. Catal. B,* **5** 57-69 (1994).

9. J. C. Clerc " Catalytic diesel exhaust aftertreatment" *Appl. Catal. B,* **10** 99-115 (1996)

10. S. Biamino, P. Fino, D. Fino, N. Russo, C. Baldini, " Catalyzed traps for diesel soot abatement: In situ processing and deposition of perovskite catalyst" *Appl. Catal. B,* **61** 297-305 (2005)

11. A. Yezerets, N. W. Currier, D. H. Kim, H. A. Eadler, W. S. Epling, C. H. F. Peden, " Differential kinetic analysis of diesel particulate matter (soot) oxidation by oxygen using a step-response technique." *Appl. Catal. B,* **61** 120-129 (2005)

12. S. J. Jelles, M. Makkee, J. A. Moujlin," Ultra low dosage of platinum and cerium fuel additives in diesel particulate control " *Topics in catalysis* **16/17,** 269-273 (2001)

13. A. Setiabudi, M. Makkee, J. A. Moujlin, " An optimal NOx assisted abatement of diesel soot in an advanced catalytic filter design" *Appl. Catal. B,* **42**, 35-45 (2003)

14. J. G. Nuan, "Physico-Chmical and Catalytic Properties of CeO_2-ZrO_2 Solid Solutions

Supported and dispersed on γ-Al_2O_3" SAE 970467 (1997)

15. R. W. McCabe, J. M. Kisenyi " Advances in automotive catalyst technology" *Chemistry & Industry* **15**, 605 (1995)

16. H. Permana, D.N. Belton, K.M. Rahmoeller, S.J. Schmieg, C.E. Hori, A. Brenner, K.Y.S. Ng, "Reactor Evaluation of Ceria-Zirconia as an Oxygen Storage Material for Automotive Catalysts," SAE 970462 (1997).

17. J. A. Cairns, A.C. Hourd, S.P. Scott, J. Thomson, H. Bradshaw, P. Goulding, l. McAlpine, P. Moles, C. Norman, "A Novel Palladium Catalyst for Use in Vehicle Emissions Control," SAE 970468 (1997).

18. M. Shelef, G. W. Graham, R. W. McCabe "Catalysis by ceria and related Materials" *Imperial College Press*, London, 2002, p343

19. H.S. Gandhi, W. B. Williamson, E. M. Logothetis, J, Tabock, C. Peters, M. D. Hurley, M. Shelef "Affinity of lead for noble-metals on different supports" *Surf. Interf. Anal.* **6(4)** 149-161 (1984)

20. J. T. Kummer, "Use of noble metals in automotive exhaust catalyst" *J. Phys. Chem.* **90(20)** 4747-4752 (1986)

21. T. Yamada, T. Kobayashi, K. Kayano, M. Funabiki, "Development of Zr containing TWC catalysts" SAE Paper 970466

22. R. Kemmler, A. Waltner, C. Schon, S. Godwin, "Current Status and Prospects for Gasoline Engine Emission Control Technolgoy-Paving the Way for Minimial Emissions," SAE Paper 2000-01-0856.

23. L. Mussmann, D. Lindner, E.S. Lox, R. van Yperen, T.P Kreuzer, l. Misushima, S. Taniguchi, G. Gaff, "The Role of Zirconium in Novel Three-Way Catalysts," SAE 970465 (1997).

24. M. H. Yao, R.J. Baird, F.W. Kunz, T. E. Hoost, " An XRD and TEM Investigation of the Structure of Alumina Supported Ceria-Zirconia" *J. Cat.* **166** 67-74 (1997)

25. T. Hinklin, B. Toury, C. Gervais, F. Babonneau, J. J. Gislason, R. W. Morton, R. M. Laine, "Liquid-feed flame spray pyrolysis of metalloorganic and inorganic alumina sources in the production of nanoalumina powders," *Chem. Mater*. **16**, 21-30 (2004).

26. J. Marchal, T. Johns, R. Baranwal, T. Hinklin, R. M. Laine, "Yttrium aluminum garnet nanopowders produced by liquid-feed flame spray pyrolysis (LF-FSP) of metalloorganic precursors," *Chem. Mater*. **16** 822-831 (2004)

27. M. Kim, T. R. Hinklin, R. M. Laine, "Core-shell nanostructure nanopowders along

$(CeO_x)_x(Al_2O_3)_{1-x}$ tie-line by liquid-feed flame spray pyrolysis (LF-FSP)" submitted to *Chem. Mater.* (2008).

28. M. Kim. R. M. Laine, "Liquid-feed flame spray pyrolysis (LF-FSP) for combinatorial processing of nanooxide powders along the $(ZrO_2)_{1-x}(Al_2O_3)_x$ tie-line. Phase segregation and the formation of core-shell nanoparticles," *J. Cer. Proc. Res.* ***8*** *129-136* (2007).

29. S. Kim, J. J. Gislason, R.W. Morton, X. Q. Pan, H. P. Sun, R. M. Laine, "Liquid-feed flame spray pyrolysis of nanopowders in the alumina-titania System," *Chem. Mater.* **16**, 2336-2343 (2004).

30. J. A. Azurdia, J. Marchal, R. M. Laine, " Synthesis and characterization of mixed-metal oxide nanopowders along the CoO_x–Al_2O_3 tie line using liquid-feed flame spray pyrolysis," *J. Am. Ceram. Soc.*, **89[9]** 2749–2756 (2006)

31. J. A. Azurdia, J. Marchal, P. Shea, H. Sun, X. Q. Pan, R. M. Laine, " Liquid-feed flame spray pyrolysis as a method of producing mixed-metal oxide nanopowders of potential interest as catalytic materials. Nanopowders along the NiO-Al_2O_3 tie line including $(NiO)_{0.22}(Al_2O_3)_{0.78}$, a new inverse spinel composition," *Chem. Mater.* **18** (2006) 731-739

32. R. M. Laine, B. L. Mueller, T. Hinklin, U.S. Patent 5,418,298, 1995.

33. A. C. Sutorik, M. S. Baliat "Solid solution behavior of CexZr1-xO2 nanopowders prepared by flame spray pyrolysis of solvent-borne precursors" *Mat. Sci. For.* **386-388** pp.371-376 (2002)

34. N. S. Bell, M.A. Rodriguez, "Dispersion properties of an alumina nanopowder using molecular, polyelectrolyte, and steric stabilization" *J. Nanosci. Nanotech*. **2004**, 4(3), 283-290

35. R. Jossen, S. E. Pratsinis, W. J. Stark, and L. Madler "Criteria for Flame-Spray Synthesis of Hollow, Shell-Like, or Inhomogeneous Oxides" *J. Am. Ceram. Soc*. **88** [6] 1388-1393 (2005)

36. CRC handbook of chemistry and physics. 80th ed.**1999-2000**. CRC press

37. J. B. Peri, "Infrared and gravimetric study of the structure hydration of γ-alumina" *J. Phys. Chem*. **1965**, 69, 211

38. P. Tarte. "Infrared spectra of inorganic aluminates and characteristic vibrational frequencies of AlO_4 tetrahedra and AlO_6 octahedra" *Spectrochim. Acta* **1967**, 23A, 2127

39. J. M. Saniger, "Al-O infrared vibrational frequencies of γ-alumina," *Mater. Lett.*

1995, 22, 109-113

40. P. G. Harrison, W. Daniell “Catalytic activity, surface redox properties, and structural evolution during the thermal processing of chromium-promoted ceria oxidation catalysts” *Chem. Mater.* **13** 1708-1719 (2001)

CHAPTER 5

SINTERING STUDIES OF $(ZrO_2)_x(Al_2O_3)_{1-x}$ CORE-SHELL NANOPOWDERS

5.1 Experimental

Liquid-feed flame spray pyrolysis (LF-FSP)

LF-FSP, as practiced at the University of Michigan, has been described in detail in published papers.[1-6] The LF-FSP process aerosolizes mixtures of metalloorganic precursors (single- or mixed-metal alkoxides, carboxylates or β-diketonates) dissolved in alcohol solvents (typically EtOH) at known concentration levels using oxygen. The resulting aerosol is ignited via methane pilot torches followed by combusting the mixture into a 1.5 m long quartz chamber. Initial combustion temperatures run 1500°-2000°C, depending on the processing conditions, generating nanopowder "soot" collected using wire-in-tube electrostatic precipitators (ESP) as detailed elsewhere.[1-6]

Temperatures drop to 300-500 °C over 1.5 meters, equivalent to a 1000°C quench in ≤ 100 msec leading to kinetic products and nanopowders that are largely unaggregated; although they are lightly agglomerated. "Shooting" rates can be up to 300 g/h when using wire-in-tube electrostatic precipitators operating at 10 kV. Typical powders have average particle sizes (APSs) of 15 to 100 nm with specific surface areas (SSAs) of 30 to 100 m^2/g.

Fabrication of Green body

The as-produced LF-FSP powders (3.0 g) were dispersed with 5 mg DARVAN C-N® (R.T. Vanderbilt company, Inc) in 100 mL EtOH using a 1.2 cm diameter 500 W ultrasonic horn (Sonics and Materials 600 VCX, Newtown, CT) at 40% of full power for 12 h in a 500 mL Teflon beaker. The dispersion was allowed to settle for 24 h. Thereafter the emulsion was further processed by adding 5 mg of polyethylene glycol 3400 D (Sigma-Aldrich) and treated with the 500 W ultrasonic horn for an additional 6 h.

Then the dispersion was rotary evaporated for 6 h and air-dried for 12 h at 150°C. After 12 h air drying, dispersion was put in the vacuum oven at 200 °C for 12 h. The dried powders were ground lightly for 30 min in an alumina mortar and pestle and sieved using –325 nylon mesh in an acrylic holder. The ground and sieved powder (600 mg)

was pressed (50 MPa) in a dual action 12 mm WC die followed by cold isostatic pressing (CIPped) (200 MPa) (Autoclave Engineers, Erie, PA) for 6 h. The pressed pellets were subjected to binder burn out by heating in air (1°C/min to 800°C, followed by a dwell at 800°C for 6 h).

Dilatometry studies

Dilatometry was run using a Theta Industries Dilatronic 6500 (Port Washington, NY) with a thermal expansion head under mild compression. Data was collected from using LabView program. Flat, square pellets, avg. 1.27 mm on a side, used for the dilatometry runs were sectioned and placed between an alumina block and the alumina push rod. Constant heating rate (CHR) experiments were conducted with heating rate 5°C/min to 1450°C in static air/oxygen.

XRD studies

As-prepared samples were characterized using a Rigaku Rotating Anode Goniometer. Powder and pellet samples were prepared by placing ≈ 100 (powder), 500 (pellet) mg on XRD sample holders (amorphous silica slides) for data collection. CuKα (λ = 1.54 Å) radiation with a Ni filter was used with a working voltage and current of 40 kV and 100 mA, respectively. Scans were continuous from 20–80° 2θ with a step scan of 2° 2θ/min in increments of 0.05° 2θ. Peak positions and relative intensities were characterized by comparison with PDF files of standard materials: δ-Al_2O_3 (PDF file 46-1131), α-alumina (PDF file 42-1164), Tetragonal ZrO_2 (PDF file 42-1164), Monoclinic ZrO_2 (PDF file 04-006-7558).

Scanning electron microscopy (SEM)

A high resolution SEM (FEI NOVA Dualbeam Focused Ion Beam Workstation and Scanning Electron Microscope) was used for images of pellets. Pellets were polished by SiC papers from 600 grids to 2400 grids and diamond powders of diameters from 9 μm to 500 nm. Pellets were sputter coated with 1-5 nm of Au-Pd to reduce charging effects. The operating voltage was from 5.0 to 10.0 kV.

Grinding ceramic composites

$(ZrO_2)_{0.54}(Al_2O_3)_{0.45}$ sample sintered at 1120 ^oC was used in an attempt to observe the tetragonal to monoclinic zirconia phase transformation, as the evidence of partially stabilized zirconia. We cut a portion of sintered $(ZrO_2)_x(Al_2O_3)_{1-x}$ pellet to flat, square

pellet, 0.5 mm on a side, using diamond saw, ground the portion in alumina mortar with alumina pestle, and recorded XRD patterns of ground powders at the time of the fracture and after 1, 5, 10 minutes of grinding .

5.2 Background, Results and Discussion

The objectives of the current study are to produce and characterize fully dense $(ZrO_2)_x(Al_2O_3)_{1-x}$ ceramic nanocomposites with homogeneous, nanosize grains from LF-FSP produced core-shell nanopowders as a prelude to exploring their potential for structural and especially for biomedical applications.[7,8]

Previously, we reported the synthesis of $(ZrO_2)_{1-x}(Al_2O_3)_x$ nanopowders with molar ratios that span the ZrO_2-Al_2O_3 composition range.[6] Liquid-feed flame spray pyrolysis (LF-FSP) of mixtures of $N(CH_2CH_2O)_3Al$ (alumatrane) and $Zr(CH_3CH_2COO)_2(OH)_2$ precursors dissolved in ethanol, were aerosolized with O_2, combusted at temperatures of 1500-2000°C and quenched rapidly thereafter to provide $(ZrO_2)_{1-x}(Al_2O_3)_x$ nanopowders of selected compositions. All powders exhibit average particle sizes (APSs) < 20 nm and corresponding surface areas of ≈ 50 m^2/g when produced at rates of 100-300 g/h. We were able to make core-shell nanostructured $(ZrO_2)_{1-x}(Al_2O_3)_x$ nanopowders at compositions of x = 0.3-0.8, Because LF-FSP allows rapid quenching of the combustion species, it offers unique routes to new, metastable nanopowders with high surface energies not accessible by conventional processing methods.

ZTA (0-26 mole% zirconia toughened alumina) properties

ZTA has received significant attention over the past two decades because of its high toughness, good resistance to wear for the structural applications in general, and chemical stability for prosthetic applications in particular.[7,8,14-18,24,25] ZTA is widely known to combine the high hardness of alumina with the high toughness of tetragonal zirconia.[9] Pure, dense alumina offers relatively high hardness (1500 Kg/mm^2) with good flexural strength (380 MPa) but relatively poor toughness (K_{IC}= 4 $MPa*m^{1/2}$),[9-12] while yttria partially stabilized tetragonal zirconia provides higher flexural strength (900 MPa), higher toughness (K_{IC}= 15 $MPa*m^{1/2}$), but lower hardness (1100 Kg/mm^2),[10-12] and can self-degrade to the monoclinic phase under 400 ^oC through surface reactions between yttria with water.[13] Therefore $(ZrO_2)_{1-x}(Al_2O_3)_x$ composites offer enhanced mechanical properties compared with pure t-zirconia and α-alumina.

ZTA compositions

Typical ZTA composites contain up to 30 wt% (26 mole%, 24 vol.%) partially stabilized zirconia, and offer improved mechanical properties (Fracture toughness K_{IC} = 5 - 10 MPa*$m^{1/2}$; Flexural strength = 500 - 940 MPa) for structural applications by using the martensitic transformation of tetragonal zirconia to monoclinic zirconia in an α alumina matrix.[14-18,24,25] At room temperature, the magnitude of toughening is proportional to the magnitude of the fracture toughness.[14-16,24,25]

The maximum amount of t-zirconia is usually limited to 30 wt% due to the difficulties in sintering zirconia.[14,15] If the amount of partially stabilized t-zirconia exceeds 30 wt%, it becomes more difficult to densify ZTA composites, based on the results of Magnani et, al.[14] and Zarate et, al.[15] Also, most studies start with α-alumina powders,[16-18] such that final densities with pressureless sintering are typically ≤ 96 %, because of the low grain boundary diffusivities of t-zirconia and α-alumina ($10^{-25}/m^3s^{-1}$) at normal sintering temperatures prohibiting densification of ZTA composites.[26] HIPping is used frequently to overcome these problems, but even densities resulting from HIPping are often less than 99%.[16,17]

For ZTA with micron size grains, yttria is used as a stabilizer to retain partially stabilized t-zirconia.[19-21] Tetragonal zirconia with ≤ 3 mole% yttria will transform to the monoclinic zirconia causing a 4% volume expansion. For additions of more than 3 mol% (3.6 mole%) yttria, t-zirconia transforms to cubic zirconia with low fracture toughness (K_{IC} = 5 MPa*$m^{1/2}$)[18] limiting mechanical properties. However, Mayo et, al.[22] and Morikawa at. al.[23] suggest that ZTA with very fine grains < 1 μm can have partially stabilized tetragonal zirconia without any stabilizing doppant due to smaller grain sizes.

ZTA processing

Most current ZTA processing involves mechanical mixing of micron sized partially stabilized zirconia/pure α-alumina powders or sol-gel processing of zirconia/alumina precursor mixtures. [7,8,14-18,24,25] Magnani et al[14], Tuan et al[24] , and Gnanam et al[25] were able to produce full density (99+%) ZTA composites with 30 wt% yttria stabilized zirconia using sol-gel methods. However, grain sizes of most current ZTA studies is micron-size.

Both powder mixing and sol-gel processing require multiple steps to produce

green compacts. Furthermore, most current studies that use pressureless sintering go to temperatures of at least 1600 ^{o}C, followed by HIPing (Hot isostatic pressing) at ≥1500 ^{o}C to achieve final composite densities of 99+%.[17,18,24] This is mainly due to the similar same grain boundary diffusivity (10^{-25} /m^3s^{-1}) of t-zirconia and α-alumina. These types of processing are not efficient in time and cost.

Because δ-alumina has a much higher grain boundary diffusivity (10^{-23} /m^3s^{-1}) than t-zirconia (10^{-25} /m^3s^{-1}) at ≥ 800 ^{o}C, [26,27] we might expect our t-$(ZrO_2)_x(Al_2O_3)_{1-x}$ core-shell nanopowders to sinter more easily. Furthermore, we might expect the δ-alumina shell to sinter on its own, while the tetragonal zirconia with slow bulk diffusion rates contribute little to densification. Thus, we expect the microstructure of separated nano-size t-zirconia grains without yttria and α-alumina grains due to isothermal heating from sintering procedure with no pores. Based on the above idea, we hoped to produce final composites with nano-size t-zirconia and α-alumina grains using our $(ZrO_2)_x(Al_2O_3)_{1-x}$ core-shell nanopowders with APSs ≤ 20 nm.

On the basis of above arguments, we report efforts to produce fully dense nanostructured ZTA nanocomposites with densities ≥ 99%. Our $(ZrO_2)_x(Al_2O_3)_{1-x}$ core-shell nanopowders allow us to produce fully dense ZTA nanocomposites with grain sizes < 200 nm using pressureless sintering in air at < 1150 ^{o}C. The t to m phase transformation of nano zirconia grains without yttria was observed by applying stress, as evidence of the potential for structural applications. These fully dense nanostructured ZTA nanocomposites may offer improved strength, fracture toughness, thermal shock resistance, and thus potential for structural and especially biomedical applications.

We begin by discussing the characteristics of the $(ZrO_2)_{0.54}(Al_2O_3)_{0.45}$ source powder, processing source powders to fully dense composites, and then characterize the final ceramic composites sintered at different temperatures using the x-ray diffraction (XRD) and high resolution scanning electron microscopy (HR-SEM). Thereafter we follow with discussions on the phase transformation behavior of $(ZrO_2)_{0.54}(Al_2O_3)_{0.45}$ nanopowder compacts sintered at different temperatures.

$(ZrO_2)_{0.54}(Al_2O_3)_{0.45}$ source powders

Here we begin by describing the general characteristics of our source materials. Figure **5.1** shows obvious unidirectional (101) lattice planes (d= 0.29 Å) in a single nanoparticle. The d-spacing from the TEM images confirms our XRD results showing the tetragonal phase zirconia core in $(ZrO_2)_{0.54}(Al_2O_3)_{0.45}$ nanoparticle.[6] Therefore, as discussed above, we might expect δ- alumina to sinter while preserving the single crystal t-zirconia cores due to differences in the diffusion rates between t-zirconia and δ-alumina as discussed in the following section.

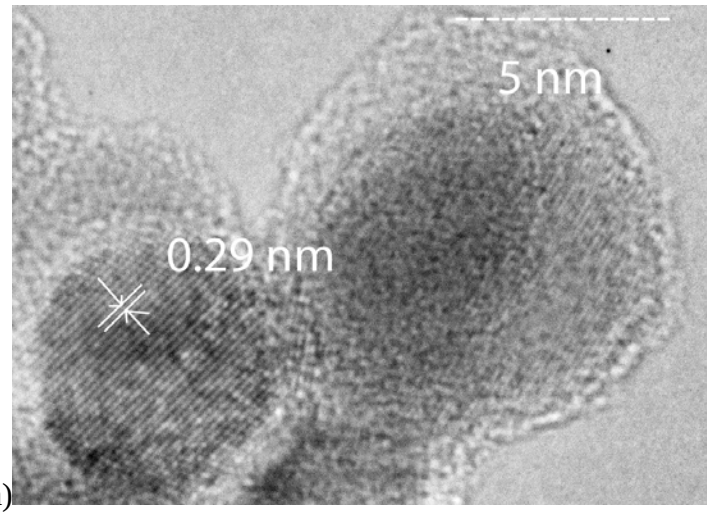

(a)

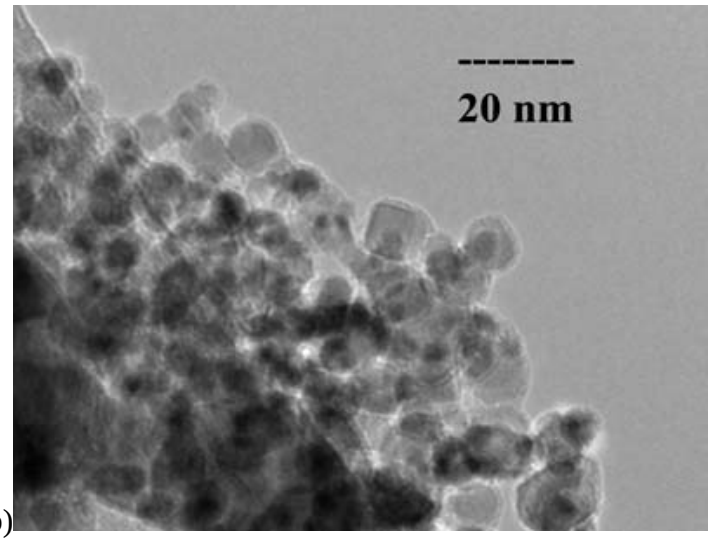

(b)

Figure 5.1. TEM images of $(ZrO_2)_{0.54}(Al_2O_3)_{0.45}$ nanopowders

Dilatometry Studies

Dilatometry provides the basis for developing heating schedules to optimize sintering conditions to make fully dense composites. In these studies, $(ZrO_2)_{0.54}(Al_2O_3)_{0.45}$ core-shell nanopowders were processed (see exp.) with 2 wt % binder (polyethylene glycol), cold isostactic pressed (CIPped 200MPa) to form green bodies, and heated in air at 1 ^oC/min to 800 ^oC for binder burn out.

The resulting $(ZrO_2)_{0.54}(Al_2O_3)_{0.45}$ 12.7 mm discs with avg. 1.4 mm thickness were cut with the diamond saw to form flat, squares with 1.27 mm sides that were placed in the dilatometer. Samples were heated in synthetic air at 5 ^oC/min to 1425 ^oC providing the trace shown in Figure **5.2**.

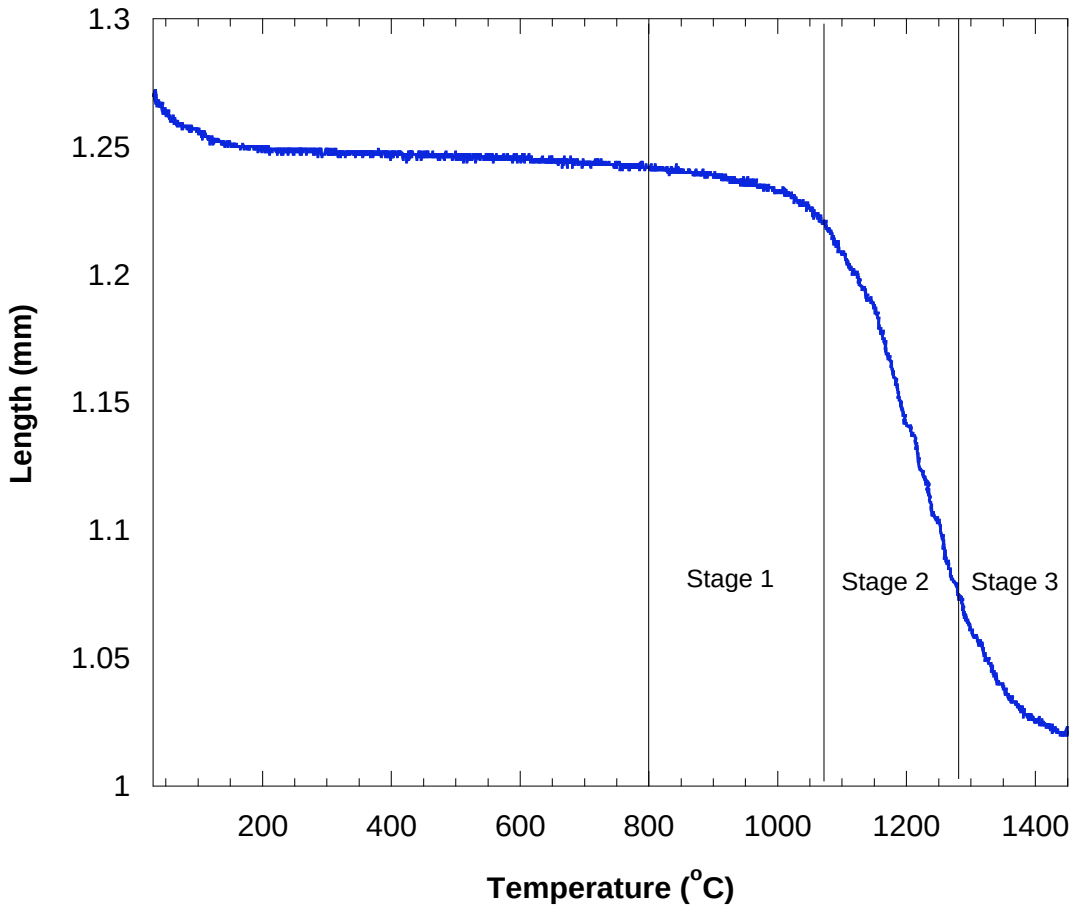

Figure 5.2. Dilatometry plot of $(ZrO_2)_{0.54}(Al_2O_3)_{0.45}$ nanopowder compact ramped at 5 ^oC/min in synthetic air. (Average plot of 6 different runs)

Figure **5.2** shows the three typical stages of sintering.[28-31] In the first stage (800 - 1060 ^{o}C), sintering begins at 800 ^{o}C. Here the interparticle contact area increases by neck formation. In this temperature range, external pressure and heating cause the rearrangement of grains. In the second stage (1060-1270 ^{o}C), continuous pore networks form, and the relative density increases by continuous shrinkage of pores and neck growth. Because δ-alumina has higher grain boundary diffusivity (10^{-23} /m^3s^{-1}) than zirconia (10^{-25} /m^3s^{-1}) at ≥ 800 ^{o}C,[26,27] we expect the δ-alumina shell to fill the pores between grains with the tetragonal zirconia contributing little to densification.

The final stage (1270-1425 ^{o}C) begins when pores become isolated and are eventually eliminated. According to various studies on ceramic sintering,[28-31] one can expect significant grain growth during this final stage. This grain growth will certainly prohibit producing dense ceramic composites with grains sizes 100 nm. Since our intention was to minimize final grain sizes, sintering temperatures of 1100-1200 ^{o}C were chosen.

Based on these dilatometer studies, we selected final dwell temperatures for sintering between 1050 and 1200 ^{o}C with ramp rates of 10 ^{o}C/min, and dwell times of 6 h in air, as described in Table **5.1**. For density measurements (Table **1**), we used Archimedes method. We were able to obtain full density at ≥1120 ^{o}C.

Table 5.1. Relative density of $(ZrO_2)_{0.5}(Al_2O_3)_{0.5}$ pellet along processing condition

Processing condition	Relative density
Before binder burn-out	0.46
After Binder burn-out	0.51
Heat to 1070 ^{o}C	0.83
Heat to 1120 ^{o}C	0.99
Heat to 1125 ^{o}C	0.99
Heat to 1145 ^{o}C	0.99
Heat to 1200 ^{o}C	0.99

Microstructures of heated composites

Figure **5.2a** shows the HR-SEM image of a fully dense $(ZrO_2)_{0.54}(Al_2O_3)_{0.45}$ pellet used for dilatometry studies (heated to 1425 ^{o}C, ramped at 5 ^{o}C/min in synthetic air).

Large grains (≥ 1 micron) were observed similar to the other studies,[2,7] because of grain growth above 1300 ^{o}C. In Figure **5.2b**, grain sizes found at 1200 ^{o}C are ~ 500 nm at nearly full density (Table **5.1**). As expected, grain growth is slower at 1200 ^{o}C. For the sample sintered at 1120 ^{o}C (Figure **5.2c**), the image shows average grain sizes of 200 nm and a fully dense microstructure after polishing with diamond media. In the image of the 1070 ^{o}C sample (Figure **5.2d**), we observe that the final composite is not fully dense, matching our density data (0.83) in Table **5.1**.

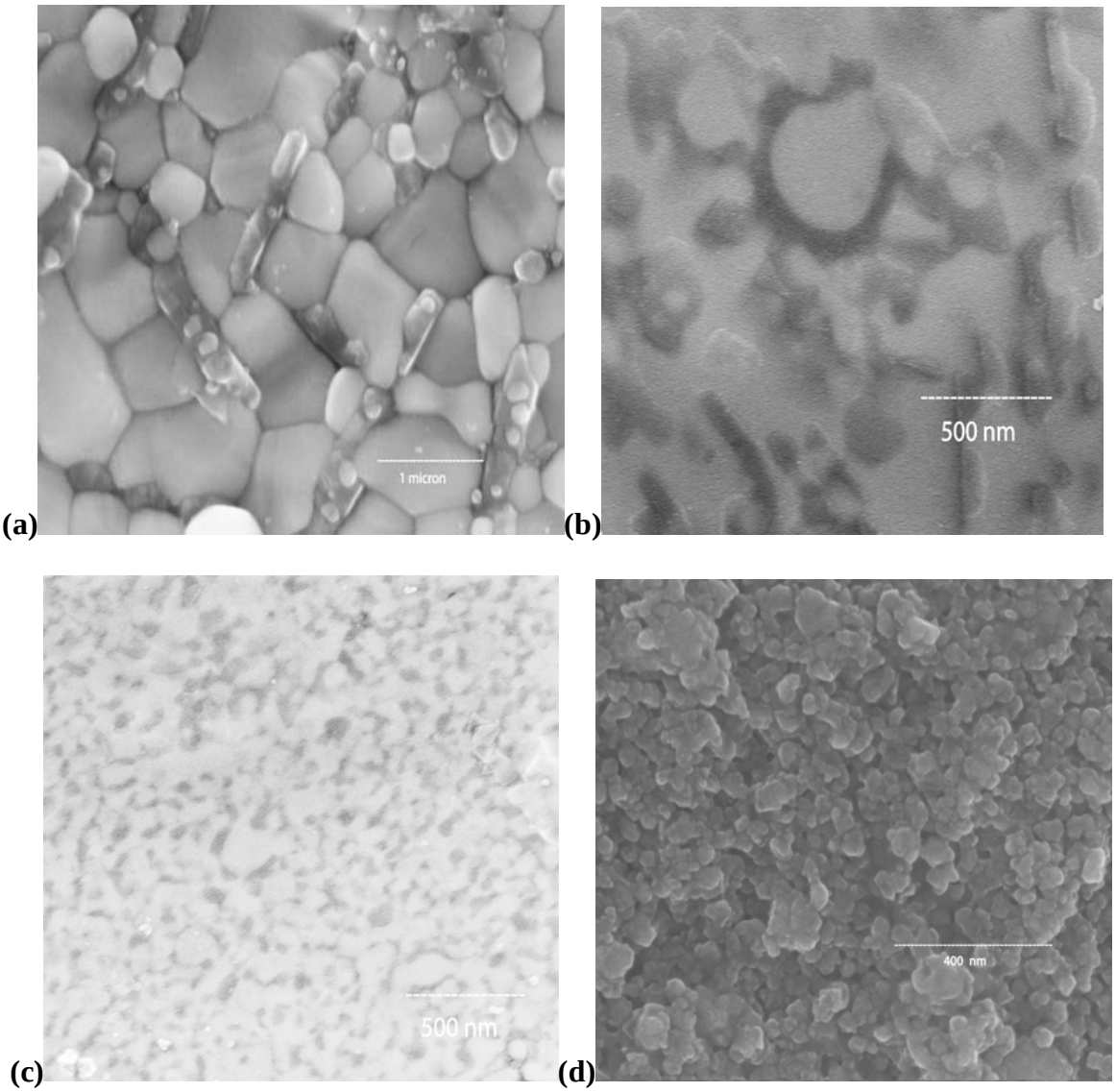

(a) **(b)** **(c)** **(d)**

Figure 5.3. **(a)** $(ZrO_2)_{0.54}(Al_2O_3)_{0.45}$ pellet heated to 1425 ^{o}C for 0.5h at 1 ^{o}C/min/air in dilatometer. $(ZrO_2)_{0.54}(Al_2O_3)_{0.45}$ pellets heated to **(b)** 1200 ^{o}C, **(c)** 1120 ^{o}C, and **(d)** 1170 ^{o}C for 6h at 10 ^{o}C/min/air in furnace.

XRD studies

XRD was used to confirm the phase composition of all samples. It is important to identify gradual phase changes at different sintering temperatures.

In our XRD data (Figure **5.4**), we observed that zirconia undergoes phase transformation from tetragonal to monoclinic between 1120 ^{o}C and 1125 ^{o}C. However, we are able to make fully dense ceramic nanocomposites at 1120 ^{o}C while retaining the t-zirconia phase. We also wanted to confirm the phase of alumina for potential ZTA composites. Due to peak intensity differences between the relatively high Z zirconia and low Z alumina, spot by spot XRD in specific 2θ (^{o}) regions was performed to identify the alumina phase in the 1120 ^{o}C sample (Figure **5.5**). By comparison with the (012), (113) and (116) peaks of α-alumina standard (PDF#:71-1124), we found that α-alumina is the main alumina phase in these fully dense nanocomposites at 1120 ^{o}C.

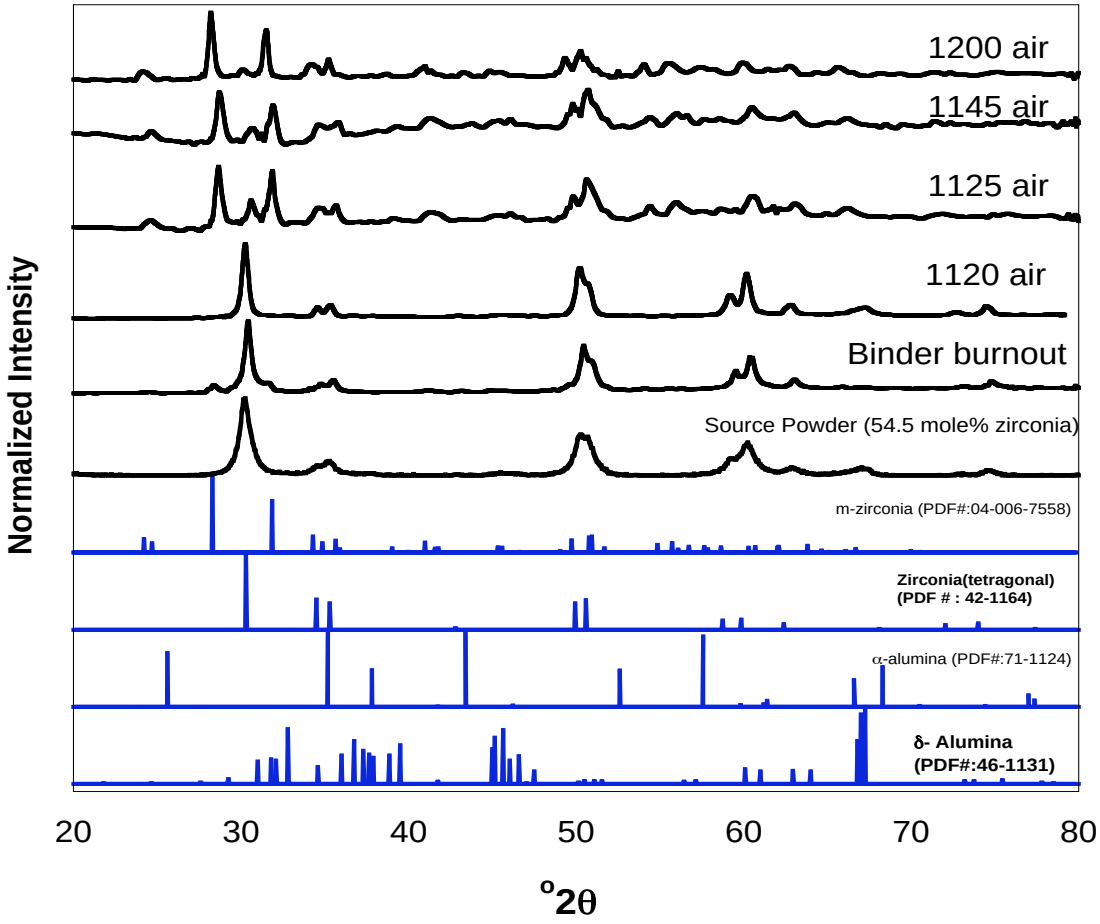

Figure 5.4. XRDs of the source powder and pellets under different heating temperatures

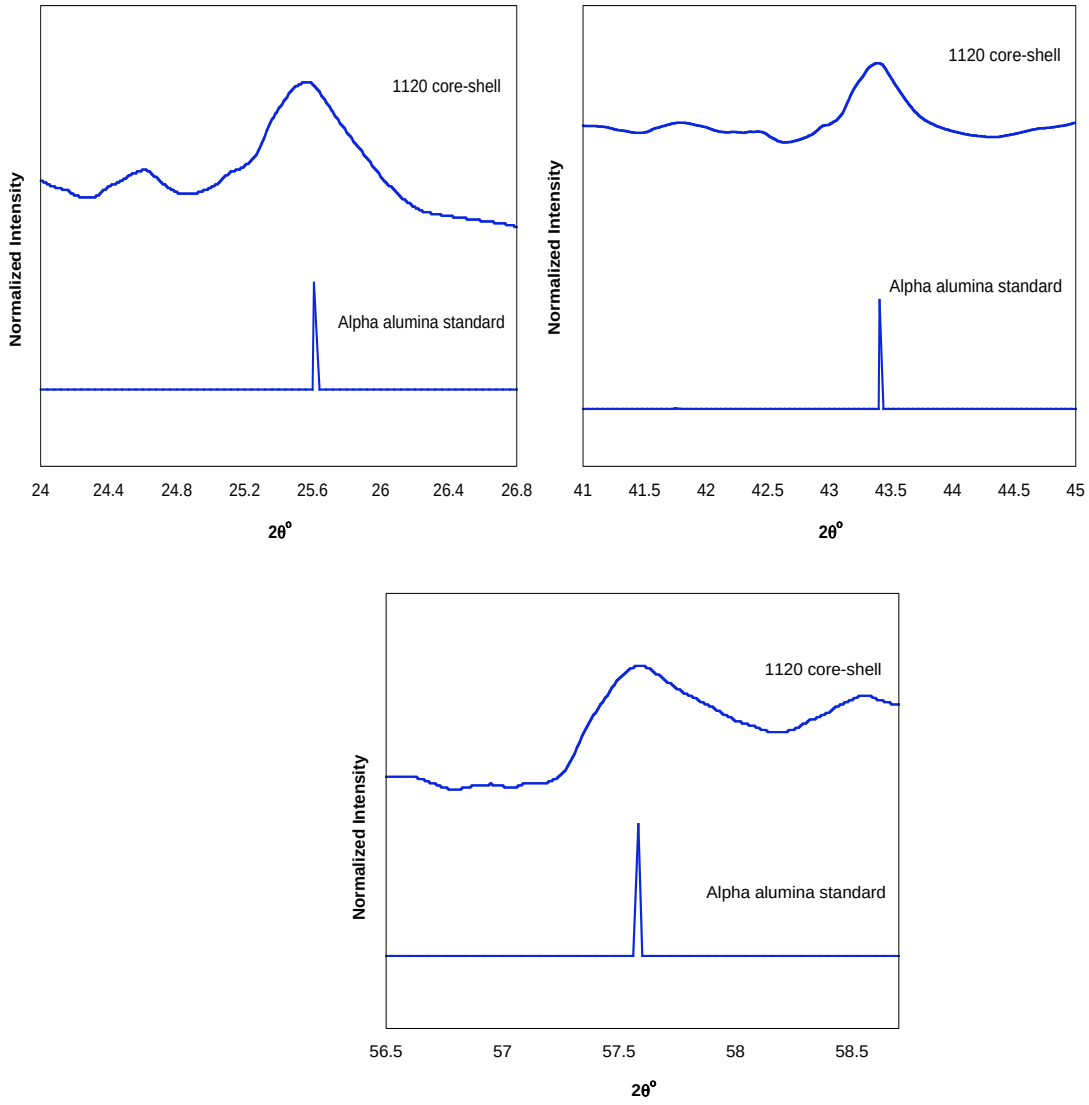

Figure 5.5. Spot by spot XRD of pellet heated to 1120 ^{o}C.

Comparison between core-shell and mixed oxides source

Since we achieved fully dense $(ZrO_2)_{0.54}(Al_2O_3)_{0.45}$ nanocomposite from our core-shell source Zr-Al-O powders, here we try to use separate source nanopowders of t-zirconia and δ-alumina by LF-FSP for fully dense nanocomposite. We did same procedure of green body preparation and sintering for these mixed oxides source case.

According to the XRD data (Figure **5.4**), mixed oxides source indicate monoclinc phase of zirconia. We presume that the effect of alumina on the zirconia phase transformation from tetragonal to monoclinc is not valid in this mixed oxides case, so zirconia is already converted to monoclinc below 1120 ^{o}C.

We also found that the relative density of this mixed oxides product is about 0.89. Microstructure of mixed oxides source composites (Figure **5.7**) also indicate final product is not a dense nanocomposite.

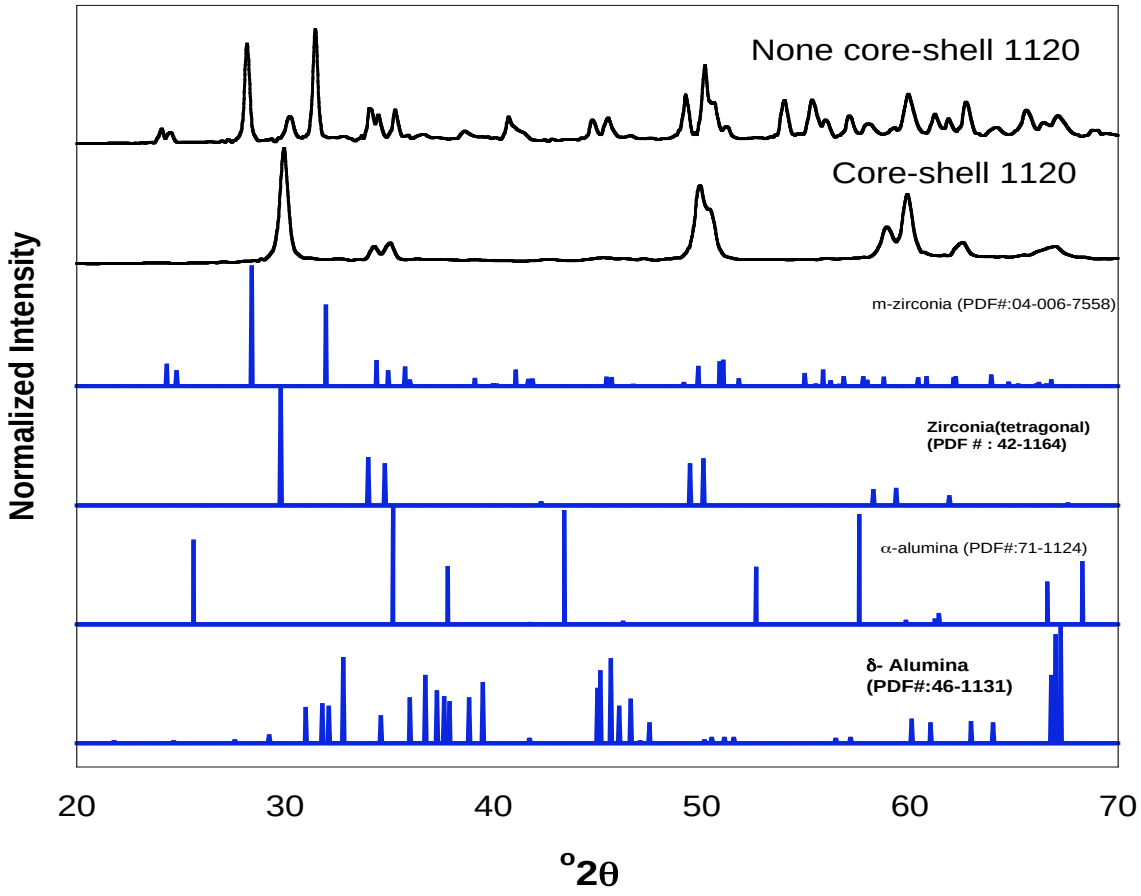

Figure 5.6. XRD patterns of core-shell pellet and none-core-shell pellet heated to 1120 ^{o}C

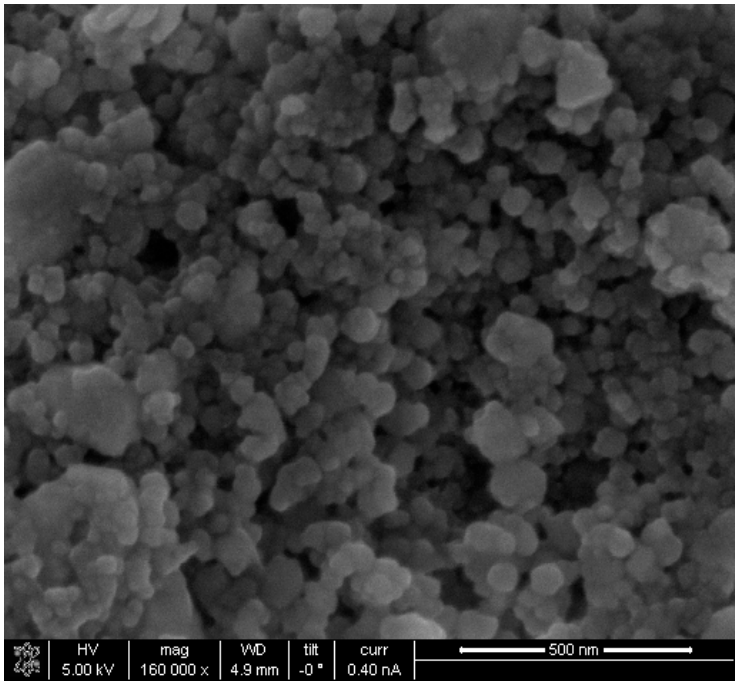

Figure 5.7. Microstructure of none-core shell source Zr-Al-O nanocomposites

Phase transformation toughening

In many cases, the tetragonal phase of zirconia is metastable. If sufficient amounts of metastable tetragonal ZrO_2 are present, then an applied stress, magnified by the stress concentration at a crack tip, can cause the tetragonal phase to convert to the monoclinic phase, with the associated volume expansion. This phase transformation puts the crack into compression, retarding its growth, and enhancing the fracture toughness.[14-16,24,25] This phenomenon is known as transformation toughening, and significantly extends the reliability and lifetime of ZTA products.[14-18,24,25]

Since tetragonal zirconia was found in our fully dense nanocomposites, here we tried to estimate the potential for phase transformation toughening. Stresses were applied by hand grinding with pestle toward our 1120 ^{o}C sintered sample, and then XRD patterns at different times were recorded as seen in Figure **5.7**. Right after fracture of 1120 ^{o}C sample, we ground fractured sample with a pestle, and recorded the XRDs at 1, 5, 10 minutes. XRDs both before and right after fracture show dominant tetragonal zirconia. However, the amount of monoclinic zirconia increases with increases in grinding time. After 10 minutes of grinding, the weight % of monoclinic phase in total zirconia is close

to 50 %. Based on this result, our ceramic nanocomposite including metastable tetragonal phase can be a good candidate for enhanced ZTA materials with high fracture toughness.

As noted above, most current ZTA composites contain up to 30 wt % (26 mole%, 24 vol. %) partially stabilized t-zirconia. In contrast, our fully dense ZTA composites have nearly 60 wt % (54 mole %, 42 vol.%) t-zirconia. Most reported ZTA composites including maximum 30 wt % (26 mole%, 24 vol. %) partially stabilized zirconia show the final densities less than 96% and micron size grains. In contrast, our fully dense ZTA composites including 60 wt % (54 mole %, 42 vol.%) zirconia with grains < 200 nm can be expected to have improved fractured toughness by the increase in zirconia volume fraction (up to 42 vol. %) for potential structural applications.

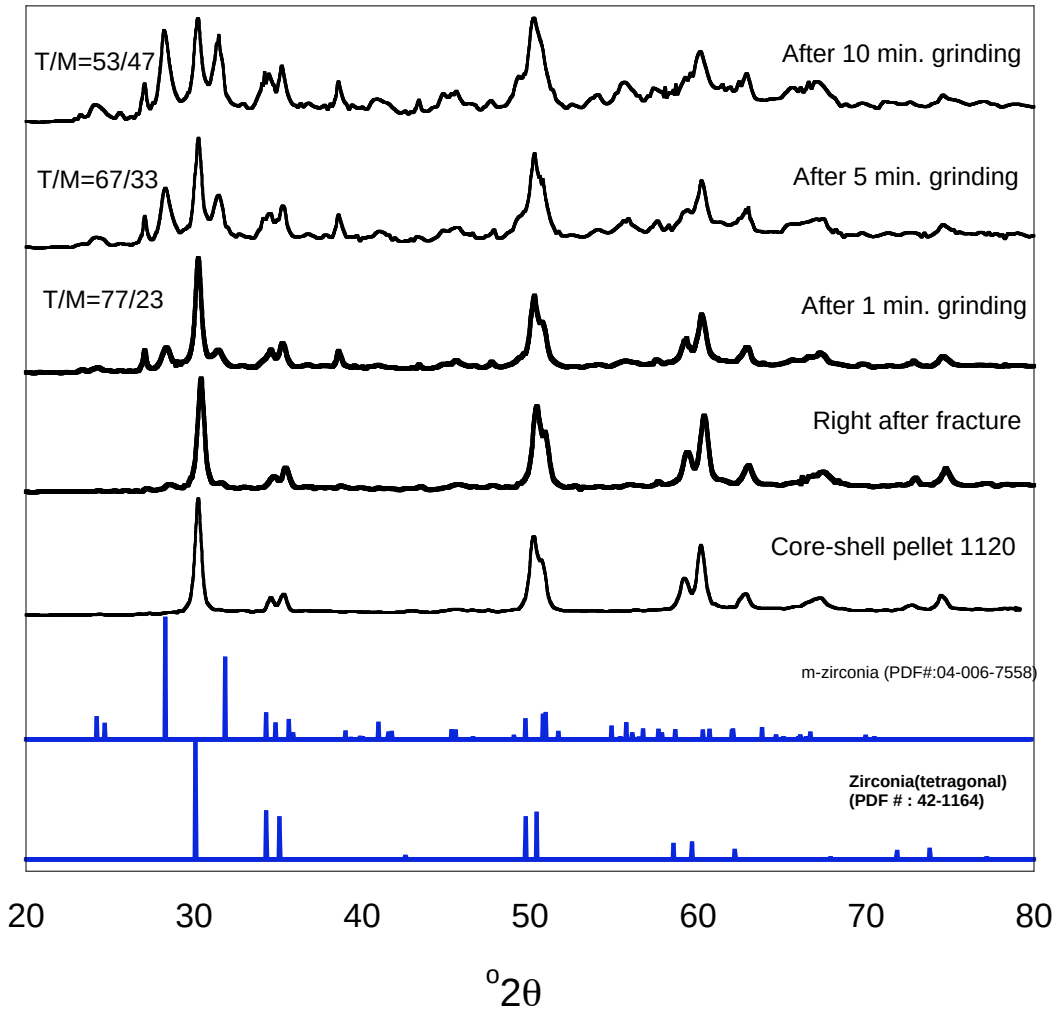

Figure 5.8. XRD patterns of pellet heated to 1120 °C and ground pellets along time changes. T/M= wt % tetragonal phase in zirconia/wt % tetragonal phase in zirconia

5.3 Conclusions

In this study, we were able to produce fully dense ZTA nanocomposites with 99% densities from our $(ZrO_2)_{0.54}(Al_2O_3)_{0.45}$ core-shell nanostructured nanopowders made by LF-FSP. Final ZTA nanocomposites with grain sizes < 200 nm were made using pressureless sintering in air at < 1150 ^oC. Partially stabilized t-zirconia without yttria was retained and the formation of α-alumina was observed after sintering at < 1150 ^oC. We are also able to control the t to m phase transformation of nano zirconia without yttria offering the potential to obtain phase transformation toughening.

We expect our fully dense nanostructured ZTA nanocomposites to offer quality strength, fracture toughness, thermal shock resistance, and thus potential for structural and especially biomedical applications.

In future papers we will discuss the sintering behavior of $(Zr/CeO_x)_x(Al_2O_3)_{1-x}$ core-shell nanopowders by LF-FSP.

5.4 References

1. T. Hinklin, B. Toury, C. Gervais, F. Babonneau, J. J. Gislason, R. W. Morton, R. M. Laine, "Liquid-feed flame spray pyrolysis of metalloorganic and inorganic alumina sources in the production of nanoalumina powders," *Chem. Mater*. **16**, 21-30 (2004).

2. S. Kim, J. J. Gislason, R.W. Morton, X. Q. Pan, H. P. Sun, R. M. Laine, "Liquid-feed flame spray pyrolysis of nanopowders in the alumina-titania System," *Chem. Mater*. **16**, 2336-2343 (2004).

3. J. A. Azurdia, J. Marchal, P. Shea, H. Sun, X. Q. Pan, R. M. Laine, " Liquid-feed flame spray pyrolysis as a method of producing mixed-metal oxide nanopowders of potential interest as catalytic materials. Nanopowders along the $NiO\text{-}Al_2O_3$ tie line including $(NiO)_{0.22}(Al_2O_3)_{0.78}$, a new inverse spinel composition," *Chem. Mater.* **18** (2006) 731-739

4. J. A. Azurdia, J. Marchal, R. M. Laine, " Synthesis and characterization of mixed-metal oxide nanopowders along the CoO_x–Al_2O_3 tie line using liquid-feed flame spray pyrolysis," *J. Am. Ceram. Soc.*, 89 [9] 2749–2756 (2006)

5. M. Kim, T. R. Hinklin, R. M. Laine, "Core-shell nanostructure nanopowders along $(CeO_x)_x(Al_2O_3)_{1-x}$ tie-line by liquid-feed flame spray pyrolysis (LF-FSP)" submitted to *Chem. Mater.* (2008).

6. M. Kim. R. M. Laine, "Liquid-feed flame spray pyrolysis (LF-FSP) for combinatorial processing of nanooxide powders along the $(ZrO_2)_{1-x}(Al_2O_3)_x$ tie-line. Phase segregation and the formation of core-shell nanoparticles," *J. Cer. Proc. Res. **8** 129-136* (2007).

7. P. Zhu, Z. Lin, G. Chen, I. Kiyohiko, "The predictions and applications of fatigue lifetime in alumina and zirconia ceramics," *Int. J. Fat.* **26** 1109-1114 (2004)

8. A. Dakskobler, T. Kosmac "The preparation and properties of Al_2O_3-ZrO_2 composites with corrugated microstructures," *J. Europ. Ceram. Soc.* **24** 3351-3357 (2004)

9. M. Szutkowska, "Fracture toughness behavior of alumina-zirconia composites," J. Mater. Proc. Tech. **153-154** 868-874 (2004)

10. CRC handbook of chemistry and physics. 80th ed.**1999-2000**. CRC press

11. http://www.accuratus.com/

12. http://www.goodfellow.com/

13. X. Guo "Property degradation of tetragonal zirconia induced by low-temperature defect reaction with water molecules," Chem. Mater. **16** 3988-3994 (2004)

14. G. Magnani, A. Brillante, " Effect of the composition and sintering process on mechanical properties and residual stresses in zirconia-alumina composites," *J. Europ. Ceram. Soc.* **25** 3383-3392 (2005)

15. J. Zarate, H. Juarez, M. E. Contreras, R. Perez "Experimental design and results from the preparation of precursory powders of $ZrO_2(3\%Y_2O_3)/(10\text{-}95)\%Al_2O_3$ composites," Pow. Tech. **159** 135-141 (2005)

16. S. T. Aruna, K. S. Rajam, " Mixture of fuels approach for the solution combustion synthesis of Al_2O_3-ZrO_2 nanocomposites," *Mater. Res. Bull*. **39** 157-167 (2004)

17. S. Bhaduri, S .B. Bhaduri, E. Zhou, "Auto ignition synthesis and consolidation of Al_2O_3-ZrO_2 nano/nano composite powders," *J. Mater. Res.* **13(1)** 156- 165 (1998)

18. D. Casellas, M. M. Nagl, L. Llanes, M. Anglada, "Fracture tougness of alumina and ZTA ceramics," J. Mater. Proc. Tech. **143-144** pp.148-152 (2003)

19. J. Freim, J. Mckittrick, "Modeling and fabrication of fine-grain alumina-zirconia composites produced from nanocrystalline precursors," *J. Am. Ceram. Soc*. **81[7]** 1773-1780 (1998)

20. F. F. Lange "Transformation toughened ZrO2: Correlations between grain size control and composition in the system ZrO_2-Y_2O_3," *J. Am. Ceram. Soc*. **69[3]** 240-242 (1986)

21. R. J. Hannick, P. M. Kelly, B. C. Muddle "Transformation toughening in zirconia-containing ceramics," *J. Am. Ceram. Soc*. **83[3]** 461-487 (2000)

22. A. Suresh, M. J. Mayo, W. D. Porter, C. J. Rawn, " Crystallite and grain-size-dependent phase transformations in yttria-doped zirconia," *J. Am. Ceram. Soc*. **86[2]** 360-362 (2003)

23. A. Bravo-Leon, Y. Morikawa, M. Kawahara, M. J. Mayo, "Fracture toughness of nanocrystalline tetragonal zirconia with low yttria content," *Acta Materialia* **50** pp.4555-4562 (2002)

24. W. H. Tuan, R. Z. Chen, T. C. Wang, C. H. Cheng, P. S. Kuo, "Mechanical properties of Al_2O_3/ZrO_2 composites," *J. Europ. Ceram. Soc.* **22** 2827-2833 (2002)

25. D. Jayaseelan, T. Nishikawa, H. Awaji, F .D. Gnanam, "Pressureless sintering of sol-gel derived alumina-zirconia composites," *Mater. Sci. Eng.* **A256** 265-270 (1998)

26. H. Yoshida, S. Hashimoto, T. Yamamoto, "Dopant effect on grain boundary diffusivity in polycrystalline alumina," *Acta Materialia* **53** pp.433-440 (2005)

27. J. Gopaul, W. C. Maskell, K. E. Pitt, " Planar oxygen sensor Part I: Effect of crazing of a zirconia crack on an alumina substrate," *J. Appl. Electrochem*. **29** 93-100 (1999)

28. I-W. Chen, X-H. Wang, "Sintering dense nanocrystalline ceramics without final-stage grain growth," Nature **404** 168-171 (2000)

29. J. L. Shi " Solid-state sintering of ceramics: pore microstructure models, densification equations and applications," *J. Mater. Sci.* **34** 3801-3812 (1999)

30. R.S. Averback, H .J. Hofler, R. Tao, " Processing of nano-grained ceramics," *Mater. Sci. Eng.* **A166** 169-177 (1993)

31. P-L. Chen, I-W-.Chen, " Sintering of fine oxides: II, Sintering mechanisms," *J. Am. Ceram. Soc*. **80[3]** 637-645 (1997)

CHAPTER 6

SYNTHESIS OF NANOPOWDERS ALONG THE ZnO-Al_2O_3 TIE-LINE

6.1 Abstract

Liquid-feed flame spray pyrolysis of mixtures of alumatrane [$Al(OCH_2CH_2)_3N$]/zinc acetate dihydrate [$Zn(O_2CCH_3)_2 \bullet 2(H_2O)$] or zinc propionate [$Zn(O_2CCH_2CH_3)_2$]/aluminum acetylacetonate [$Al(Acac)_3$] dissolved in EtOH in known molar ratios can be used to combinatorially generate nanopowders along the ZnO-Al_2O_3 tie-line. LF-FSP of $(ZnO)_x(Al_2O_3)_{1-x}$ powders with x = 0 to 1.0 were produced and characterized by XRD, SEM, TEM, FTIR, TGA, DTA and BET. The resulting powders had average particle sizes (APSs) <100 nm with the majority being < 50 nm.

Analytical data suggest that at concentrations of interest for transparent conducting oxides, < 10 mole % Al_2O_3 the particle morphologies are combinations of plates and rods that grow with c/a ratios close to 1.

The spinel phase dominates at $(ZnO)_x(Al_2O_3)_{1-x}$ x=0.5 and 0.7, which differs from the currently accepted phase diagram for the ZnO-Al_2O_3 couple where phase separation between spinel and α-alumina should be observed at the same composition. It appears that the rapid quenching during LF-FSP helps preserving spinel phase at ambient temperature as new, kinetic products of $(ZnO)_x(Al_2O_3)_{1-x}$ nanopowders. Finally, the solubility of ZnO in Al_2O_3 and vice versa in the materials produced by LF-FSP suggest apparent flame temperatures reached before quenching are 1700°-1800°C.

6.2 Introduction

Transparent conducting oxides or TCOs are used for a wide variety of applications including various display applications as well as photovoltaic, electrochromic, RF shielding and sensor applications. TCOs typically have band gaps > 3.1 eV (absorptions < 400 nm) and can have conductivities of ≈ 1 x 10^4 Scm^{-1} similar to good metal conductors.[1-10] Although functionally useful TCOs have been made from a wide variety of alloys or doped forms of In_2O_3, SnO_2, Ga_2O_3, ZnO, PbO_2, SbO_2; the commercial material of choice is doped indium oxide, e.g. In_2O_3:Sn 5-6 at% Sn (ITO). Unfortunately, ITO is expensive because of the scarcity of In. Thus, extensive efforts have been made to find substitutes that provide similar properties at lower costs.

Aluminum doped zinc oxide or ZnO:Al was first proposed as an ITO substitute by Wasa et al[1] in 1971,[11] and has since been the subject of numerous studies, typically in thin films prepared using a variety of deposition methods.[12-16] One key issue is the thermal stability of ZnO which loses oxygen at temperatures ≥150°C.[17] In 1984, Minami et al. described the preparation of ZnO:Al films stable to ≈ 400°C with resistivities of ≈ 2 x 10^{-4} Ω cm.[17-19] ZnO:Al films have recently been used in commercial flat panel displays and thin film solar cells offering resistivities of 1-3 x 10^{-4} Ω cm at dopant concentrations of 1.6-3.2 at% Al in ZnO.[11-19] Considerable opportunity remains to further modify these materials to improve conductivity, thermal stability and transparency through further manipulation of both chemical and phase composition as well as processing methods motivate the efforts reported here.[19]

We have previously demonstrated that liquid-feed flame spray pyrolysis (LF-FSP) offers a simple way to produce complex mixed-metal oxide nanopowders.[20-35] Furthermore, we recently demonstrated that LF-FSP processing of MgO-, CuO-, CoO-, ZrO-, CeO-, NiO-Al_2O_3 mixed-metal systems provides access to heretofore unknown and/or unusual spinel phases because of the rapid quench kinetics that occur in the process.[28-34] Given that some of these materials and phases may offer unique properties inaccessible using standard ceramics processing methods, we sought to extend LF-FSP processing to $(ZnO)_x(Al_2O_3)_{1-x}$ nanopowders hopefully with similar outcomes. The current studies also serve as the basis for LF-FSP processing of $(ZnO)_x(Al_2O_3)_{1-x}$ nanopowders incorporating tertiary and/or quaternary dopants.

Three phases are found along the ZnO-Al_2O_3 tie-line; ZnO zincite, $ZnAl_2O_4$ spinel, and Al_2O_3 alumina. Based on these phases, a set of compositions was targeted for LF-FSP processing focusing on two main regions of Al_2O_3 doped ZnO [$(ZnO)_x(Al_2O_3)_{1-x}$, x = 0.9-1.0] and middle compositions including the spinel phase region [$(ZnO)_x(Al_2O_3)_{1-x}$, x = 0.3-0.5].

The Table **6.1** series of LF-FSP $(ZnO)_x(Al_2O_3)_{1-x}$ nanopowders was produced at rates of 30-50 g/h using EtOH as the solvent and fuel. The as-prepared powders were characterized by XRD, TEM, BET, FTIR, TGA-DTA, and chemical analysis.

6.3 Experimental

Materials

Zinc nitrate [$Zn(NO_3)_2 \cdot x(H_20)$, 99%] and zinc acetate dihydrate dihydrate [$(CH_3COO)_2Zn \cdot 2H_2O$, 99.9%] were purchased from Aldrich (Milwaukee, WI). Triethanolamine $N(CH_2CH_2OH)_3$, anhydrous ethanol [CH_3CH_2OH, 99$^+$%], and methanol were purchased from Alfa Aesar. Aluminum tris(sec-butoxide), [$Al(OsBu)_3$, 97%] was purchased from Chattem Chemical Co. Aluminum acetylacetonate [$Al(C_5H_7O_2)_3$, 99.9%] was purchased from Mackenzie company (Bush, LA). All compounds and solvents were used as received.

Precursor preparation and pyrolysis.

Zinc propionate: $Zn(O_2CCH_2CH_3)_2$

Zinc Nitrate [$Zn(NO_3)_2 \cdot x(H_20)$, 99%, 100 g, mole] was reacted with excess propionic acid (400 mL, 5.44 mole) in a 1 L flask equipped with a still head and an addition funnel. N_2 was sparged directly through the solution (2 psi pressure) as the solution was heated at 120 ˚C/2h to distill off ~150 mL of liquid (water and propionic acid). The resulting solution was slowly heated to distill off excess solvent and reactant. Thereafter, the solution was reduced to 100 mL of a viscous green gel by rotary evaporation, and then the gel was dried to a solid under a dynamic vacuum at 70 °C. The TGA of this product is discussed in the Results and Discussion section.

Alumatrane $Al[N(CH_2CH_2O)_3]$ was synthesized from $Al(OsBu)_3$ and $N(CH_2CH_2OH)_3$ as described elsewhere,[20,23] then diluted with EtOH such that the ceramic yield was 7.5 wt % by TGA.

$(ZnO)_x(Al_2O_3)_{1-x}$ A series of precursors corresponding to specific $(ZnO)_x(Al_2O_3)_{1-x}$ (x = 0 to 1.0) powder compositions were prepared. For ZnO rich composition series, alumatrane was used as the source of Al_2O_3 and zinc acetate methanolic solution for ZnO. For the whole ZnO-Al_2O_3 tie-line compositions, we used aluminum acetylacetonate [$Al(Acac)_3$] as the source of Al_2O_3 and $Zn(O_2CCH_2CH_3)_2$ for ZnO, because zinc acetate was only slightly soluble in alcohol solvents.

Measured volumes of the two solutions, based on the molar ratio of Zn and Al, were mixed in the appropriate amounts to make 500 ml solutions for each precursor

compositions listed in Table **6.1** in the Results and Discussion section, and then 2500 ml of EtOH was added to give a final volume of 3000 ml with stirring at room temperature.

Liquid-feed flame spray pyrolysis (LF-FSP)

LF-FSP, as developed at the University of Michigan, has been described in detail in published papers.[20-35] Briefly, alcohol (typically EtOH) solutions containing 1-10 wt % loading of ceramic as precursors, e.g. single- or mixed-metal alkoxides, carboxylates or β-diketonates are aerosolized with O_2 into a 1.5 m long quartz chamber where it is ignited with methane pilot torches.

Initial combustion temperatures run 1500°-2000°C, depending on the processing conditions, generating nanopowder "soot." Temperatures drop to 300-500 °C over 1.5 meters, equivalent to a 1000°C quench in ≤ 100 msec leading to kinetic products and nanopowders that are largely unaggregated; although they are lightly agglomerated. "Shooting" rates can be 200 g/h when using wire-in-tube electrostatic precipitators operating at 10 kV. Typical powders are 15 to 100 nm APS with specific surface areas (SSAs) of 30 to 100 m^2/g. When combinations of elements are used, the resulting nanopowders will have compositions identical to those of the precursor solutions. Since compositions of chemical solutions can be changed intentionally, potentially even during mixing just before aerosolization, it becomes possible to combinatorially produce mixed-metal oxide materials. Hence it becomes possible to rapidly optimize materials for given properties or for ease of processing.

Characterization

Thermal gravimetric analysis and differential thermal analysis (TGA-DTA)

Phase transformations and mass loss events occurring during heating of as-prepared samples were investigated by Simultaneous Differential Thermal (SDT) Analyzer (TA Instruments, Inc., New Castle, DE). The transformation temperatures were determined by themogravimetric analysis (TGA) were also done using a model 2960 Simultaneous Thermogravimetric Analyzer.

As-prepared powders of about 20 mg were hand pressed in a 3 mm dual action die and placed inside Pt sample cups and heated at ramp rates of 10˚C/min from room temperature to 1400˚C. The reference material was a pellet of α-alumina. A synthetic air

flow of 50 ml/min was maintained during all SDT experiments. Precursor samples were placed in alumina sample cups with an empty alumina cup as the reference and heated at ramp rates of 10°C/min up to 1000°C.

X-ray diffraction analysis (XRD) As-prepared and heat-treated (air/nitrogen) samples were characterized using a Rigaku Rotating Anode Goniometer. Powder samples for the Rigaku were prepared by placing ≈ 100 mg in XRD sample holders (amorphous silica slides) for data collection. Cu Kα (λ = 1.54 Å) radiation with a Ni filter was used with a working voltage and current of 40 kV and 100 mA, respectively. Scans were continuous from 10–80° 2θ with a step scan of 2° 2θ/min and increments of 0.05° 2θ. Peak positions and relative intensities were characterized by comparison with PDF files for zincite (ZnO), normal spinel ($ZnAl_2O_4$), non-stoichiometry spinel [$(Zn_{0.3}Al_{0.7})Al_{1.7}O_4$], and δ-$Al_2O_3$, (36-1451), (05-0669), (77-0732), and (42-1215) respectively.

Specific surface area (SSA)

SSA was measured on a Micromeritics ASAP 2000 sorption analyzer. Samples (200 mg) were degassed at 400°C until the outgas rate was 5 mmHg/min. Analyses was run at 77K with N_2. SSAs were determined by the BET multipoint method using at least five data points with relative pressures of 0.001-0.20. The average particle size was derived using the formula $< R >= \frac{3}{\rho \times SSA}$ where <R> = average particle size in diameter, and ρ is the density of the material.

Transmission Electron Microscopy (TEM)

An analytical high resolution TEM (Model 3011, JOEL, Osaka, Japan) was used to measure the particle sizes and morphologies of as-prepared powders. Powder samples were prepared by dipping a holey carbon grid in a vial of emulsion with as-prepared powder. The specimen was held in a Gatan double tilt goniometer. An operating voltage of 300 kV was used.

Scanning electron microscopy (SEM).

A high resolution SEM (FEI NOVA Dual beam focused ion beam workstation and scanning electron microscope) was used to image powder morphologies. Powder samples were dispersed in distilled H_2O using an ultrasonic horn (Vibra-cell, Sonics and

Materials, Inc., Newton, CT). A drop of the dispersed powder/water was placed on an aluminum SEM stub and allowed to dry for 4 h on a hot plate. Powders were sputter coated with 1-5 nm of Au-Pd to reduce charging effects. The operating voltage was 15.0 kV.

6.4 Results and discussion

The objectives of the current study were to develop structure-property-processing parameters for LF-FSP production of $(ZnO)_x(Al_2O_3)_{1-x}$ oxide nanopowders along the $ZnO\text{-}Al_2O_3$ tie-line including spinel ($ZnAl_2O_4$) composition regions as listed in Table **6.1**. Details of the LF-FSP process are given in the experimental.

The mixed-metal precursors are mutually soluble in alcohol allowing any composition of the two to be aerosolized and combusted using LF-FSP process. Therefore, LF-FSP offers access to high specific surface area (SSA) nanopowders consisting of single-phase, solid solutions and mixed-phase nanopowders in the $(ZnO)_x(Al_2O_3)_{1-x}$ oxide system.

Below, we first discuss what is known about the $ZnO\text{-}Al_2O_3$ phase diagram, and then discuss the types of powders made and their specific characteristics.

The $ZnO\text{-}Al_2O_3$ phase diagram was first described by Bunting[36] in 1932 but does not incorporate ZnO:Al solid solutions (up to 5 mol% Al_2O_3 depending on the synthesis temperature) and off-stoichiometric spinel phases. Hansson et al[37] recently revised the phase diagram, adding two solid solution regions to Bunting's work. First, the maximum solubility of Al_2O_3 in zincite was found to be 4.7 mole% at 1695°C and was found to decrease rapidly with decreasing temperatures to ≤ 0.5 mole% at 1550°C and below. The spinel composition is reported as the mineral gahnite ($ZnAl_2O_4$) when Al_2O_3 is in equilibrium with zincite ZnO. [37]

LF-FSP flame synthesis occurs at temperatures of 1500°-2000°C, thus we are potentially able to explore the solubility limit of Al in ZnO at much higher temperatures than possible for standard ceramics processing methods and by virtue of the rapid quenching that occurs in LF-FSP, produce powders with relatively extreme compositions, e.g. at the edge of the currently known solubility limits.

However, nanopowders produced by LF-FSP show higher solubility (up to 20 mole% Al_2O_3) at ZnO rich compositions than the phase diagram.[37] As with many of our previous studies, LF-FSP materials generated by rapid quenching lead to novel kinetic products not expected based on traditional processing methods. Since traditional processing methods lead to thermodynamically rather than kinetically defined phase compositions, these materials may offer unique opportunities for a wide variety of

application including various display applications and/or photovoltaic, electrochromic, RF shielding and sensor applications.

Compositions

The set of compositions listed in Table **6.1** were produced using LF-FSP. First, We made ZnO rich composition sample from zinc acetate and alumatrane, then the overall compositions series with zinc propionate and aluminium acetylacetonate.

Table 6.1. Selected $(ZnO)_x(Al_2O_3)_{1-x}$ nanopowder compositions produced by LF-FSP

From zinc acetate and alumatrane

Sample	Mole % of Al_2O_3	Mole % of ZnO
95 mole% ZnO	5	95
97.5 mole% ZnO	2.5	97.5
99 mole% ZnO	1	99
99.5 mole% ZnO	0.5	99.5
99.8 mole% ZnO	0.3	99.8
100 mole% ZnO	0	100

From zinc propionate and aluminium acetylacetonate

Sample	Mole % of Al_2O_3	Mole % of ZnO
10 mole% ZnO	90	10
30 mole% ZnO	70	30
50 mole% ZnO	50	50
80 mole% ZnO	20	80
95 mole% ZnO	5	95
99 mole% ZnO	1	99

Precursor and precursor formation

We previously reported the characterization of alumatrane $[N(CH_2CH_2O)_3Al]$ and its use as a precursor in LF-FSP for the synthesis of δ-alumina nanopowders.[23,25,30-35] Here we report on the zirconium precursor, $Zn(O_2CCH_2CH_3)_2$ synthesized as discussed in the experimental section. This precursor has a thermal decomposition pattern similar to other metal carboxylate precursors studied previously.[30-34]

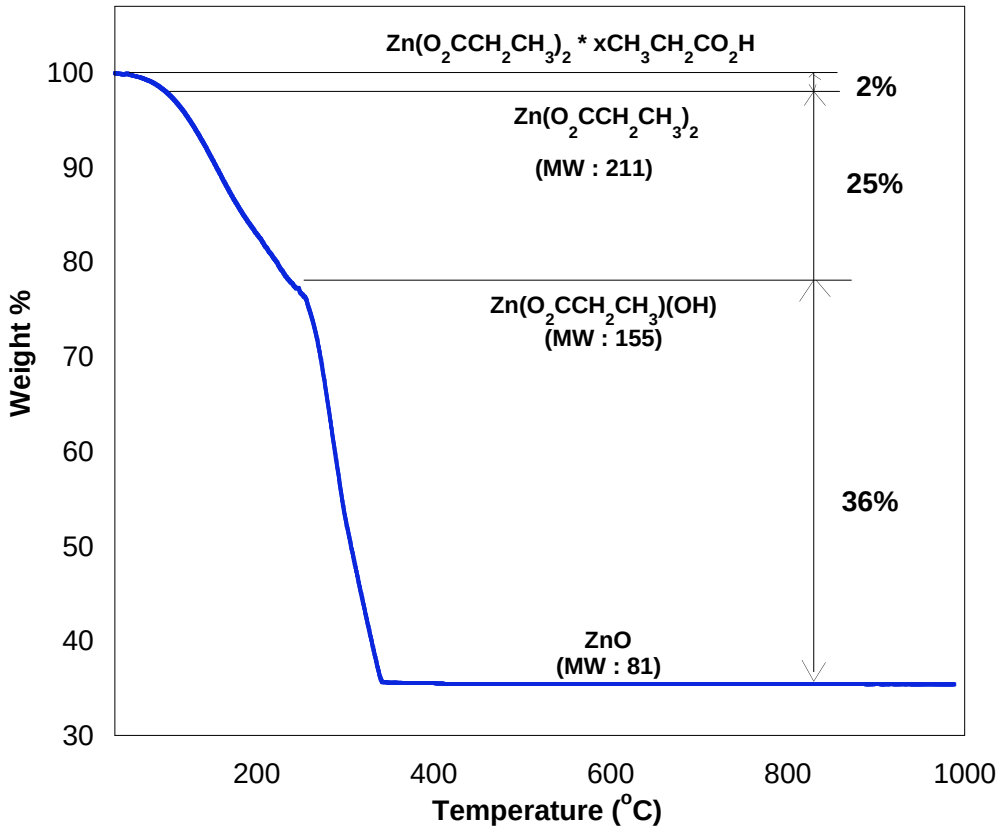

Figure 6.1. TGA of $Zn(O_2CCH_2CH_3)_2$ ramped at 10^oC/min in synthetic air.

Figure **6.1** shows a TGA trace for $Zn(O_2CCH_2CH_3)_2$. Initial mass losses (2%) are due to propionic acid of recrystallization. Thereafter, mass loss events are attributed to the decomposition of the propionate ligands as reaction suggested in reaction (1),(2). [23,25,30-35]

$$Zn(O_2CCH_2CH_3)_2 \rightarrow Zn(O_2CCH_2CH_3)(OH) + CH_3CH{=}C{=}O \qquad (1)$$

Calc. (Found) Mass Loss = 26.0 % (25.0%)

$$Zn(CH_3CH_2COO)(OH) \rightarrow ZnO + H_2O + CH_3CH{=}C{=}O \qquad (2)$$

Calc. (Found) Mass Loss = 34.4 % (35.0 %)

Final ceramic yields [37% (ZnO)] are within experimental error of the calculated value (37.6 %) from the decomposition of the precursor [$Zn(O_2CCH_2CH_3)_2$] to the oxide (ZnO) and are as expected based on previous studies. [23,25,30-35]

XRD studies

Here we begin with the ZnO rich samples from zinc acetate and alumatrane, which form Al-doped zincite nanopowders. The XRDs for the majority of the compositions are given in Figure **6.2**. 100 mole% ZnO (pure ZnO) has the hexagonal wurtzite structure in accord with PDF[36-1451]. The XRDs of the 95-100 mole at% ZnO compositions show that hexagonal zincite is the major phase. However, small (440) peaks at 65.2° 2θ seen in the XRD support spinel phase formation for compositions 97.5 and 95 mole% ZnO.

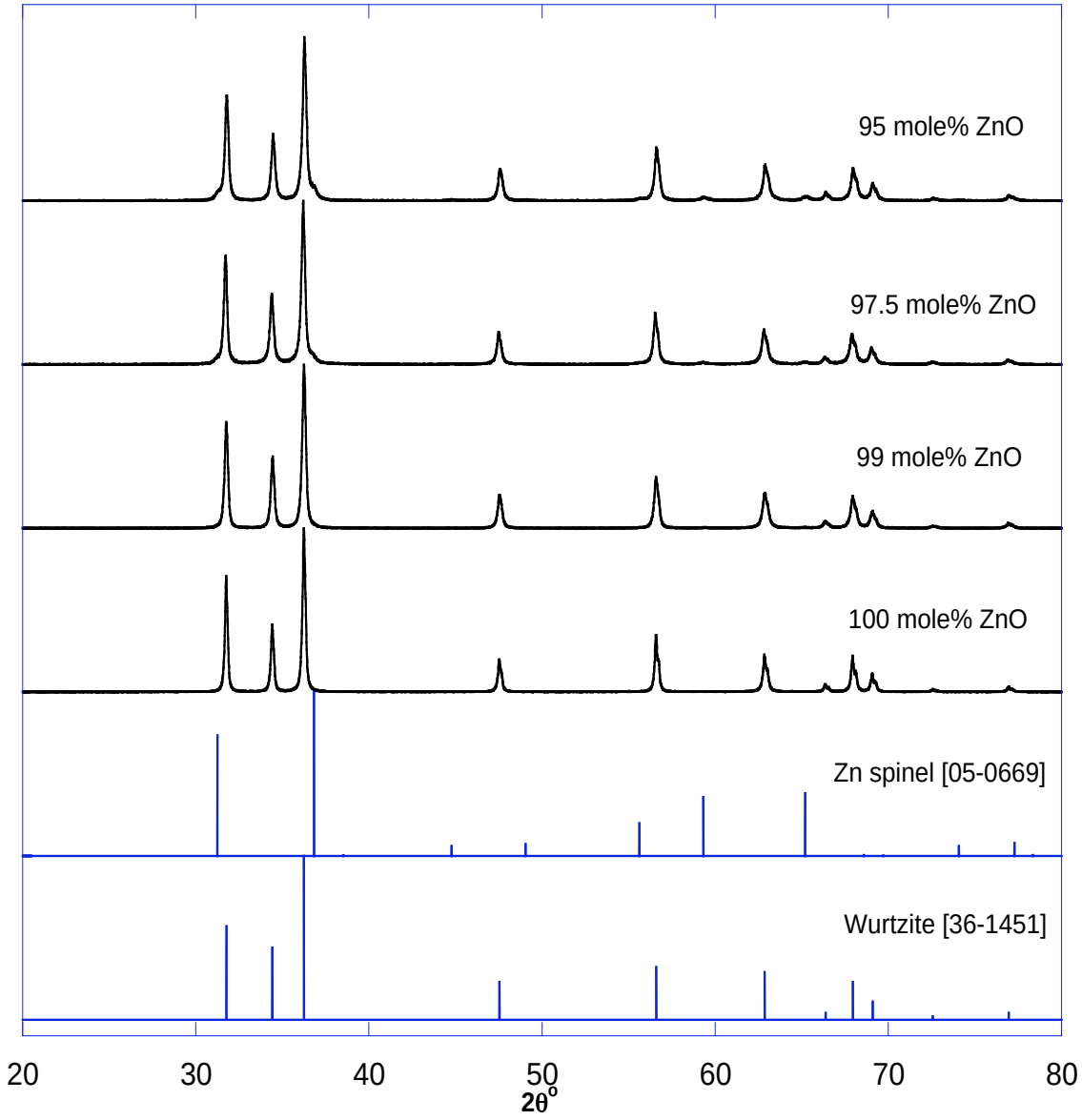

Figure 6.2. XRD patterns of $(ZnO)_x(Al_2O_3)_{1-x}$ nanopowders from zinc acetate and alumatrane

For overall compositions including the spinel phase region, we used zinc propionate $Zn(O_2CCH_2CH_3)_2$ and aluminum acetylacetonate [$Al(Acac)_3$], because zinc acetate is only slightly soluble in alcohol solvents. Figure **6.3** provides XRD patterns for all as-produced nanopowders along the $(ZnO)_x(Al_2O_3)_{1-x}$ tie-line.

In Figure **6.3**, the zinc-rich samples (99, 95 mole % ZnO) show only wurtzite (PDF #: 36-1451). For 80 mole% ZnO, wurtzite is the main phase, but traces of spinel $ZnAl_2O_4$ are also observed as a weak (440) peak appears at 65.2° 2θ supporting spinel phase formation.

For samples with 30 and 50 mole % ZnO, $ZnAl_2O_4$ spinel is observed as the main phase. The formation of 100% spinel phase at 50 mole % ZnO is expected.[37] However, the 30 mole % ZnO sample is also phase pure spinel in contrast to existing thermodynamic data where phase separation between spinel and α-alumina should be found. In the phase diagram, phase pure spinel with a 30 mole% ZnO composition forms only between 1700 and 1800 °C. One could argue that in LF-FSP, phase pure spinel forms and the spinel structure is preserved by rapid quenching to ambient temperature, forming a kinetic product.

Thus, we can suggest that the effective LF-FSP operating temperature is 1700°-1800°C. The term "effective" is used because we are not able to estimate the effect(s) of the very small particle sizes and therefore high surface energies on the solubility of one oxide phase in the other.

The 10 mole% ZnO sample shows phase separation between spinel and δ-alumina; different from the phase diagram where phase separation should lead to spinel and α-alumina. According to Hinklin et, al., [23] the formation of δ-alumina might be favored during LF-FSP processing. One can argue that kinetic transition alumina formed during LF-FSP were not able transform to thermodynamically stable α alumina, because of rapid quenching (1000 ^{o}C/millisec).

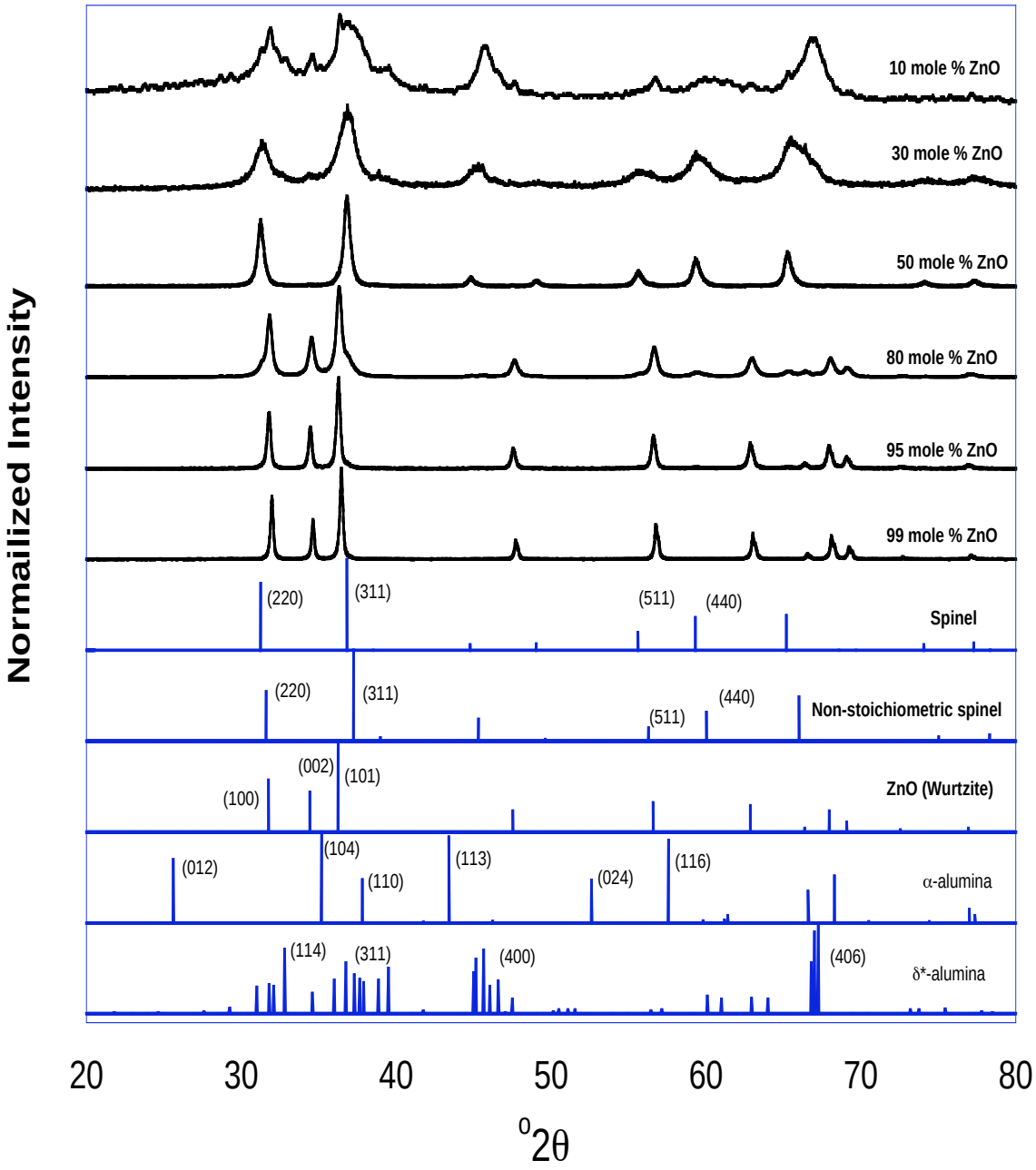

Figure 6.3. XRD powder patterns of as-processed $(ZnO)_x(Al_2O_3)_{1-x}$ nanopowders by LF-FSP. Wurtzite ZnO (PDF file: 36-1451), Spinel $ZnAl_2O_4$ (PDF file: 05-0669), Non-stoichiometric spinel $(Zn_{0.3}Al_{0.7})Al_{1.7}O_4$ (PDF file: 77-0732), α-alumina (PDF file: 71-1124), δ^*-Al_2O_3 (PDF file: 46-1215),

Average particle sizes (APSs) and specific surface areas (SSAs) from BET

Table **6.2** provides average particle sizes (APSs) of samples from zinc acetate and alumatrane along the different plane directions as measured using Debye-Scherer methods. 100 mole% ZnO (pure ZnO) has the largest APSs of 90-150 nm depending on the crystallographic plane.

Table 6.2. Particle sizes (nm) measured by FMWH of XRD and aspect ratio (c/a).

(hkl)	100 mole% ZnO	99.8 mole% ZnO	99 mole% ZnO	97.5 mole% ZnO	95 mole% ZnO
(100)	134	68	44	39	33
(002)	150	59	41	32	34
(101)	114	54	38	32	29
(102)	100	47	34	30	31
(110)	101	55	36	32	32
(103)	90	41	28	27	27
(112)	88	47	31	27	29
(201)	88	51	34	33	29
Aspect ratio (c/a)	1.12	0.87	0.93	0.82	1.03

The crystallite sizes decrease to ~30 nm for 95 mole% ZnO. XRDs of the (hkl) 100, 002, and 101 reflections of all LF-FSP prepared samples showed no evidence of preferred growth orientations in contrast to reports for sputtered materials with even less Al doping.[13]

Lattice parameters determined using the (100) and (101) peaks (Figure **6.2**) show c/a axis ratios of < 2.0 as listed in Table **6.3**. In Table **6.3**, it can be seen that the *d* spacings of both the a- and c-axes increase when the amount of Al^{3+} increases indicating that the cell volume increase is proportional to the Al^{3+} ion concentrations.

Since the Al^{3+} radius (0.053 nm) is smaller than that of Zn^{2+} (0.075 nm), the expansion of the lattice constants in both directions might be explained in terms of the incorporation of Al^{3+} ions in interstitial sites,[38,39] not by substitution of Zn^{2+} by Al^{3+}. If Al^{3+}ions were to substitute for Zn^{2+}, one would expect that the total cell volume decrease. However, the 95 mole % ZnO cell volume is lower than that for 99.8 mole % ZnO, which indicates that the concentration of Al ions is above the solubility limit in ZnO at this composition (Maximum is 4.7 mole % per Hanssen et. al).[37] The maximum cell volume is found for 97.5 mole % ZnO. For 99.8, 99.0 and 97.5 ZnO mole % compositions, we find Al^{3+} dissolved in ZnO likely due to the rapid quenching during the LF-FSP process.

Table 6.3. Lattice parameters measured by XRD using (100) and (101) peaks.

	100 mole% ZnO	99.8 mole% ZnO	99 mole% ZnO	97.5 mole% ZnO	95 mole% ZnO
a	3.2442	3.2506	3.2508	3.2532	3.2490
c	5.1900	5.2084	5.2068	5.2128	5.2022
Cell volume	94.6	95.3	95.3	95.6	95.1

The APSs for samples from zinc propionate and aluminium acetylacetonate were estimated from Debye-Scherer line broadening and their SSAs (Table **6.4**). Both methods give very similar results. The APSs are 15 ± 5 nm.

Table 6.4. APSs and SSAs of $(ZnO)_x(Al_2O_3)_{1-x}$ nanopowders

Sample ZnO Mole %	XRD line broadening Particle size (nm)	BET-derived Particle size (nm)	SSA (m^2/g)
99	16	18	30
95	14	16	33
80	13	15	39
50	13	13	50
30	12	11	59
10	12	11	63

Scanning and transmission electron microscopy

High resolution microscopy was used to assess particle morphologies as a function of chemical and phase composition. SEMs of the 100, 97.5 and 95 mole% ZnO samples made from zinc acetate and alumatrane are shown in Figure **6.4**. Pure ZnO (ZA00) powders consist of hexagonal rods and platelets. The addition of small amounts of alumina in the 97.5 and 95 mole% ZnO powders results in significant reductions in average particle sizes (APSs) from the pure ZnO powders. This APS reduction in the SEM images matches with the APS data from XRD line broadening in previous section. However, particles >100 nm are still seen in both samples.

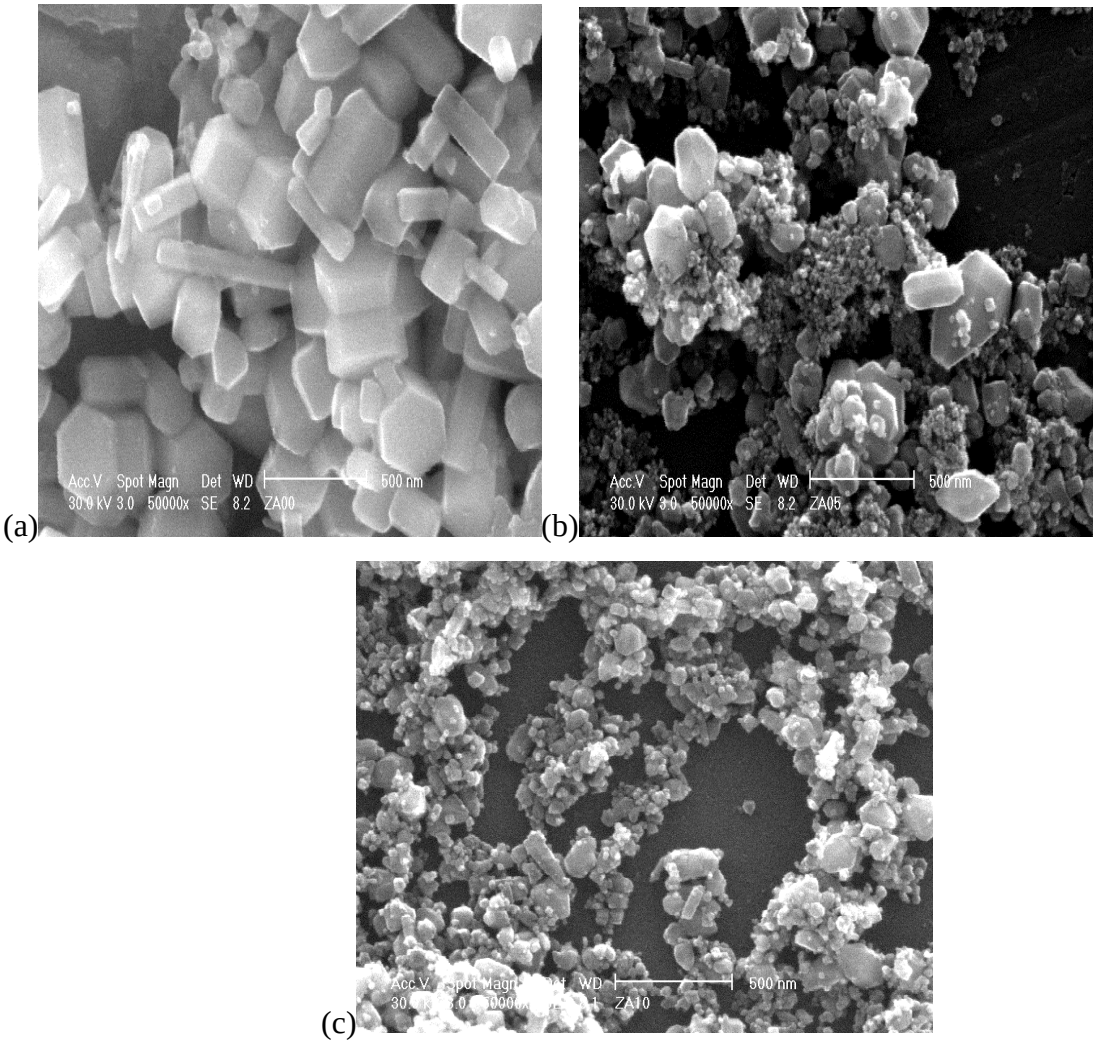

Figure 6.4. SEM micrographs of as-prepared nanopowders made from zinc acetate and alumatrane. (a) 100 (b) 97.5 and (c) 95 mole % ZnO samples

SEM was also used to demonstrate powder uniformity for the samples from zinc propionate and aluminium acetylacetonate. Figure **6.5** shows that SEM resolution is insufficient to reveal individual particles but does provide a view of the general particle population.

For ZnO rich sample (Figure **6.5a**) shows dominant cylindrical shape particles with irregular c/a ratio, and bimodal distribution of APSs. For spinel region sample (Figure **6.5b**), most particles are spherical and APSs are less than 50nm. These SEMs indicate that the particle populations produced here do not include any obvious micron size particles.

(a) 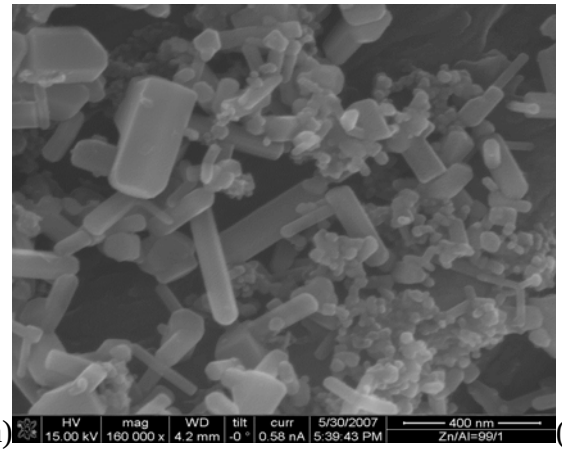

(b) 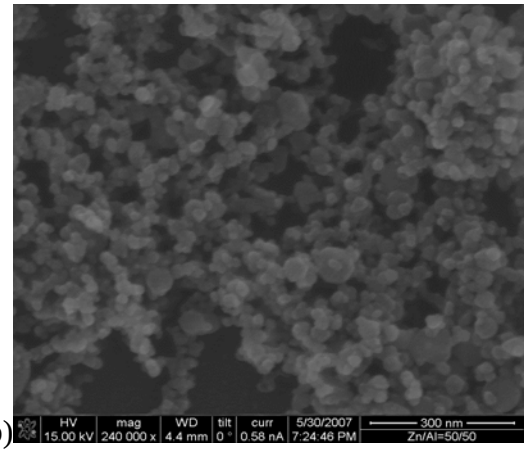

Figure 6.5. SEM images of (a) 99 mole% ZnO with Al_2O_3. (b) 50 mole% ZnO in Al_2O_3.

TEM micrographs of 100, 99.8 and 95 mole% ZnO samples are shown in Figure **6.6**. While small particles (< 15 nm in particle sizes) are not observed in pure ZnO powders, the 99.8 mole% ZnO powders show significant amounts of fine particles with APSs < 30 nm compared to the pure ZnO powders.

(a) 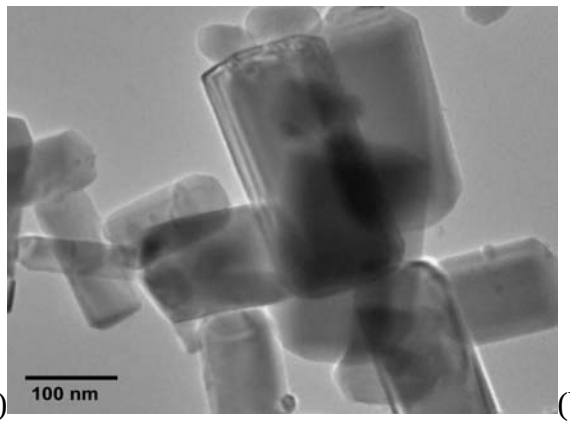

(b) 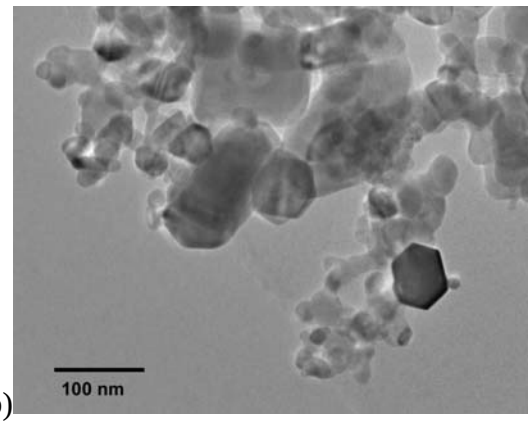

(c) 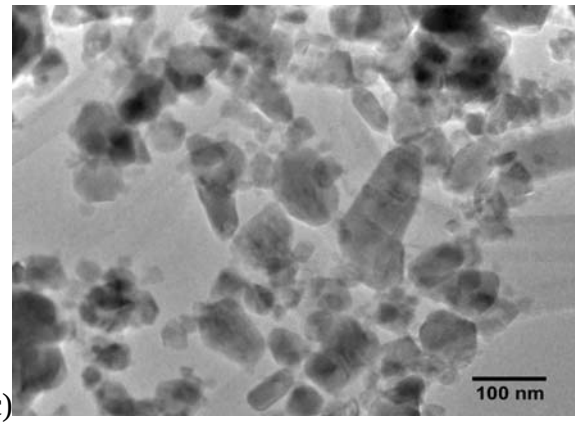

Figure 6.6. TEM micrographs of as-prepared powders.(a) 100 (b) 99.8 and (c) 95 mole% ZnO

The increase of small sized particles in 99.8 and 95 mole% ZnO samples also matches with XRD line broadening results and SEM images. It appears that there is a bimodal size distribution at 25 nm and 250 nm in these powders, while the compositions close to the spinel region (see below) show more uniform and smaller APSs. The morphologies also change with Al^{3+} doping. As the amount of Al increases, the resulting particles tend toward rods indicating enhanced growth along the c-axis perhaps indicating somewhat selective addition of Al^{3+} ions to one growth face. However, detailed studies that correlate particle size and shape as a function of Al^{3+} content were not pursued further.

TEM images were also used to gather information on particle morphologies and sizes of as-prepared powders at the spinel composition. Discussions of actual size/size distributions are not appropriate if based solely on TEM micrographs, unless combined with the XRD results and SEM images. Figure **6.7** offers high-resolution TEM images of $(ZnO)_x(Al_2O_3)_{1-x}$ nanopowders from LF-FSP. Particle sizes here are typically below 30 nm in diameter with the vast majority < 20 nm. Figure **6.7a** shows clear unidirectional lattice planes (d= 2.4 Å of (311) planes, cubic spinel phase). The d spacing value from TEM images confirms our previous XRD results of spinel phase at 50 mole% ZnO composition. Multi-faceted single particle is likely a consequence of particle formation during rapid quench from the gas phase.

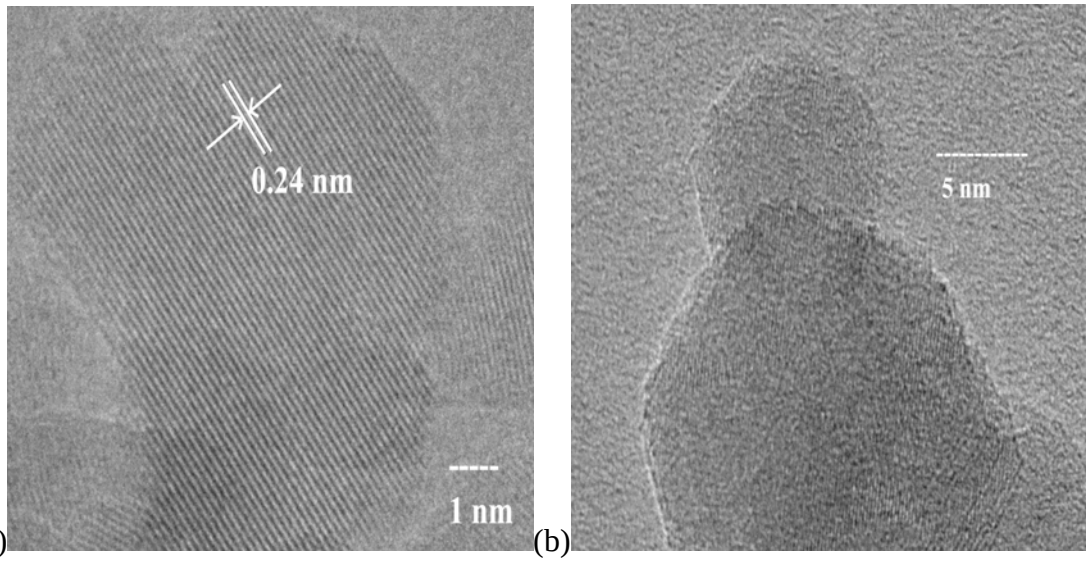

(a) (b)

Figure 6.7. TEM images of (a) 50 mole% ZnO in Al_2O_3. (b) 30 mole% ZnO in Al_2O_3.

Diffuse reflectance infrared Fourier transform spectroscopy (DRIFTS).

Once the particle morphologies were characterized by XRD and high-resolution microscopy, the particle surface chemistries were characterized using FTIR. DRIFT spectra for $(ZnO)_x(Al_2O_3)_{1-x}$ nanopowders are presented in Figure **6.8**. Higher wavenumber (>1500 cm^{-1}) regions were first normalized and then multiplied 10x in an effort to observe νC-H or νO-H bands on powder surfaces. These spectra offer little evidence for either νC-H or νO-H bands.

The as-processed nanopowders have no significant organic species on the surface, as the absence at 2900-2700 cm^{-1} νC-H vibrations suggests.[40] νO-H vibrations (3800-3200 cm^{-1}) show both chemi- and physi-sorbed water on the surface of nanopowders.[41]

νM-O bands are observed in the 1200-400 cm^{-1} region. The spinel structure (80, 50 and 30 mole % ZnO) is confirmed by FTIR spectra, as there are three characteristic peaks at 510, 570, and 690 cm^{-1} corresponding to a normal spinel structure with octahedrally coordinated Al^{3+}.[42,43] The bands at 450-600 cm^{-1} show νZn-O bands typical of the wurtzite structure, which dominate zinc rich samples (95, 99, 80 mole% ZnO).[44,45]

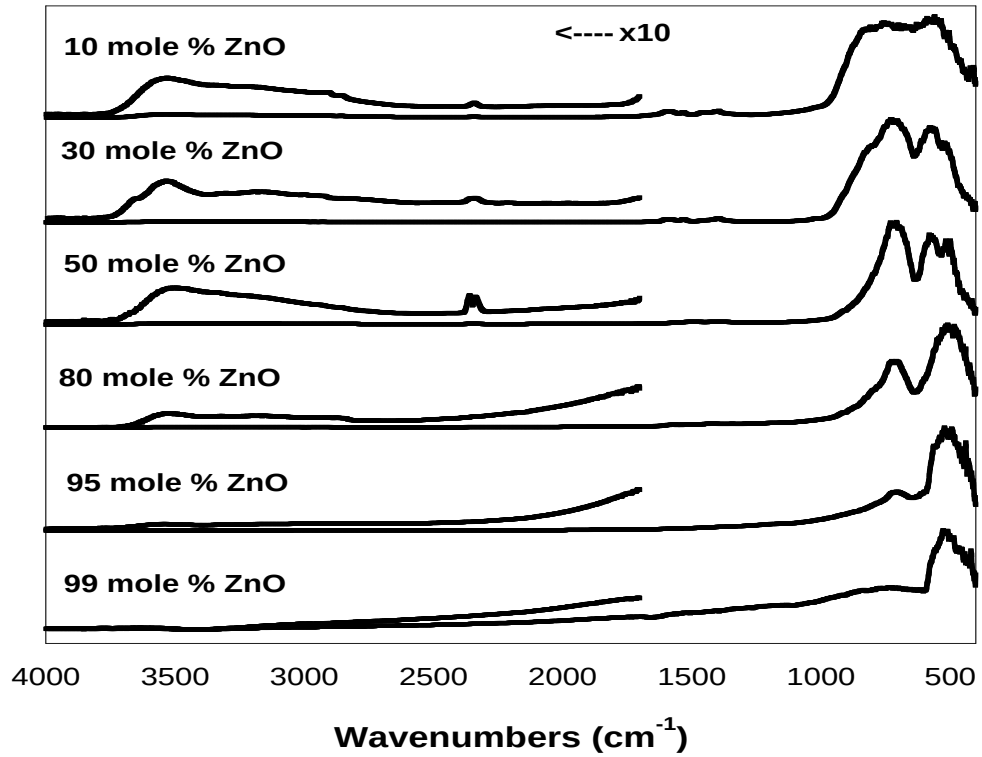

Figure 6.8. DRIFTs of as-processed $(ZnO)_x(Al_2O_3)_{1-x}$ nanopowders.

TGA-DTA studies

Thermal gravimetric analyses (TGA) were performed in air on all as-prepared powder samples to determine the relative amounts of surface species and thermal behaviors, and the thermal stability of the powders was investigated using DTA. Figures **6.9** shows the TGA for the series of powders. The DTAs are not shown, because they are not informative, no phase transformations are observed.

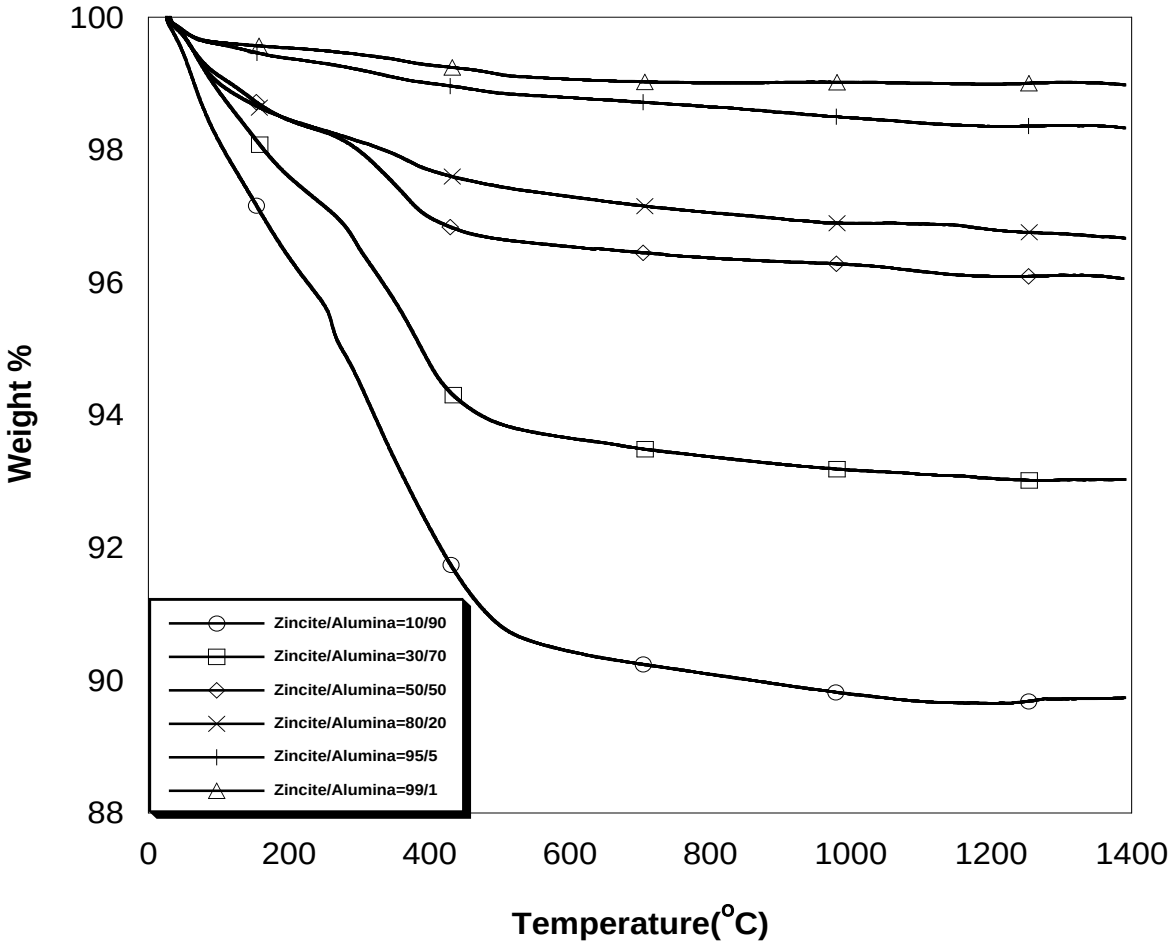

Figure 6.9. TGAs of as-processed $(ZnO)_x(Al_2O_3)_{1-x}$ nanopowders made from zinc propionate and aluminum acetylacetonate (10°C/min, in air).

All as-processed powders exhibit 0.5-5.0 wt% mass-losses up to ≈ 300°C, typical of LF-FSP produced nanopowders, that can be attributed to evolution of both physi- and chemi-sorbed water as seen in the FTIR (Figure **6.8**).[41] Mass losses between 300° and 400 °C are due to elimination of carbonate species as CO_2. The amount of mass loss is proportional to the amount of alumina, same as seen previously.[30-34]

Reprocessing spinel composition nanopowders by LF-FSP

We recently reprocessed δ-alumina using LF-FSP causing δ alumina transform to α alumina.[35] Based on this result, we realized that given that 30 mole% ZnO composition gives pure nonstoichiometric spinel phase (PDF file:77-0732) as a kinetic product, we might expect core-shell nanostructured nanoparticles to form with spinel and α-alumina using LF-FSP reprocessing based on the thermodynamic data at the elevated temperatures and nucleation differences between spinel and α-alumina due to different boiling points.[33-35] Therefore, we reprocessed as-produced spinel composition nanopowders (30 and 50 mole % ZnO), because we expect that as-processed spinel nanoparticles will be separated to spinel and α-alumina during reprocessing. The existing phase diagram suggests that phase separation between spinel and α-alumina should be observed at 30 mole % ZnO composition.

As-produced LF-FSP $(ZnO)_x(Al_2O_3)_{1-x}$ (x=0.3, 0.5) powders (3.0 g) were dispersed with 5 mg DARVAN C-N® (R.T. Vanderbilt company, Inc) in 100 mL EtOH using a 1.2 cm diameter 500 W ultrasonic horn (Sonics and Materials 600 VCX, Newtown, CT) at 40% of full power for 12 h. The dispersion was allowed to settle for 24 h. Dispersed nanopowders were mixed with ethanol to a 3.0 wt% ceramic loading, and reprocessed by LF-FSP as described in experimental section.

We found that the result form reprocseeing is different from what we originally expected. The XRDs (Figure **6.10)** show the phases of the as-produced and re-processed nanopowders at 30 and 50 mole% ZnO compositions. For 50 mole% ZnO samples, phase separation between wurtzite zincite and spinel phase (PDF file: 05-0669) were observed in contrast to the existing thermodynamic data showing phase pure stoichiometric spinel. For 30 mole% ZnO samples, two main phases, wurzite and spinel (PDF file: 05-0669), with traces of α-alumina phase.

Based on the comparison with thermodynamic phase diagram,[37] it appears that phase pure spinel is heated to form separated spinel phase and liquid phase during LF-FSP reprocessing, then spinel portion is quenched to form stoichimetric spinel (PDF file: 05-0669) and liquid portion is quenched to form wurtzite ZnO. Because ZnO sublimes at 1700^oC, Zn^{2+} in liquid portion are expected to become vapors during LF-FSP reprocessing and oxidized to form ZnO during quenching.

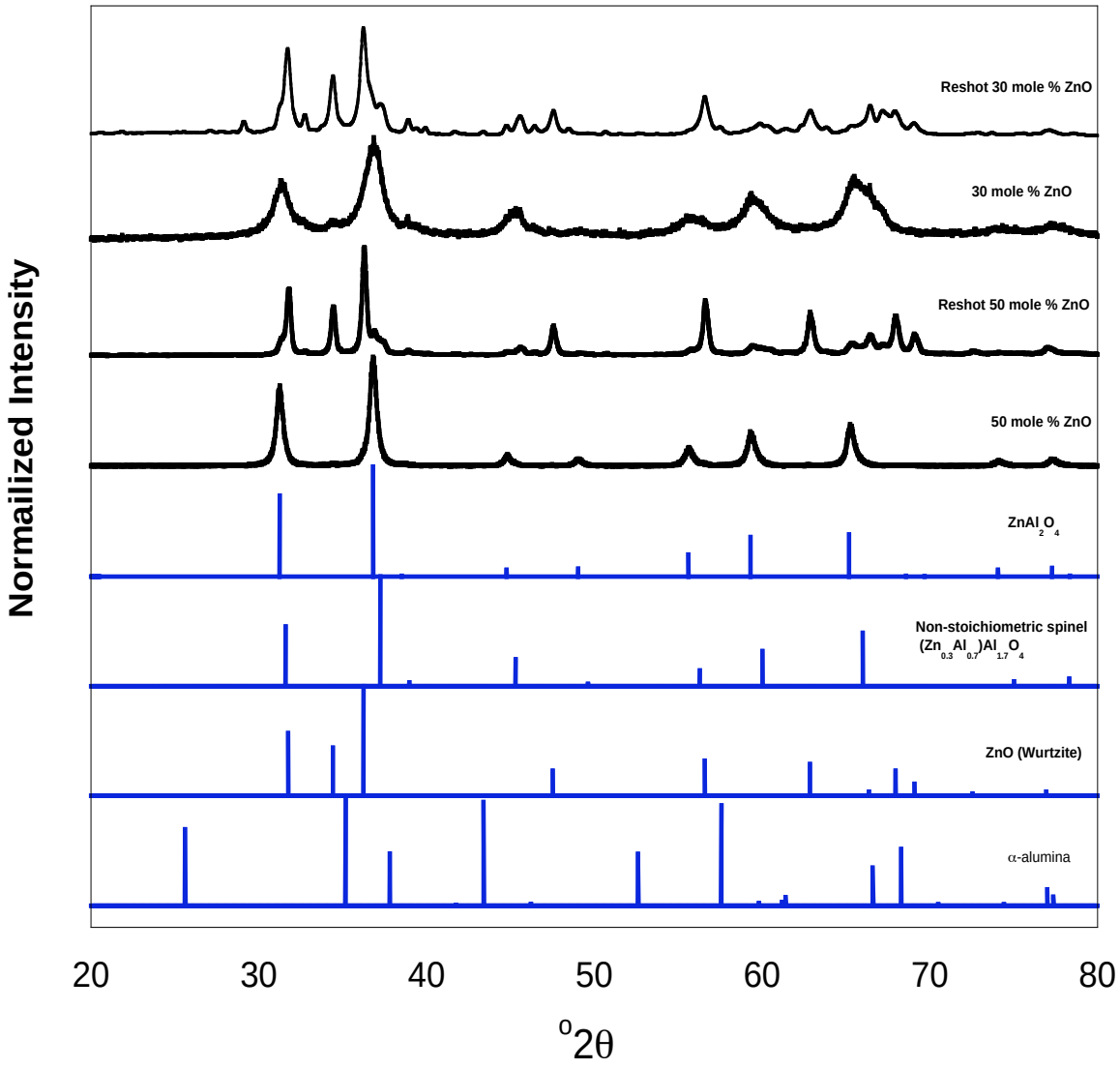

Figure 6.10. XRDs of as-prepared and reprocessed nanopowders of spinel composition.

High resolution SEM was used to study the morphology of re-processed nanopowders. In Figure **6.11**, we observe two different morphologies in the re-processed nanopowders. Comparing with images in previous sections, we expect the cylindrical shape nanoparticles to be zincite and the spherical nanopowders to be spinel.

(a)

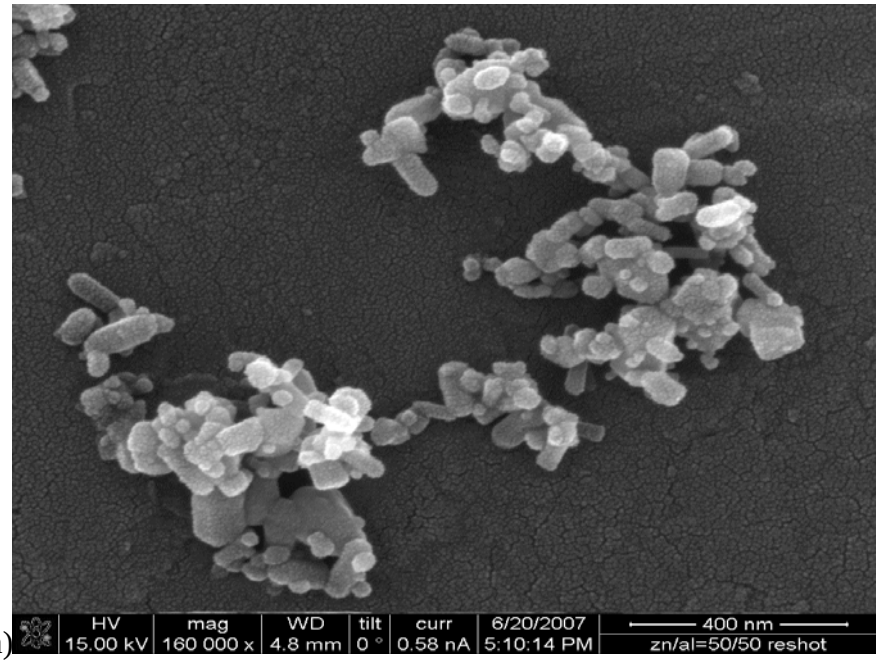

(b)

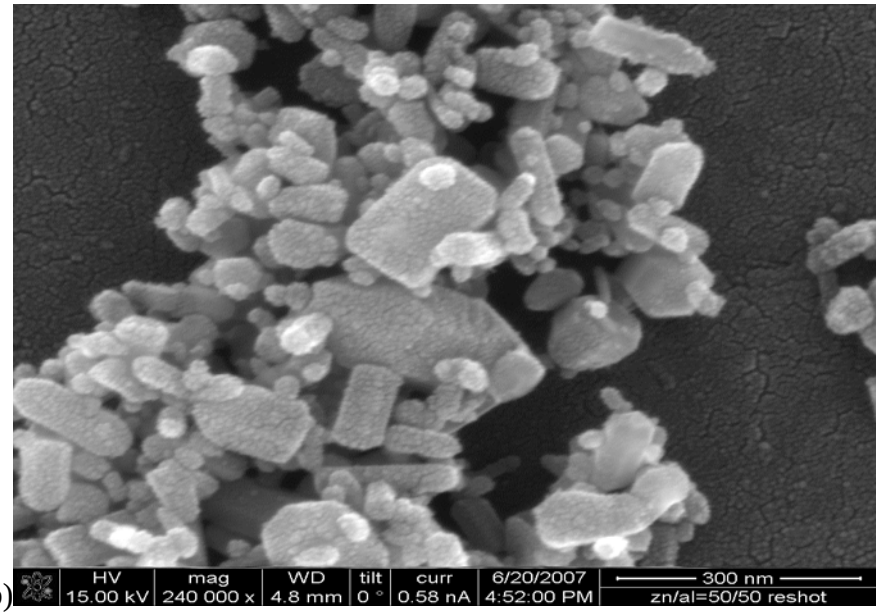

Figure 6.11. SEM images of reprocessed (a), (b) 50 mole% ZnO in Al_2O_3

High resolution TEM was used for studies on the morphology and the crystal structure of re-processed nanopowders. Figure **6.12** images of reprocessed nanopowders also show a mixture of cylindrical and spherical nanoparticles that can be expected to be wurtzite and spinel, bsed on the XRDs. Clear lattice planes in both cylindrical and spherical nanopowders indicate single crystals. Twinning (Figure **6.12a**) might happen

during LF-FSP due to stress caused by quenching. We might expect potential core-shell structure with different flame temperature of LF-FSP.

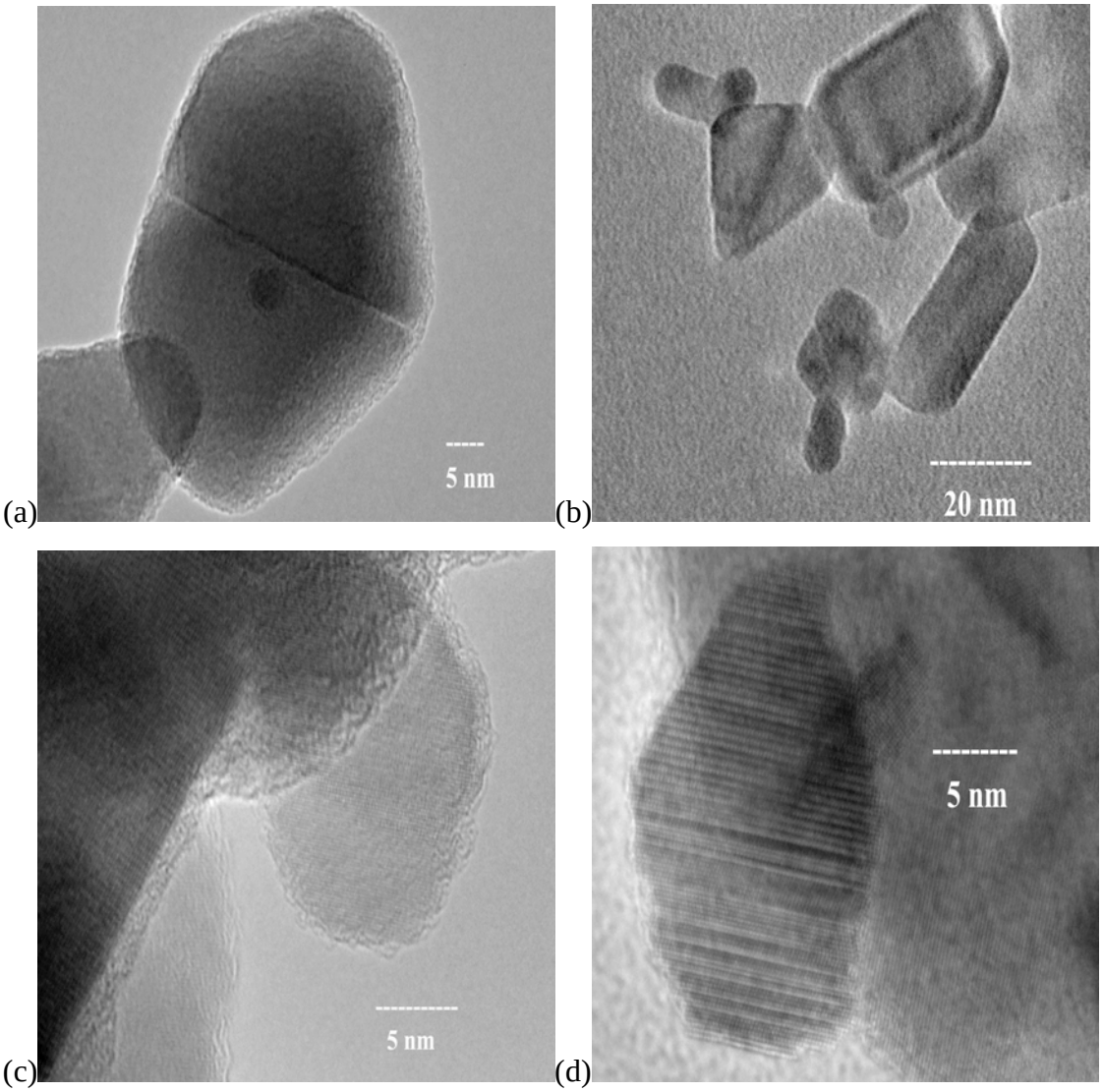

Figure 6.12. TEM images of reprocessed (a),(c) 50 mole% ZnO in Al_2O_3
(b),(d) 30 mole% ZnO in Al_2O_3

6.5 Conclusions

The utility of LF-FSP processing for combinatorial studies of nanopowders along the $(ZnO)_x(Al_2O_3)_{1-x}$ tie line was demonstrated focusing on composition regions including Al-doped ZnO for TCO applications and zinc spinel ($ZnAl_2O_4$). The resulting data is different from the thermodynamic phase diagram, because the resulting nanopowders are kinetic products made by rapid quenching of LF-FSP.

The as-produced powders were characterized in terms of phase, size, composition, and morphology by chemical analysis, FTIR, XRD, SEM, TEM and TGA-DTA. The XRD data support previous conclusions suggesting that Al^{3+} ions incorporate into interstitial site of zincite resulting in octahedrally coordinated Al^{3+}. At 80 mole % ZnO, small amounts of spinel phase segregate, while the XRD results suggest formation of a single zincite phase at zinc-rich compositions of 99, 95 mole % ZnO.

Based on the solubilities of Al_2O_3 in ZnO (up to 20 mole% Al_2O_3) and vice versa, we can suggest an effective operating temperature for LF-FSP processing that ranges between 1700-1800°C in ZnO-Al_2O_3 system from the two compositional regions studied. The term “effective” is used because we are not able to estimate the effect(s) of the very small particle sizes and therefore high surface energies on the solubility of one oxide phase in the other. As noted above, the resulting materials suggest that the ZnO-Al_2O_3 phase diagram may need revision.

Also, reprocessing as-prepared nanopowders of 30 and 50 mole% ZnO samples by LF-FSP cause phase separation from phase pure spinel to spinel and wurtzite in contrast to existing thermodynamic data. We expect this phenomenon from vaporazation of Zn^{2+} ions during LF-FSP process.

6.6 References.

1. H. Hosono, H. Ohta, M. Orita, K. Ueda, M. Hirano, "Frontier of transparent conductive oxide thin films," *Vacuum* **66**, 419-425 (2002).

2. I. Hamberg and C. G. Granqvist, "Evaporated Sn-doped In_2O_3 films: Basic optical properties and applications to energy-efficient windows," *J.Appl. Physics* **60**, R123-R160 (1986).

3. P.P. Edwards, A.Porch, M.O. Jones, D.V. Morgan, R.M. Perks, "Basic materials physics of transparent conducting oxides," *Dalton Trans.* 2995-3002 (2004).

4. H. Hono, "Built-in Nanostructures in Transparent Oxides for Novel Photonic and Electronic Functions Materials," *Int. J. Appl. Ceram. Technol*. **1**, 106-18 (2004).

5. D.S. Ginley, C. Bright, "Transparent conducting oxides," *MRS Bull.* **25**, 15-18 (2000).

6. B.G. Lewis, D.C. Paine, "Applications and processing of transparent conducting oxides," *MRS Bull.* **25**., 22-7 (2000).

7. H.Kawazoe, H. Yanagi, K. Ueda, H. Hosono, "Transparent p-type conducting oxides: Design and fabrication of p-n heterojunctions," *MRS Bull.*, **25**, 28-36 (2000).

8. T. Minami, "New n-type transparent conducting oxides," *MRS Bull.* **25**, 38-44 (2000).

9. R.G. Gordon, "Criteria for choosing transparent conductors," *MRS Bull.* **25**, 52-7 (2000).

10. T.J. Coutts, D.L. Young, X. Li, "Characterization of Transparent Conducting Oxides" *MRS Bull.*, **25**, 58-65 (2000).

11. K. Wasa, S. Hayakawa, and T. Hada, "Electrical and Optical Properties of Sputtered *n-p* ZnO-Si Heterojunctions" *Jpn. J. Appl. Phys.* **10**, 1732 (1971).

12. Z. Jin, I. Hamberg, and C.G. Granqvist, "Optical properties of sputter-deposited ZnO:Al thin films"*J. Appl. Phys.* **64**, 5117 (1988).

13. M.J. Alam and D.C Cameron, "Preparation and properties of transparent conductive aluminum-doped zinc oxide thin films by sol–gel process"*J. Vac. Sci. Technol. Sect. A* **19**, 1642 (2001).

14. T. Schuler and M.A. Aegerter, "Optical, electrical and structural properties of sol gel ZnO:Al coatings*" Thin Solid Films* **351**, 125-31 (1999).

15. S. H. Jeong, J. W. Lee, S. B. Lee and J. H. Boo, "Deposition of aluminum-doped zinc oxide films by RF magnetron sputtering and study of their structural, electrical and optical properties," *Thin Solid Films* 435, 78-82 (2003).

16. T. Suchiya, T. Emoto, and T. Sei, "Preparation and properties of transparent conductive thin films by the sol-gel process" *J. Non-Cryst. Solids* **178**, 327-32 (1994).

17. T. Minami, H. Nanto, S. Shooji, and S. Takata, "The stability of zinc oxide transparent electrodes fabricated by R.F. magnetron sputtering" *Thin Solid Films* **111**, 167 (1984).

18. T. Minami, H. Nanto, S. Shooji, and S. Takata, *Jpn. J. Appl. Phys., Part 2: Lett.* **24** p.L781 (1985).

19. T. Minami, "New n-type transparent conducting oxides," *MRS Bull.* **25** 38-44 (2000).

20. C.R. Bickmore, K.F. Waldner, D.R. Treadwell, R.M. Laine, "Ultrafine Spinel Powders by Flame Spray Pyrolysis of a Magnesium Aluminum Double Alkoxide," *J. Am. Ceram. Soc.* **79**, 1419-23 (1996).

21. C.R. Bickmore, K.F. Waldner, R. Baranwal, T. Hinklin, D.R. Treadwell, R.M. Laine, "Ultrafine Titania by Flame Spray Pyrolysis of a Titanatrane Complex: Part I," *J. Europ. Ceram. Soc.* **18**, 287-97 (1998).

22. A.C. Sutorik, S.S. Neo, T. Hinklin, R. Baranwal, D.R. Treadwell, R.Narayanan, R.M. Laine, "Synthesis of Ultrafine β"-Alumina Powders via Flame Spray Pyrolysis of Polymeric Precursors," *J. Am. Ceram. Soc*. **81**, 1477-86 (1998).

23. T. Hinklin, B. Toury, C. Gervais, F. Babonneau, J.J. Gislason, R.W. Morton, R.M. Laine "Liquid-Feed Flame Spray Pyrolytic Synthesis of Nanoalumina Powders," *Chem. Mater.* **16**, 21-30 (2004).

24. R. M. Laine, T. Hinklin, G. Williams, S.C. Rand, "Low-Cost Nanopowders for Phosphor and Laser Applications by Flame Spray Pyrolysis," in Mater. Sci. Forum Vols. 343-346, *Scitec & Trans Tech. Publ., Zurich, Switzerland,* **2000** pp. 500-10.

25. R. Baranwal, M. P. Villar, R. Garcia and R. M. Laine, "Synthesis, Characterization, and Sintering Behavior of Nano-mullite Powder and Powder Compacts," *J. Am. Ceram. Soc*. **84**, 951- 61 (2001).

26. G. Williams, S.C. Rand, T. Hinklin, R.M. Laine, "Laser action in strongly scattering rare-earth-doped dielectric nanophosphors," *Phys. Rev. A*. **65**, 013807 (2002).

27. S. Kim, J.J. Gislason, R.W. Morton, X. Pan, H. Sun, R.M. Laine, "Liquid-Feed Flame Spray Pyrolysis of Nanopowders in the Alumina-Titania System," *Chem. Mater*. **16**, 2336-43 (2004).

28. J. Marchal, T. Hinklin, R. Baranwal, T. Johns, and R. M. Laine, "Yttrium aluminum garnet nanopowders by flame spray pyrolysis," *Chem. Mater*. **16**, 822-831 (2004).

29. R.M. Laine, J. Marchal, H.J. Sun, X.Q. Pan, "A new $Y_3Al_5O_{12}$ phase produced by liquid-feed flame spray pyrolysis (LF-FSP)," *Adv. Mater.* **17**, 830-33 (2005).

30. J.A. Azurdia, J.C. Marchal, P. Shea, H. Sun, X. Q. Pan, R.M. Laine; "Liquid-feed flame spray pyrolysis (LF-FSP) as a method of producing mixed-metal oxide nanopowders of potential interest as catalytic materials. Nanopowders along the NiO-Al_2O_3 tie-line including $(NiO)_{0.22}(Al_2O_3)_{0.78}$, a new inverse spinel composition." *Chem. Mater.* **18** (2006) 731-739

31. J.A. Azurdia, J.C. Marchal, R.M. Laine, "Combinatorial processing of mixed-metal oxide nanopowders along the Co_3O_4-Al_2O_3 tie line using liquid-feed flame spray pyrolysis (LF-FSP)," *J. Am. Ceram. Soc.,* **89 [9]** 2749–2756 (2006).

32. T. R. Hinklin, R.M. Laine, "Combinatorial processing of mixed-metal oxide nanopowders along the MgO-Al_2O_3 tie line using liquid-feed flame spray pyrolysis (LF-FSP)," *Chem. Mater.* In press. (2008).

33. M. Kim, R. M. Laine, "Liquid-feed flame spray pyrolysis (LF-FSP) for combinatorial processing of nanooxide powders along the $(ZrO_2)_{1-x}(Al_2O_3)_x$ tie-line. Phase segregation and the formation of core-shell nanoparticles," *J. Cer. Proc. Res. **8** 129-136* (2007).

34. M. Kim, T. R. Hinklin, R. M. Laine, "Core-shell nanostructure nanopowders along $(CeO_x)_x(Al_2O_3)_{1-x}$ tie-line by liquid-feed flame spray pyrolysis (LF-FSP)" submitted to *Chem. Mater.* (2008).

35. R. M. Laine. J. C. Marchal, H. P. Sun, X. Q. Pan, "Nano alpha Al_2O_3 by liquid-feed flame spray pyrolysis," *Nature Materials* **5(9)** 710-712 (2006).

36. E.N. Bunting, *Bur. Stand. J. Res*., 8 (2), 279-87 (1932).

37. R. Hansson, P.C. Hayes, and E. Jak, "Experimental study of phase equilibria in the Al-Fe-Zn-O system in air," *Metall. Mater. Trans. B*, 35B, 633-642 (2004).

38. H. Kim, A. Pique, J.S. Horwitz, H. Murata, Z.H. Kafafi, C.M. Gilmore, and D.B. Chrisey, "Effect of aluminum doping on zinc oxide thin films grown by pulsed laser deposition for organic light-emitting devices," *Thin Sol. Films*, **377-378**, 798-802 (2000).

39. H. Cao, C. Sun, Z. Pei, A. Wang, L. Wen, R. Hong, and X. Jiang, "Properties of transparent conducting ZnO:Al oxide thin films and their application for molecular organic light-emitting diodes," *J. Mater. Sci.: Mater. Electro.,* **15**, 169-174 (2004).

40. X. Liu, R. E. Truitt, “DRFT-IR Studies of the Surface of γ-Alumina,” *J. Am. Chem. Soc.* **119** 9856-9860 (1997)

41. J. B. Peri, “Infrared and gravimetric study of the structure hydration of γ-alumina,” *J. Phys. Chem*. **69** 211-219 (1965)

42. S. Shen, K. Hidahat, L. Yu, and S. Kawi, “Simple hydrothermal synthesis of nanostructured and nanorod Zn-Al complex oxides as novel nanocatalysts,” Adv. Mater. **16**, 541-5(2004).

43. A. Adak, A. Pathak, P. Pramanik, “Characterization of ZnAl2O4 nanocrystals prepared by the polyvinyl alcohol evaporation route,” *J. Mater. Sci. Lett*. **17**, 559-561 (1998).

44. S.V. Tsybulya, L.P. Solov’eva, L.M. Plyasova, O.P. Krivoruchko, “Refinement of cation distribution in the structure of nonstoichiometric aluminozinc spinel,” Zh. Strukt. Kim., **32**, 86-9 (1991).

45. A. N. Tsvigunov, V. G. Khotin, A. S. Krasikov and B. S. Svetlov, “Shock-Wave Synthesis of Nonstoichiometric Aluminizing Spinel and Gahnite,” Glass and Ceramics, **58**, 353-5 (2002).

CHAPTER 7
CONCLUSION AND FUTURE WORKS

7.1 Conclusion

We here demonstrated the utility of LF-FSP for combinatorial synthesis of variety of mixed metal oxide nanopowders. LF-FSP provides access to mixed-metal oxide nanopowders with exceptional control of stoichiometry and phase purity. Here we have succeeded in preparing nanopowders of any composition in $(ZrO_2)_x(Al_2O_3)_{1-x}$, $(CeO_x)_x(Al_2O_3)_{1-x}$, $(CeO_x)_x(ZrO_2)_{1-x}$, $(Ce_{0.7}Zr_{0.3}O_2)_{0.x}(Al_2O_3)_{1-x}$, and $(ZnO)_x(Al_2O_3)_{1-x}$ systems. The resulting materials are very complex in phase composition and behavior. However, it appears possible to completely map compositions and phases in this system. As-produced nanopowders are with specific surface area 30-70 m^2/g at rates of 100-300 g/h.

Most of all, we succeeded in producing core-shell nanoparticles in the $(ZrO_2)_x(Al_2O_3)_{1-x}$, $(CeO_x)_x(Al_2O_3)_{1-x}$, and $(Ce_{0.7}Zr_{0.3}O_2)_{0.x}(Al_2O_3)_{1-x}$ systems in a single step with the correct choice of metalloorganic precursors. Because LF-FSP offers rapid quenching of the combustion species, it provides access to new, kinetic materials not accessible by any other conventional processing method. These nanopowders can offer novel potential for catalytic, photonic, structural, electrical and biomedical applications.

For the $(ZrO_2)_x(Al_2O_3)_{1-x}$ system, we were able to observe what appears to be the presence of of Zr $^{2+/3+}$ ions in Zr-Al-O binary system. These nanopowders may offer utility in photonic applications anticipated based on Ti doped sapphire lasers.

For the $(CeO_x)_x(Al_2O_3)_{1-x}$ system, We found the presence of Ce^{3+} ions in δ-alumina lattice at all concentrations and Ce-magnetoplumbite at 5-10 mole % CeO_x concentrations. We also find the presence of Ce^{3+} ions in nanopowders of Ce-Al-O system, Ce-magnetoplumbite structure and $(CeO_x)_x(Al_2O_3)_{1-x}$ core-shell nanostructured nanoparticles at specific CeO_x compositions. These nanopowders can offer novel potential for catalytic, structural, photonic, and electronic applications.

LF-FSP processing can provide low-cost, efficient routes to well-known but enhanced catalyst materials, especially for emission control applications. LF-FSP provides exceptional control of stoichiometry and phase purity for the $(CeO_x)_x(ZrO_2)_{1-x}$ and $(Ce_{0.7}Zr_{0.3}O_2)_{0.x}(Al_2O_3)_{1-x}$ mixed-metal oxide nanopowders. We were able to produce nanopowders of any composition in the Ce-Zr-O and Ce-Zr-Al-O systems with specific surface area of ≥ 30 m^2/g at rates of 50-100 g/h. We were able to produce nano $Ce_{0.7}Zr_{0.3}O_2$ solid solutions in $(CeO_x)_x(ZrO_2)_{1-x}$ system and find the formation of single crystal $Ce_{0.7}Zr_{0.3}O_2$ solid solutions in δ-alumina nanoparticles, exclusively by LF-FSP.

We did sintering studies of as-produced core-shell nanostructured nanopowers. Here we report efforts to produce fully dense nanostructured ZTA nanocomposites with 99+% density. These studies use LF-FSP produced $(ZrO_2)_x(Al_2O_3)_{1-x}$ core-shell nanopowders with phase pure t-zirconia cores and δ-alumina shell with APSs < 20 nm. These powders allow us to produce fully dense ZTA nanocomposites with grain sizes less than 200 nm using pressureless sintering in air at < 1150 ^oC. We are also able to control t to m phase transformation of nano zirconia without yttria offering the potential to obtain phase transformation toughening.

We expect our fully dense nanostructured ZTA nanocomposites of the novel potentials for structural, biomedical applications with enhanced strength, fracture toughness and thermal shock resistance.

The utility of LF-FSP processing for combinatorial studies of nanopowders along the $(ZnO)_x(Al_2O_3)_{1-x}$ tie line was demonstrated focusing on composition regions including Al-doped ZnO for TCO applications and zinc spinel. For ZnO rich samples, the XRD data suggest that Al^{3+} ions incorporate into interstitial site of zincite resulting in octahedrally coordinated Al^{3+}. At 80 mole % ZnO contents, small amounts of spinel phase segregation occur, while the XRD results suggest formation of a single zincite phase at compositions at zinc-rich samples (99, 95 mole % ZnO). Based on the solubilities of Al_2O_3 in ZnO and vice versa, we can suggest an effective operating temperature for LF-FSP processing that ranges between 1700-1800°C in ZnO-Al_2O_3 system from the two compositional regions studied. As noted above, the resulting materials suggest that the ZnO-Al_2O_3 phase diagram may need revision. Also,

reprocessing as-prepared nanopowders by LF-FSP can cause phase separation due to vaporization under high temperature.

7.2 Future works

We will do the sintering studies of $(CeO_x)_x(Al_2O_3)_{1-x}$, and $(Ce_{0.7}Zr_{0.3}O_2)_{0.x}(Al_2O_3)_{1-x}$ core-shell nanopowders for potential catalytic and photonic applications. We might expect to produce the final composite with submicron grains, based on the bulk diffusivity of each elements.

We also plan to produce core-shell nanopowders of α-alumina core using LF-FSP. Instead of metalloorganic precursors, we will use emulsion of as-processed δ-alumina nanopowders and precursor targeted as shell materials, because we expect δ to α alumina phase transformation during LF-FSP processing. Effect of shell materials on the δ to α alumina phase transformation will also be studied.